UNIVERSITY OF CALIFORNIA
RIVERSIDE

Better Constraints for the $M_{\rm BH} - \sigma_*$ Relation in the Non-Local Universe
&
Correlations of Ionized Gas Outflows with AGN and Host Galaxy Properties

A Dissertation submitted in partial satisfaction
of the requirements for the degree of

Doctor of Philosophy

in

Physics

by

Remington O. Sexton

September 2020

Dissertation Committee:

Professor Gabriela Canalizo, Chairperson
Professor Frederick Hamann
Professor Brian Siana

The Dissertation of Remington O. Sexton is approved:

Committee Chairperson

University of California, Riverside

Acknowledgments

There are a countless number of individuals responsible for me ending up where I am today, most of whom will not fit on this page, but I am grateful for all of their help through my entire academic journey.

First and foremost, to my parents Elvira and Stanley, who provided their everlasting support and unconditional love, even through the hardest of times. Thank you, mom and dad.

I would like to thank my Ph.D. advisor, Dr. Gabriela Canalizo, for her support and mentoring - but most of all - for her patience, as she watched me reinvent many wheels for the sake of my own understanding.

To Marcela, who has been by my side through my entire time at UCR, thank you for your encouragement, love, understanding, and putting up with me this whole time. And to my cats, Kitters and Sprinkle, who have never left my side, even as I write this. Finally, to my friends. You know who you are. Thanks for all the laughs.

I acknowledge financial support from the NASA MIRO program through the Fellowships and Internships for Extremely Large Data Sets (FIELDS) in the form of a Graduate Student Fellowship. I personally thank Dr. Bahram Mobasher for his generous support as a FIELDS graduate student fellow. Partial financial support was provided by the National Science Foundation, under grant No. AST 1817233.

The text of this dissertation, in part, is a reprint of a published article titled "Stronger Constraints on the $M_{\rm BH} - \sigma_*$ Relation up to $z \sim 0.6$" as it appears in *The Astro-*

physical Journal, Volume 878, Number 2, 19 June 2019. The co-authors, Gabriela Canalizo, Kyle D. Hiner, Stefanie Komossa, Jong-Hak Woo, Ezequiel Treister, Sabrina Lyn Hiner Dimassimo listed therein supervised or provided comments to assist in the publication of the article as it appears in this dissertation.

ABSTRACT OF THE DISSERTATION

Better Constraints for the $M_{\rm BH} - \sigma_*$ Relation in the Non-Local Universe
&
Correlations of Ionized Gas Outflows with AGN and Host Galaxy Properties

by

Remington O. Sexton

Doctor of Philosophy, Graduate Program in Physics
University of California, Riverside, September 2020
Professor Gabriela Canalizo, Chairperson

We revisit the possibility of redshift evolution in the $M_{\rm BH} - \sigma_*$ relation with a sample of 22 Seyfert 1 galaxies with black holes (BHs) in the mass range $10^{6.3} - 10^{8.3}$ $M_\odot$ and redshift range $0.03 < z < 0.57$ with spectra obtained from spatially resolved Keck Low-Resolution Imaging Spectrometer observations. Stellar velocity dispersions were measured directly from the Mg Ib region, taking into consideration the effect of Fe II contamination, active galactic nucleus (AGN) dilution, and host-galaxy morphology on our measurements. BH masses are estimated using the Hβ line width, and the luminosity at 5100 Å is estimated from surface brightness decomposition of the AGN from the host galaxy using high-resolution imaging from the *Hubble Space Telescope*. Our selection criteria allowed us to probe lower-luminosity AGNs and lower-mass BHs in the non-local universe than those measured in previous single-epoch studies. We find that any offset in the $M_{\rm BH} - \sigma_*$ relation up to $z \sim 0.6$ is consistent with the scatter of local BH masses, and address the sources of biases and uncertainties that contribute to this scatter.

We present Bayesian AGN Decomposition Analysis for SDSS Spectra (BADASS), an open source spectral analysis code designed for automatic detailed deconvolution of AGN and host galaxy spectra, implemented in Python, and designed for the next generation of large scale surveys. BADASS simultaneously fits all spectral components, including power-law continuum, stellar line-of-sight velocity distribution, Fe II emission, as well as narrow, broad, and outflow emission line features, all performed using Markov Chain Monte Carlo to obtain robust uncertainties and autocorrelation analysis to assess parameter convergence.

We use BADASS to perform correlation analysis of 63 SDSS Seyfert 1 galaxies with evidence of strong non-gravitational outflow kinematics in the [O III]λ5007 emission line. We confirm findings from previous studies that show the core of the [O III] profile is a suitable surrogate for σ_*, however there is evidence that the core experiences broadening that scales with outflow velocity. We find sufficient evidence that σ_*, [O III] core dispersion, and the non-gravitational outflow dispersion of the [O III] profile form a plane whose fit results in a scatter of ~ 0.1 dex. Finally, we discuss the implications, caveats, and recommendations when using the [O III] dispersion as a surrogate for σ_* for the $M_{\rm BH} - \sigma_*$ relation.

Contents

List of Figures

List of Tables

Chapter 1

Introduction

In light of the most recent scientific breakthroughs regarding supermassive black holes (BHs), such as the first image of the supermassive black hole of M87 (Event Horizon Telescope Collaboration et al., 2019), the story of their discovery begins as early as the early 1960s. The first indication that strong radio sources identified by early surveys were of peculiar interest were their large redshifts coupled with their compact stellar appearance (Schmidt, 1963), and shortly afterward more objects of this nature were discovered (Matthews & Sandage, 1963). The most reasonable explanation for their high-luminosities at such large redshifts was given by Salpeter (1964), who suggested that only gravitational accretion of interstellar matter onto a massive object could explain observations. Since then, we have referred to such objects as active galactic nuclei (AGN), a general term to describe an entire paradigm of astrophysical objects, powered by supermassive black holes, which are believed to reside at the center of every galaxy. These powerful cosmic engines, fueled by infalling matter, are believed to play an key role in the formation of galaxies over the last

13.8 Gyr.

Clues as to how supermassive BHs evolve with their host galaxies manifest themselves in the form of scaling relations, i.e., how properties of BHs (namely mass), scale with properties of their host galaxies. The most commonly seen host properties that scale with BH mass ($M_{\rm BH}$) are stellar velocity dispersion (σ_*), bulge luminosity ($L_{\rm bulge}$), and bulge stellar mass (M_*) (see Kormendy & Ho (2013) for a review of all such relations). Among these, the $M_{\rm BH} - \sigma_*$ relation stands out as the most fundamental BH scaling relation since it implies a relationship between the growth of the supermassive BH and the host galaxy kinematics which governed its formation (Ferrarese & Merritt, 2000; Gebhardt et al., 2000a).

This implication of so-called "co-evolution" between $M_{\rm BH}$ and σ_* could also imply that there is some means of communication between the central BH - whose gravity cannot exceed a relatively small sphere of influence - and the surrounding host stars at kpc scales. One of the foremost theories as to how BHs influence their hosts is through feedback in the form of large-scale outflows (Fabian, 2012; King & Pounds, 2015), while others argue that galaxy mergers are the cause (Jahnke & Macciò, 2011), or possibly both. There is also the possibility that the $M_{\rm BH} - \sigma_*$ relation is only a local relation - a sort of evolutionary end-point - that we only observe today, which implies we should observe a significantly different $M_{\rm BH} - \sigma_*$ relation in the non-local universe. To identify which of these evolutionary tracks explains our observations requires the probing of $M_{\rm BH} - \sigma_*$ relation at higher redshifts.

In Chapter 2, we revisit the possibility of evolution in the $M_{\rm BH} - \sigma_*$ relation with observations of a sample of 22 Seyfert 1 galaxies in the local and non-local universe using a standard sample selection criteria based on the broad Hβ line width. To address the

requirements of fitting AGN and host galaxy spectra, we introduce a new fitting algorithm in Chapter 3 called Bayesian AGN Decomposition Analysis for SDSS Spectra (BADASS), developed specifically for the detailed fitting of AGN spectra and to detect objects with ionized outflows commonly seen in optical forbidden emission lines. Finally, in Chapter 4, we discuss the results of fitting a sample of 63 Seyfert 1 galaxies with strong ionized outflows using BADASS, and some promising correlations of outflow kinematics with properties of AGNs and host galaxies.

Chapter 2

Stronger Constraints on the Evolution of the $M_{\rm BH} - \sigma_*$ Relation up to $z \sim 0.6$

2.1 Introduction

Since their initial discovery nearly two decades ago, black hole (BH) scaling relations have motivated extensive study in the role of central supermassive black holes (SMBHs) in the evolution of their host galaxies over cosmic time. Measurements of gas kinematics in inactive galaxies revealed a strong correlation between the mass $M_{\rm BH}$ of the central SMBH and the stellar velocity dispersion σ_* of the central spheroid of its host galaxy (Ferrarese & Merritt, 2000; Gebhardt et al., 2000a; Tremaine et al., 2002; McConnell & Ma, 2013). This fundamental relationship was soon established for local active galaxies as well by exploiting

the visible broad-line regions (BLRs) in type 1 active galactic nuclei (AGNs) as a direct probe of virial BH mass (Gebhardt et al., 2000b; Ferrarese et al., 2001; Onken et al., 2004; Greene & Ho, 2006a; Woo et al., 2010; Bennert et al., 2011a; Woo et al., 2013; Bennert et al., 2015; Woo et al., 2015). Today, the $M_{\rm BH} - \sigma_*$ relation remains the strongest and most fundamental correlation between SMBHs and their host galaxies (see Kormendy & Ho (2013) for a comprehensive review).

There exists an ongoing debate as to whether SMBHs co-evolve in tandem with their host galaxies over time or if the scaling relations we observe today are an evolutionary endpoint, such that host galaxies grow over time to "catch up" to their SMBHs formed at much earlier times. Co-evolution would imply some feedback mechanism powered by the central AGN, which acts to self-regulate the growth of the SMBH and host galaxy (Fabian, 2012; King & Pounds, 2015). In the latter scenario, scaling relations as the result of an evolutionary endpoint call into question how the seeds of today's SMBHs grew so rapidly in the early universe (Volonteri, 2010; Greene, 2012). Alternatively, the emergence of BH scaling relations could be non-causal in nature, and could be explained through the hierarchical assembly of BH and stellar mass via mergers (Jahnke & Macciò, 2011). To address the controversy, numerous attempts have been made to measure $M_{\rm BH} - \sigma_*$ in the non-local universe to determine which SMBH evolutionary track may be responsible for local observations.

Early attempts by Woo et al. (2006) and Woo et al. (2008) to measure the $M_{\rm BH} - \sigma_*$ relation of broad-line Seyfert 1 galaxies at $z = 0.36$ and $z = 0.57$ resulted in a significant positive offset of 0.43 dex and 0.63 dex in $M_{\rm BH}$, respectively, implying that BHs were "over-

massive" relative to their host galaxies at earlier times. If we quantify the required stellar mass assembly as inferred from stellar velocity dispersion (Zahid et al., 2016), the results by Woo et al. imply that host bulges must grow by a factor of ~ 4 within 4 Gyr ($z = 0.36$), and a factor of ~ 6 within 5.5 Gyr ($z = 0.57$), to be consistent with the $M_{\rm BH} - \sigma_*$ relation at $z = 0$. This is problematic since it means that bulges must undergo significant stellar mass assembly in a relatively short amount of time, and the possible mechanisms for doing so without significantly growing their BHs remain largely speculative. Similar studies by Canalizo et al. (2012) using dust-reddened 2MASS quasi-stellar objects (QSOs) at $0.14 < z < 0.37$, and Hiner et al. (2012) using post-starburst QSOs at $z \sim 0.3$, found a similar significant positive offset from the local relation, which further exacerbated the problem.

It is however possible that the observed offset in the $M_{\rm BH} - \sigma_*$ relation at higher redshifts is not of physical origin, but the result of selection bias. Lauer et al. (2007) explained that AGNs selected by a luminosity threshold preferentially selects overmassive BHs relative to their hosts due to a steep drop in the luminosity function of galaxies. In addition to this, Shen & Kelly (2010) suggested that single-epoch (SE) samples can be biased toward high BH masses due to uncorrelated variations between continuum luminosity and line widths in reverberation mapping studies. These two biases can act independently and in conjunction with one another to create the observed offset from the local $M_{\rm BH} - \sigma_*$ relation and give a false indication of host-galaxy evolution. Selecting samples at both low and high redshift using consistent criteria can help to mitigate these biases. In addition to this, since previous non-local studies primarily sampled BHs at the high-mass regime of the

$M_{\rm BH} - \sigma_*$ relation, it would be ideal to sample the low-mass regime of the $M_{\rm BH} - \sigma_*$ relation as a function of redshift. Since selection criteria based on AGN luminosity necessarily bias samples toward the more massive BHs of AGNs, we have historically lacked a sample of lower-mass BHs of comparable galaxy sizes as those previously studied, especially in the non-local universe.

In this paper we attempt to address the aforementioned biases using a new set of selection criteria based on the broad Hβ emission line width to select lower-mass BHs in the non-local universe. In Section 2.2 we discuss our sample selection, observations/data acquisition, and reduction procedure. In Section 2.3 we describe in detail how measurements of σ_*, line widths, and AGN luminosity are performed to calculate BH mass. We also investigate the use of the [O III] width as a proxy for σ_* in the context of BH scaling relations following the precedent of previous studies (Brotherton, 1996; McIntosh et al., 1999; Véron-Cetty et al., 2001; Shields et al., 2003; Greene & Ho, 2005; Woo et al., 2006; Komossa & Xu, 2007; Bennert et al., 2018). In Section 2.4 we present our results for our sample on the $M_{\rm BH} - \sigma_*$ relation and investigate the possible evolution as a function of redshift. We discuss any systematic uncertainties and selection biases which may affect our results in Section 2.5. Finally, we discuss the implications of our results in Section 2.6.

Throughout this paper, we assume a standard cosmology of $\Omega_m = 0.27$, $\Omega_\Lambda = 0.73$, and $H_0 = 71$ km s^{-1} Mpc^{-1}. We refer to individual objects by their abbreviated object designations (i.e., J000338, etc.).

2.2 Data Acquisition

2.2.1 Sample Selection

To construct the sample, objects were selected from the SDSS DR7 (York et al., 2000) database which satisfied the following properties: (1) a redshift within the range $0.0 < z < 0.9$ to ensure that the broad Hβ and Mg Ib complexes were within the observed spectral range of the SDSS, (2) a broad Hβ FWHM within the range 500 km s^{-1} $\leq$ FWHM$_{\mathrm{H}\beta}$ $\leq$ 2000 km s^{-1} to select lower BH mass objects, and (3) visible stellar absorption features (typically Ca H+K equivalent width EW$_{\mathrm{CaH+K}} > 0.5$ Å) to ensure that σ_* could be accurately measured. The resulting 2539 objects were then cross-referenced with *HST* archival data to ensure that high-resolution images were available for detailed deconvolution of the AGN point-spread function (PSF) and its respective host galaxy. Relatively deep (1000-2000+ s) *HST* imaging was found for 32 objects, performed using a variety of instruments and filters, and spanning the redshift range $0.03 < z < 0.57$. Observational time constraints allowed for spatially resolved optical spectroscopy of 29 of the 32 objects using the Keck Low-Resolution Imaging Spectrometer (LRIS; see Section 2.2.2). Modeling of the power-law AGN continuum to determine the luminosity at 5100 Å could not be performed on seven objects due to the high fraction of stellar light from the host galaxy and were omitted from the final sample.

The final sample of 22 objects are listed in Table 2.1. Of these, eight satisfy the Hβ width criteria for narrow-line Seyfert 1 (NLS1) galaxies (500 km s^{-1} $\leq$ FWHM$_{\mathrm{H}\beta}$ $\leq$ 2000 km s^{-1}; Goodrich (1989)), while the remaining 14 are classified as broad-line Seyfert 1 (BLS1) galaxies (FWHM$_{\mathrm{H}\beta} > 2000$ km s^{-1}). It is possible that more objects in our sample

satisfy the broad-line width criterion for NLS1s since these objects tend to exhibit Lorentzian profiles (Véron-Cetty et al., 2001); however we still require the Gaussian FWHM model to determine BH mass.

We note that the definition of "NLS1" can extend beyond the Hβ line width criteria given above. Previous studies have selected NLS1s based on the flux ratio [O III]/H$\beta_{\rm broad} < 3$ (Shuder & Osterbrock, 1981; Osterbrock & Pogge, 1985), which ensures that NLS1s have larger Hβ widths than forbidden lines; however this criterion does not exclude BLS1s. All 22 objects in our sample satisfy the [O III]/H$\beta_{\rm broad} < 3$ criterion by virtue of the fact that all of the objects in our sample are Type 1 AGNs. Another commonly cited characteristic of NLS1 galaxies include strong Fe II emission in the presence of weak [O III] emission. However, more recent studies with larger samples of NLS1s have found that correlations of Fe II with other emission line properties are not as unique to NLS1s as previously thought. For instance, Véron-Cetty et al. (2001) found that any anti-correlation between Fe II and [O III] is weak at best, and concluded that all objects with broad Hβ < 2000 km s^{-1} are genuine NLS1s. Similarly, Xu et al. (2012) and Valencia-S. et al. (2012) found that the same correlations between Fe II and other emission line properties commonly found in NLS1s are as common among BLS1s, implying that these selection criteria are not unique to NLS1s, but rather that strong Fe II emission is a common property across the arbitrarily chosen line width criteria that distinguish NLS1s and BLS1s. We therefore find that our definition of NLS1 based on solely on line width is justified.

The small fraction of NLS1 objects obtained in the final sample can be traced back to the simplistic algorithm used to perform emission line fits in SDSS DR7, particu-

larly when applied to SDSS-classified QSO spectra. The large (1000 pixel) mean/median filter used for continuum subtraction does not perform well in the presence of a strong and rapidly varying stellar continuum. Additionally, the DR7 algorithm does not simultaneously fit narrow and broad components, and can therefore produce inaccurate results if there is a strong narrow-line emission present atop a broad-line component. The DR7 algorithm performs optimally when fitting SDSS-classified QSOs which exhibit a weaker stellar continuum relative to the AGN continuum and weaker narrow-line emission relative to broad-line emission. This is opposite of what is seen of typical NLS1 galaxies, which have a stronger stellar continuum relative the AGN continuum, and narrow emission lines of comparable widths to the broad-line emission components. Because the DR7 algorithm is not optimized for the peculiar spectra of NLS1 galaxies, we do not recommend using the DR7 emission-line database (`specLine` table) to query NLS1 objects.

2.2.2 Observations

Long-slit spectroscopy was performed on 2015 March 24-25 and 2015 December 3-4 using the LRIS (Oke et al., 1995) on the Keck I Telescope atop the summit of Maunakea in Hawai'i. Weather conditions for all nights were clear, with subarcsecond seeing ranging between $0\farcs6$ and $0\farcs8$. A $1''$ slit was chosen to spatially resolve both the central region close to the AGN and the host galaxy bulge within the effective (half-light) radius. Figure 2.1 shows the position angle of the slit, chosen to be aligned with the semi-major axis of the bulge component of the host galaxy. After passing through the slit, the beam is then collimated and split by a dichroic designated by a wavelength cutoff. Wavelengths below the dichroic cutoff are passed through a grism and into the LRIS-B camera, while wavelengths

above the cutoff are passed through a grating of a specified blaze angle into the LRIS-R camera. Both the LRIS-B and LRIS-R (Rockosi et al., 2010) CCD detectors have a pixel scale of $0.135''\text{pixel}^{-1}$. Table 2.1 lists the dichroic, grating, and central wavelength used for each object to ensure that the region around Hβ was captured on the LRIS-R detector. The 1200/7500, 900/5500, and 600/5000 lines mm^{-1} gratings provide logarithmically rebinned (constant velocity) spectral resolutions of $\sim$ 20, 27, and 40 km s^{-1}, respectively. All observations with the LRIS-B detector utilized the 600/4000 lines mm^{-1} grism, which has a spectral resolution of $\sim$ 32 km s^{-1}.

2.2.3 Data Reduction

Spectroscopic data reduction was performed using standard techniques with a combination of IRAF (Valdes, 1984) and Python scripts. Separate reductions were performed for each of the nine LRIS observing configurations in our sample, based on the dichroic, grating, and central wavelength chosen for each object (Table 2.1). After bias subtraction and flat-fielding, cosmic ray removal was performed using *L.A.Cosmic* (van Dokkum et al., 2012). Any leftover cosmic ray artifacts were manually removed using the IRAF task *imedit*. Wavelength calibration was performed using Hg, Cd, and Zn arc lamps on the LRIS-B side, while Ne and Ar arc lamps were used on the LRIS-R side. Sky emission lines were then used to correct for small linear shifts in the wavelength axis due to flexure. Sky emission lines were subsequently removed by fitting the background with a low-order polynomial.

Table 2.1: Summary of Keck/LRIS observations. Column 1: object. Column 2: right ascension. Column 3: declination. Column 4: redshift. Column 5: spatial scale per pixel. Column 6: position angle of slit during observations, measured E of N. Column 7: dichroic cutoff wavelength. Column 8: LRIS-R grating. Column 9: central wavelength of grating. Column 10: exposure time. Column 10: observation date.

Object	R.A. (J2000)	Decl. (J2000)	z	Spatial Scale (kpc pix^{-1})	PA (deg)	Dichroic (Å)	Grating (l mm^{-1})	Cen. Wave. (Å)	Exp. Time (s)	Obs. Date (yyyy mm dd)
J000338.94+160220.6	00:03:38.94	+16:02:20.65	0.11681	0.281	22	500	600/5000	6500	1200	2015 Dec 03
J001340.21+152312.0	00:13:40.21	+15:23:12.04	0.12006	0.288	113	500	600/5000	6500	1200	2015 Dec 03
J015516.17−094555.9	01:55:16.17	-09:45:55.94	0.56425	0.875	166	560	600/5000	6500	2400	2015 Dec 04
J040210.90−054630.3	04:02:10.90	-05:46:30.35	0.27065	0.554	109	560	600/5000	6500	1200	2015 Dec 04
J073505.66+423545.6	07:35:05.66	+42:35:45.68	0.08646	0.215	110	460	1200/7500	5360	1200	2015 Mar 24
J092438.88+560746.8	09:24:38.88	+56:07:46.84	0.02548	0.067	96	460	1200/7500	5360	600	2015 Mar 24
J093829.38+034826.6	09:38:29.38	+03:48:26.69	0.11961	0.287	127	460	1200/7500	5360	1200	2015 Mar 24
J095819.87+022903.5	09:58:19.87	+02:29:03.51	0.34643	0.657	95	560	1200/7500	6800	1200	2015 Mar 24
J100234.85+024253.1	10:02:34.85	+02:42:53.17	0.19659	0.434	101	560	600/5000	7150	1200	2015 Mar 25
J101527.25+625911.5	10:15:27.25	+62:59:11.59	0.35064	0.663	94	560	1200/7500	6800	2400	2015 Mar 24
J113657.68+411318.5	11:36:57.68	+41:13:18.51	0.07200	0.182	28	500	1200/7500	5760	2400	2015 Mar 24
J114851.61+514528.7	11:48:51.61	+51:45:28.73	0.06742	0.171	66	500	1200/7500	5760	1200	2015 Mar 24
J120814.35+641047.5	12:08:14.35	+64:10:47.57	0.10555	0.257	95	560	900/5500	6640	1200	2015 Mar 25
J123228.08+141558.7	12:32:28.08	+14:15:58.75	0.42692	0.750	101	560	1200/7500	7200	2400	2015 Mar 24
J123349.92+634957.2	12:33:49.92	+63:49:57.23	0.13407	0.316	92	560	900/5500	6640	1200	2015 Mar 25
J123455.90+153356.2	12:34:55.90	+15:33:56.28	0.04637	0.120	141	500	1200/7500	5760	600	2015 Mar 24
J132504.63+542942.3	13:25:04.63	+54:29:42.38	0.14974	0.347	145	560	600/5000	7150	1200	2015 Mar 25
J132943.60+315336.7	13:29:43.60	+31:53:36.76	0.09265	0.229	131	560	900/5500	6640	1200	2015 Mar 25
J141234.67−003500.0	14:12:34.67	-00:35:00.06	0.12724	0.302	94	500	1200/7500	5760	1200	2015 Mar 24
J142543.20+344952.9	14:25:43.20	+34:49:52.91	0.17927	0.403	53	560	600/5000	7150	1200	2015 Mar 25
J145640.99+524727.2	14:56:40.99	+52:47:27.24	0.27792	0.565	43	560	600/5000	7150	2400	2015 Mar 25
J160044.99+505213.6	16:00:44.99	+50:52:13.60	0.10104	0.247	112	500	1200/7500	5760	2400	2015 Mar 24
J171806.84+593313.3	17:18:06.84	+59:33:13.32	0.27356	0.558	90	560	600/5000	7150	1200	2015 Mar 25

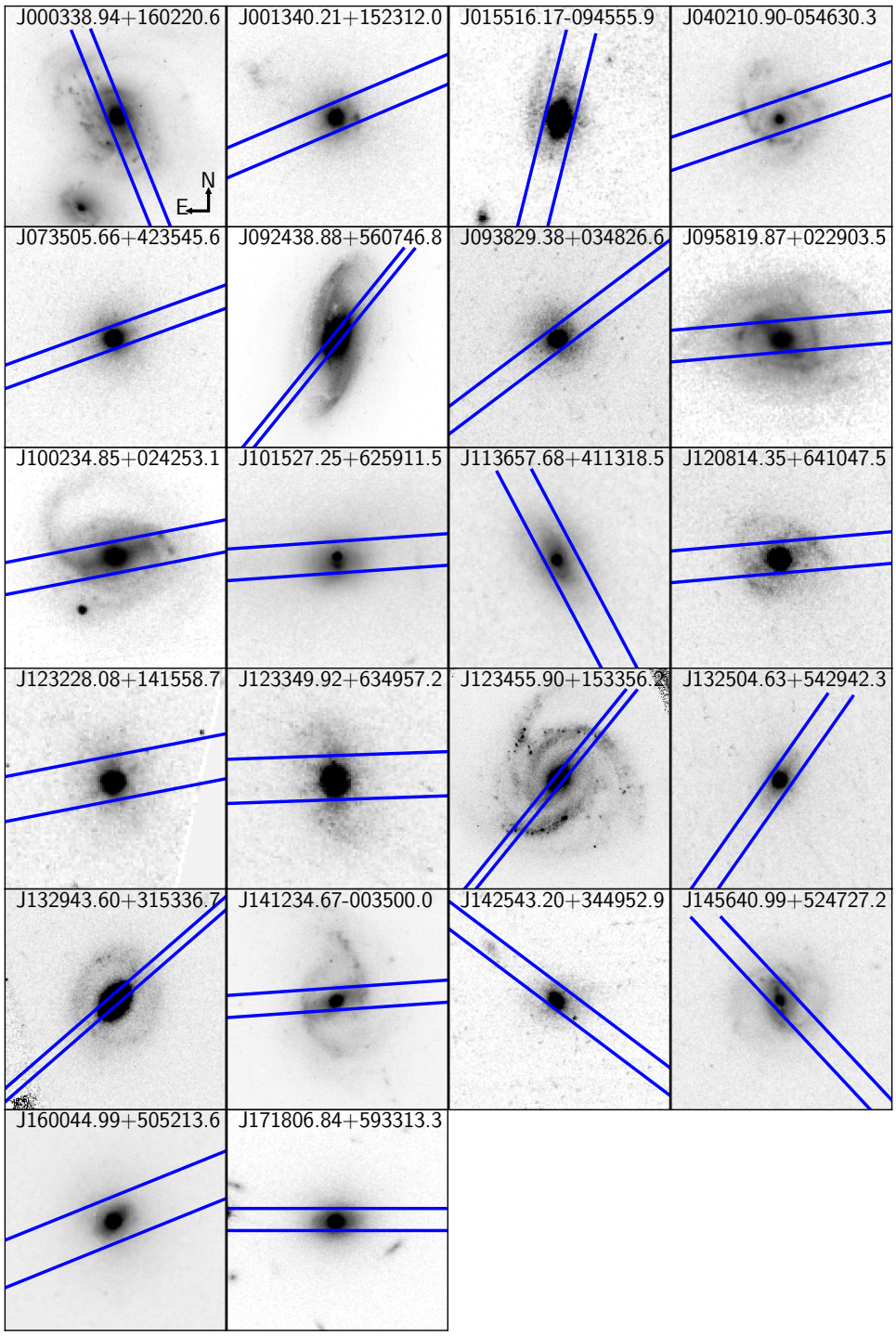

Figure 2.1: *HST* imaging cutouts of our sample. Each image is aligned with north pointed up. Blue bars represent the Keck/LRIS 1″ slit aperture placed on each object and aligned according to the PA (in degrees N of E) listed in Table 2.1.

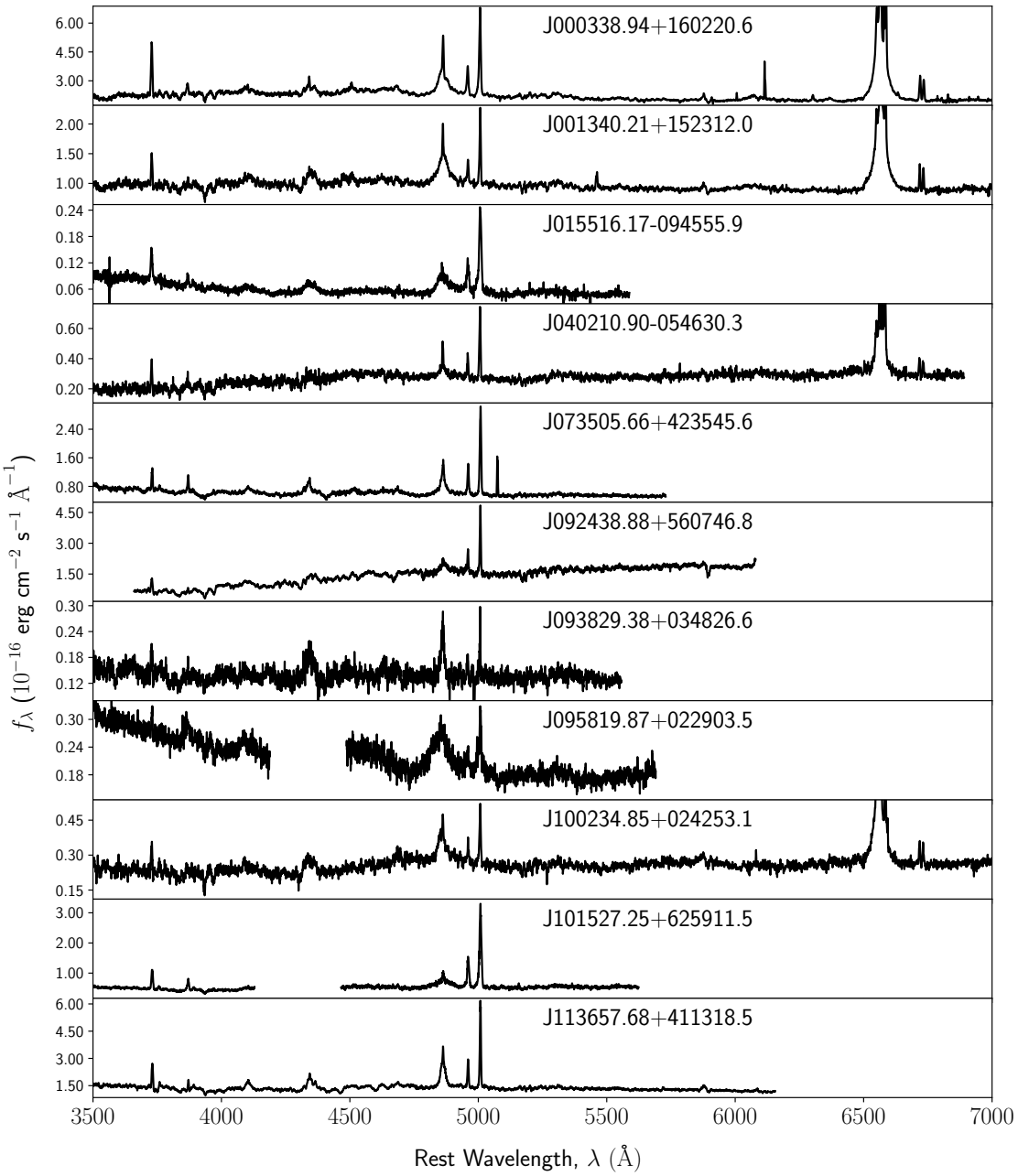

Figure 2.2: Spectra of our sample from Keck/LRIS observations. Gaps in coverage correspond to the dichroic cutoff wavelength and the grating coverage, which depend on the resolution and central wavelength of the grating chosen for each object.

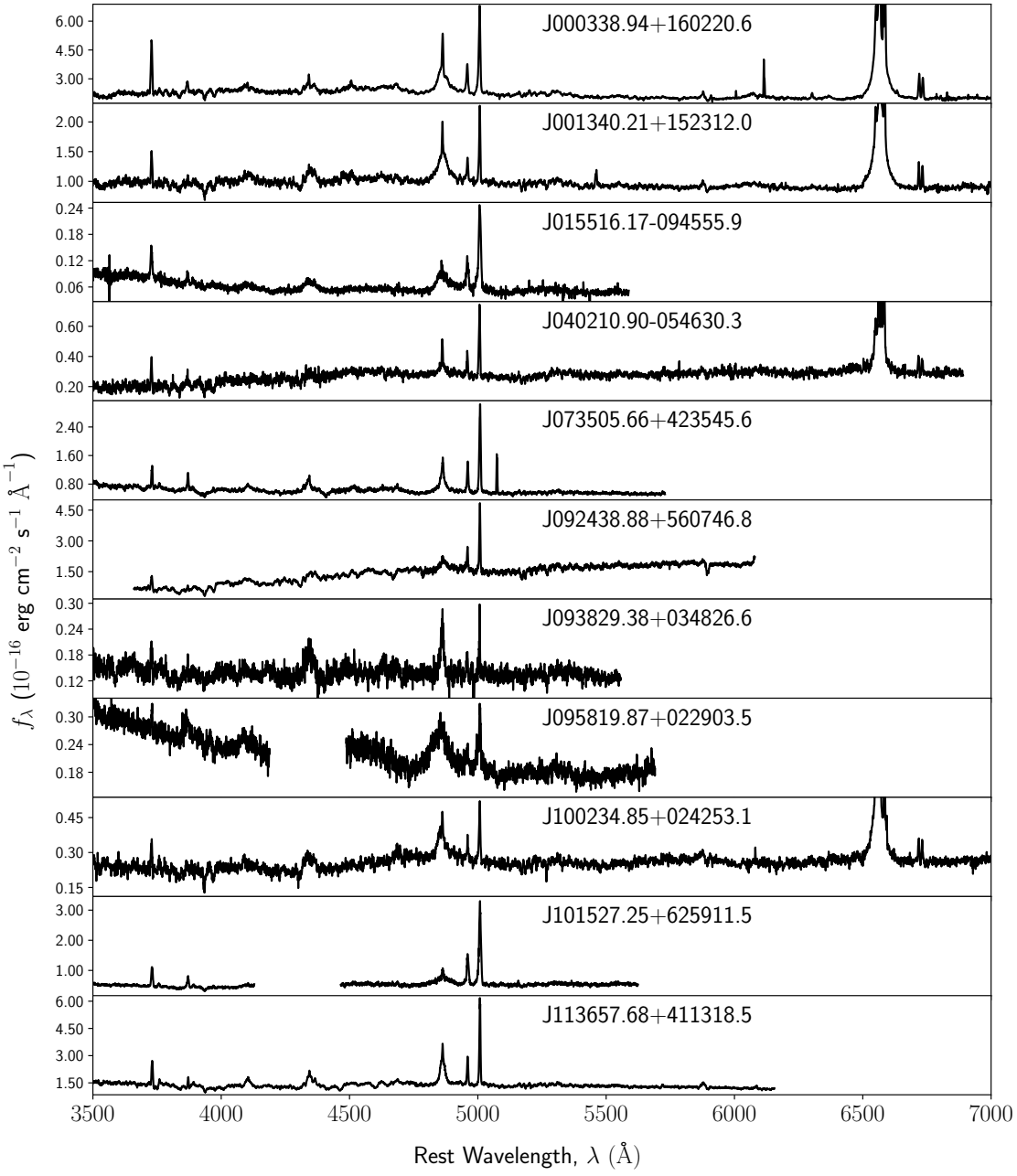

Figure 2.2: *Continued.*

The two-dimensional spectra were then rectified in the spatial direction by tracing the signal of each object along the wavelength direction. Flux calibration was performed using spectrophotometric standards from Massey et al. (1988) and Massey & Gronwall (1990). Telluric correction was performed for spectra that exhibited strong contamination from atmospheric absorption. Objects with two exposures were averaged together using the IRAF task *imcombine*.

The spectra were extracted with an aperture equal to the effective radius $r_{\rm eff}$ of the bulge component measured from *HST* imaging using GALFIT (see Section 2.3.6). The LRIS-B and LRIS-R spectra were then combined into a single spectrum. This was done for two reasons: (1) to maximize wavelength coverage to accurately model the AGN power-law continuum, and (2) to accurately model any Fe II emission between 4400 and 5500 Å that may contaminate the Hβ/ Mg Ib complex. To do this, we convolved the higher-resolution side with a Gaussian to the same resolution as its respective lower-resolution side. We modeled the noise from the lower-resolution spectra to artificially populate the subsequently smoothed higher-resolution side with normally distributed noise of the same standard deviation. The wavelength axis of the higher-resolution side was then interpolated to the same dispersion as the lower-resolution side so they could be combined. Finally, the combined spectrum was logarithmically rebinned to constant velocity scale. For velocity dispersion measurements of the Mg Ib region we used the uncombined LRIS-R spectra, which in cases where the 1200/7500 or the 900/5500 grating was used, have a higher resolution than the LRIS-B grism (see Section 2.3.1). Figure 2.2 shows the final extracted and combined rest-frame spectrum of each object of the final sample. Gaps in spectral coverage between the

LRIS-B and LRIS-R sides occur in three spectra, and are caused by the choice of specific LRIS-R configuration used during observations.

2.2.4 HST Archival Data

Imaging data for each object were obtained via the Hubble Legacy Archive (HLA), which provides enhanced data products that are fully reduced, corrected for artifacts and cosmic rays, drizzled, and combined for all *HST* instruments. Because our sample includes data from a variety of *HST* instruments, filters, and depths, it is crucial that the data for each object be reduced in a consistent and optimized manner for each instrument. Furthermore, HLA data products include robust uncertainty estimates for image data, which are necessary for accurate deconvolution of the AGN PSF from the host galaxy using GALFIT (see §2.3.6). Details of the *HST* imaging used for each object are given in Table 2.2.

Table 2.2: Summary of *HST* archival data[a] obtained for our sample. Column 1: object SDSS designation. Column 2: instrument. Column 3: camera/channel. Column 4: filter. Column 5: spatial scale per side pixel. Column 6: exposure time. Column 7: proposal ID.

Object	Instrument	Camera/Channel	Filter	Spatial Scale (kpc pix^{-1})	Exposure Time (s)	Proposal ID
J000338.94+160220.6	ACS	WFC	F606W	0.10	2084	10889
J001340.21+152312.0	WFC3	UV	F475W	0.09	2268	12233
J015516.17−094555.9	NIC	NIC2	F110W	0.32	5120	11208
J040210.90−054630.3	ACS	WFC	F606W	0.21	720	10588
J073505.66+423545.6	WFPC2	PC	F814W	0.08	1230	11130
J092438.88+560746.8	WFPC2	PC	F814W	0.02	1230	11130
J093829.38+034826.6	WFPC2	PC	F814W	0.11	1230	11130
J095819.87+022903.5	ACS	WFC	F814W	0.24	2028	10092
J100234.85+024253.1	ACS	WFC	F814W	0.16	2028	10092
J101527.25+625911.5	ACS	WFC	F775W	0.25	2360	10216
J113657.68+411318.5	WFPC2	PC	F814W	0.07	1230	11130
J120814.35+641047.5	WFPC2	PC	F814W	0.10	600	6361
J123228.08+141558.7	WFPC2	PC	F606W	0.28	2700	8805
J123349.92+634957.2	WFPC2	PC	F814W	0.12	1230	11130
J123455.90+153356.2	WFPC2	PC	F814W	0.04	600	6361
J132504.63+542942.3	WFPC2	PC	F814W	0.13	1230	11130
J132943.60+315336.7	WFPC2	WF	F814W	0.17	600	6361
J141234.67−003500.0	ACS	WFC	F814W	0.11	1090	10596
J142543.20+344952.9	WFPC2	PC	F814W	0.15	1230	11130
J145640.99+524727.2	ACS	WFC	F606W	0.21	720	10588
J160044.99+505213.6	WFPC2	PC	F814W	0.09	1230	11130
J171806.84+593313.3	ACS	WFC	F814W	0.21	2040	9753

[a]Archival data obtained from Hubble Legacy Archive

2.3 Analysis

In the following sections we discuss the necessary measurements required to analyze our sample on the $M_{\rm BH} - \sigma_*$ relation. We first discuss quantities obtained from spectral analysis beginning with stellar velocity dispersion, which include the effects of host-galaxy inclination and Fe II contamination in our spectra. We then discuss in detail our multi-component fitting methods, how we measure broad Hβ widths for calculation of BH masses, as well as investigate the use of [O III]λ5007 as a surrogate for σ_*. Next we discuss measurements obtained from *HST* imaging, which include surface brightness decomposition and

measurements of the AGN luminosity at 5100 Å. Finally, we derive the equation used to calculate BH masses for our sample.

2.3.1 Stellar Velocity Dispersion

Stellar velocity dispersions were measured using the penalized pixel-fitting (pPXF; Cappellari & Emsellem (2004),Cappellari (2017)) technique, which convolves a series of stellar templates with a Gauss-Hermite kernel to fit the line-of-sight velocity distribution (LOSVD) of the integrated spectrum of stellar light from galaxies. To minimize the possibility of template mismatch, a total of 636 stellar templates with minimal gaps in wavelength coverage were chosen from the Indo-US Library of Coudé Feed Stellar Spectra (Valdes et al., 2004), which have a FWHM resolution of ∼1Å and wavelength range between 3465 and 9469 Å. Additionally, we generated 20 narrow Fe II templates of widths ranging from 50 to 1000 km s^{-1} and 91 broad Fe II templates of widths ranging from 1100 to 10,000 km s^{-1} using the template from Véron-Cetty et al. (2004) to account for possible Fe II contamination and included them with the stellar templates. We note that the choice of Fe II template used to remove Fe II contamination can result in differences in the quality of the subtraction. For example, Barth et al. (2013) notes that the Véron-Cetty et al. (2004) Fe II template better accounts for Fe II emission by modeling emission lines with Lorentzian profiles and includes only Fe II emission features that are commonly found in Seyfert 1 galaxies, as opposed to other Fe II templates which specifically model the Fe II emission of I Zw 1. We find that the inclusion of low-order additive and multiplicative polynomials has no significant effect on our fits; this can be attributed to the inclusion of broad Fe II templates which can account for broad variations in the stellar continuum. We fit the entire Mg Ib/Fe II region from 5025

to 5800 Å when possible, or as much of this region as our wavelength coverage allows.

The algorithm utilizes a penalty function, controlled by a user-input *bias* parameter, which acts to bias the fit toward a Gaussian LOSVD. Monte Carlo simulations were performed to determine the behavior of the penalty function and determine the maximum *bias* parameter at values of $\sigma_* > 3 \times$ (velocity scale) for which the difference between output and input parameters was within the scatter of the simulation. For all of our objects, the optimal *bias* value was determined to be ~ 0.1.

Figure 2.3 shows the best-fit pPXF solution for each object in our sample. The best-fit values of the stellar velocity dispersion for each object are reported in Table 2.4. Uncertainties are determined using Monte Carlo methods by generating 1000 mock spectra using the noise-added best-fit model and re-fitting using pPXF.

2.3.2 Effect of Host Galaxy Inclination on Stellar Velocity Dispersion Measurements

Given that 15 out of the 22 objects in our sample contain a visible disk morphology in *HST* imaging (see Section 2.3.5), we must consider the possible bias in our measurements of σ_* due to disk contamination. Kinematically "cold" disk components can contaminate bulge dispersion measurements and act to increase the measured value of σ_*, especially at intermediate to edge-on inclinations. Hartmann et al. (2014) found that σ_* can be biased by as much as 25% for edge-on systems, and Bellovary et al. (2014) found that considerable scatter in the $M_{\rm BH} - \sigma_*$ relation can be explained by σ_* measurements that do not account for disk inclination. In our sample, we observe that objects that host disk morphologies

have systematically higher values of σ_* on the $M_{\rm BH} - \sigma_*$ relation than objects with no visible disk morphology. Disk inclinations were measured using GALFIT surface brightness decomposition of *HST* imaging (see Section 2.3.5) and using the relation between disk axis ratio (b/a) and inclination i from Pizagno et al. (2007), which takes into account a disk of finite thickness (Haynes & Giovanelli, 1984). Bellovary et al. (2014) used cosmological N-body simulations of disk galaxies to estimate the effect of inclination on measurements of σ_* in bulges that grow naturally over time without making any assumptions on their kinematics, providing an equation to correct for inclination effects as a function of disk rotational velocity $v_{\rm rot}$ and bulge anisotropy $(v/\sigma)_{\rm spec}$. Disk luminosities from GALFIT (see Table 2.3) were corrected for Galactic extinction, as well as intrinsic extinction estimated from measurements of Balmer emission line ratios. We also applied k-corrections and filter transformations from each *HST* filter to SDSS-r using *pysynphot* (STScI development Team, 2013). Finally, we corrected for passive evolution using the online passive evolution calculator from van Dokkum & Franx (2001) by assuming a single stellar population formed at $z >> 1$. We infer rotational velocities $v_{\rm rot}$ that are typical of disk luminosities in our sample, and assume an anisotropy parameter of $(v/\sigma)_{\rm spec} = 0.6$ for a fast-rotating late-type galaxy (Falcón-Barroso et al., 2017). Finally, we obtain a correction for σ_* as a function of i using the prescription from Bellovary et al. (2014) with an adopted uncertainty of 10% for this correction. We find that varying the parameters $v_{\rm rot}$ and $(v/\sigma)_{\rm spec}$ do not considerably change the magnitude of the correction for σ_*. After correcting for inclination, the affected velocity dispersions decrease by 10% on average, but do not significantly change the scatter of our sample on the $M_{\rm BH} - \sigma_*$ relation. If we did not correct for inclination, the majority of our sample would

reside below the relation. Stellar velocity measurements for objects with disk morphologies listed in Table 2.4 have been corrected for the effects of inclination.

2.3.3 Effect of Fe II Contamination on Stellar Velocity Dispersion Measurements

Contamination from Fe II emission is present to some degree in all objects in our sample. This is especially apparent for objects J123349 and J132504, which both exhibit strong narrow Fe II emission between 4400 and 5500 Å (see Figure 2.2). In such cases, pPXF is prone to mistaking narrow Fe II emission for variations in a stellar continuum at some different systemic velocity than real stellar absorption features and can lead to an overestimate of the stellar velocity dispersion. We find that, while broad Fe II emission can easily be subtracted off prior to stellar template fitting without affecting the fit, narrow Fe II emission can make determination of its relative contribution to the host galaxy nearly impossible. To accurately determine the relative contribution of Fe II emission and its effects on our measurements of the LOSVD, we use pPXF to fit Fe II and stellar templates simultaneously. We find that if the total (broad + narrow) Fe II fraction of the total flux within the Mg Ib/Fe II region exceeds ∼5%, the stellar velocity dispersion can be overestimated by as much as 50-90%, due mainly to the presence of strong narrow Fe II. For our sample, the average uncertainty due to the presence of broad and narrow Fe II emission is ∼8%. We further discuss the possible biases in our stellar velocity dispersion measurements due to Fe II contamination in Section 2.5.4.

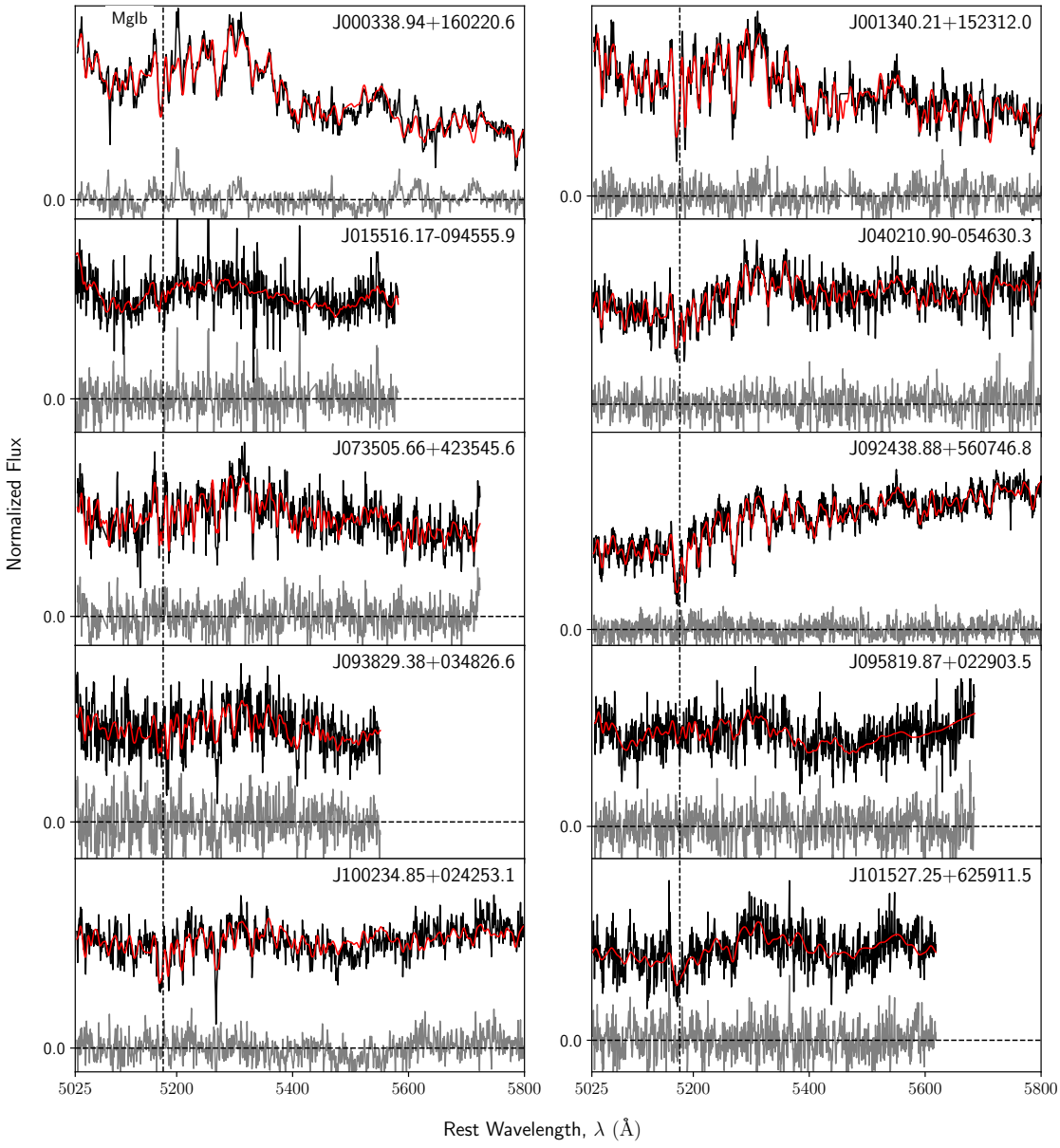

Figure 2.3: Velocity dispersion measurements of the Mg Ib/Fe II region spanning from 5025 to 5800 Å (coverage permitting). Each spectrum (black) are median normalized to 1 for fitting purposes and overplot with the best-fit (red) to the line-of-sight velocity distribution. Residuals are shown below each fit in gray.

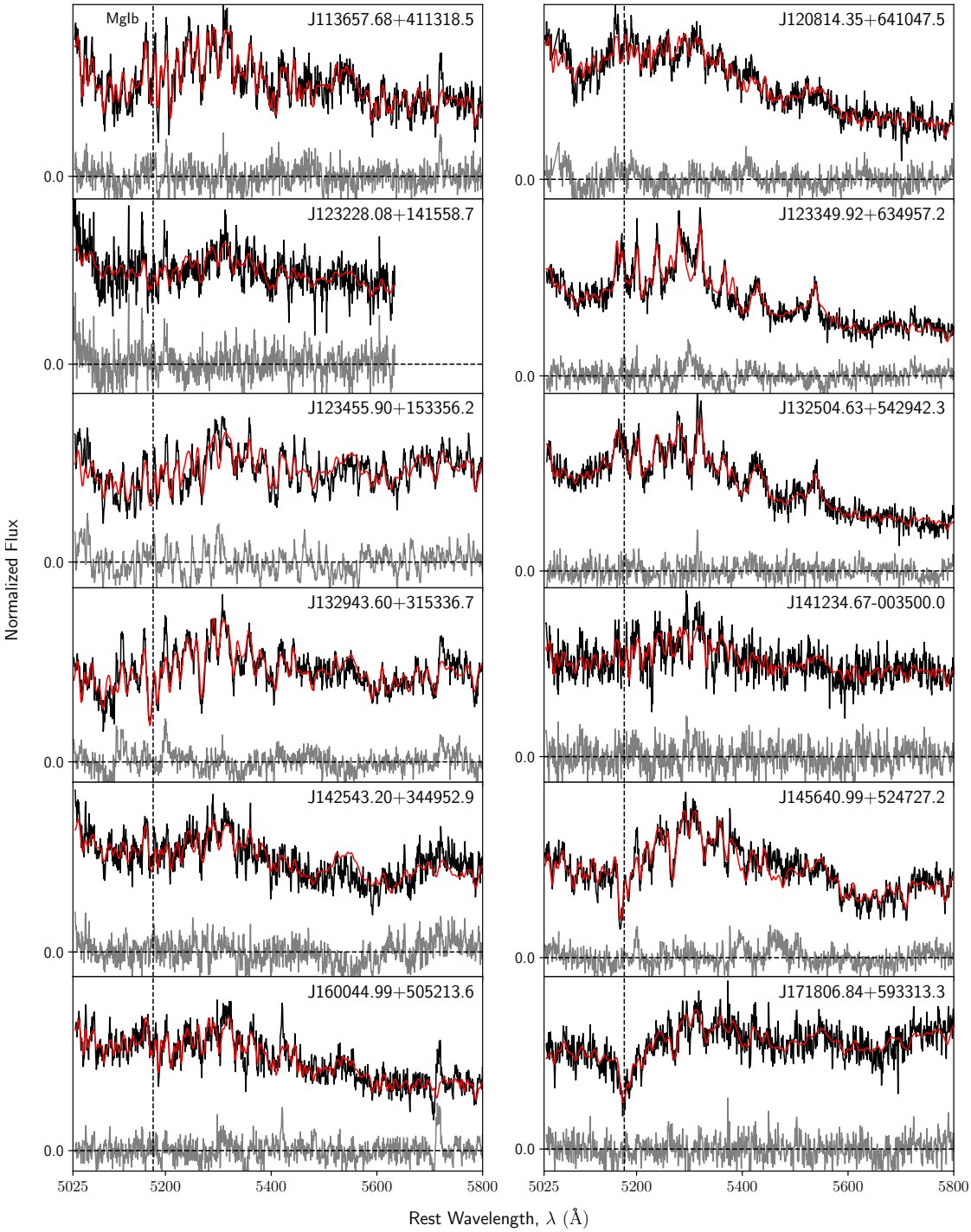

Figure 2.3: *Continued.*

2.3.4 Multi-Component Spectral Fitting

The variable and complex nature of optical AGN spectra necessitate the use of simultaneous multi-component fitting to accurately constrain the relative contributions of each of the spectral components present. As with velocity dispersion measurements, the contribution from broad and narrow Fe II emission can further affect measurements of broad Hβ and [O III] emission features. Broad Fe II emission between Hβ and [O III]λ4959 can cause Hβ to appear more broad and asymmetric if unaccounted for. Similarly, narrow Fe II can be present on either side of [O III]λ5007 and complicate width measurements. In addition to Fe II emission, stellar absorption from the host galaxy can cause significant asymmetries in the line profile of broad Hβ. Finally, the relative strength of the AGN continuum can dilute the strength of stellar continuum, and therefore must be accounted for (Greene & Ho, 2005).

To perform simultaneous fitting of all components, the fitting region is chosen to span from rest-frame $4400 - 5800$ Å, large enough such that the relative contribution from Fe II and stellar emission can be adequately constrained from both sides of the Hβ/[O III] region. The stellar continuum across the fitting region is modeled using the same 636 stellar templates used to measure stellar velocity dispersion; however, we constrain the LOSVD solution to that found in the previous step (see Section 2.3.1) and allow pPXF to determine the best-fit stellar templates to match the spectrum. The Fe II component is modeled using the broad and narrow template from Véron-Cetty et al. (2004). Each Fe II template is parameterized by an amplitude, width, and velocity offset, all of which are free parameters during the fitting process. The AGN continuum is modeled using a simple power law with

an amplitude and power-law index as free parameters. The amplitude is constrained to be positive and the power-law slope is constrained to the range $[-4, 2]$. Finally, broad and narrow Hβ and [O III]$\lambda\lambda$4959, 5007 emission features are fit. The amplitude ratio of the [O III]$\lambda\lambda$4959, 5007 lines were held at a 1:3 constant ratio as per theoretical calculations and empirical observations (Dimitrijević et al., 2007), while the amplitude of the narrow Hβ line was left as a free parameter. The widths of narrow Hβ and [O III]λ4959 were tied to the width of [O III]λ5007. The velocity offsets of the [O III] lines were tied, but the narrow Hβ velocity offset was left as a free parameter. Velocity offsets are measured with respect to best-fit redshift determined from the fit to stellar absorption features described in Section 2.3.1. Blueshifted wing components are included in the fits to narrow emission lines, and are constrained to have a width greater than their narrow core counterpart. If the fitting algorithm cannot adequately fit a blue-wing component with the narrower core emission line, or if the resulting core component has a width less than than the intrinsic FWHM resolution of the instrument configuration, blue-wing components are removed from the model.

All components of the model are fit simultaneously using a custom Bayesian maximum-likelihood algorithm implemented in Python, with uncertainties estimated via Markov Chain Monte Carlo (MCMC) using the affine invariant MCMC ensemble sampler *emcee* (Foreman-Mackey et al., 2013). The small size of our sample allows us to initialize parameters on an individual object basis to ensure accurate modeling of all components. First, an initial model is constructed for the emission lines, Fe II templates, and power-law continuum using reasonable starting values, and are subsequently subtracted off from the original data. The remaining flux, which is assumed to contain a non-negligible fraction of stellar continuum, is

then fit with pPXF (Cappellari & Emsellem, 2004; Cappellari, 2017) to obtain the best-fit stellar templates. Initial conditions for each parameter are determined using a least-squares numerical optimization routine which maximizes the likelihood function given by

$$\chi^2 = \sum_{i=1}^{N} \frac{(y_{\mathrm{data},i} - y_{\mathrm{model},i})^2}{\sigma_i^2}, \tag{2.1}$$

where σ_i is the 1σ uncertainty for each datum $y_{\mathrm{data},i}$, and $y_{\mathrm{model},i}$ is the value of the model at each datum. Upper and lower limits on parameters, for example minimum and maximum broad-line widths, are also chosen to serve as priors to constrain fitting parameters. Once adequate initial values and bounds have been determined, *emcee* is used to sample the parameter space of each parameter to determine their posterior distributions, from which the best-fit values and uncertainties are calculated. The number of MCMC iterations performed is ultimately determined by how well individual model components are initially fit, with the most degenerate components requiring longer runtimes. Each object is fit with a minimum of 2500 iterations, but each parameter generally converges on a solution in less than 1000 iterations.

We find that the use of an MCMC algorithm is advantageous over simpler least-squares methods since the high number of free parameters can lead to numerous degeneracies in parameter solutions thus requiring the algorithm to exhaustively explore each parameter space. Our MCMC implementation allows one to visualize how individual parameters approach or diverge from a solution, or if degeneracies exist. The most common degeneracy observed during the fitting process is that of the width of broad Fe II, which is due to overlapping broad Fe II features; however, we have found that broad Fe II does not strongly

affect stellar velocity dispersion measurements because the features are too broad to mimic narrower stellar absorption features. In general, most degeneracies resolve themselves after a sufficient number of MCMC iterations, usually after higher signal-to-noise ratio (S/N) features, such as emission lines, have converged on a stable solution, allowing less constrained features, such as Fe II or stellar emission, to subsequently converge on their respective solutions. Large degeneracies, if present, emerge in the posterior distributions of each affected parameter, and are reflected in our uncertainties.

Figure 2.4 shows the best-fit model, individual component models, and residuals for each object using our multi-component fitting method. For one object, J145640, the [O III] complex appears to be significantly attenuated, and we therefore mask the [O III] complex during the fitting process. See the Appendix 2.7 for further discussion on the spectrum and fitting of object J145640.

2.3.4.1 Measuring Broad Hβ FWHM

A number of objects in our sample exhibit asymmetric broad Hβ emission lines. Ordinarily, such an asymmetric profile would require multiple Gaussian components or fitting the dispersion directly from the line profile. However, the inclusion of the stellar continuum and Fe II emission, and modeling the line with a single Gaussian, fully accounts for any asymmetries or non-Gaussian shape in the line profile. Prominent examples of this asymmetry are shown in the spectra of J000338, J100234, J145640, and J171806. We find that the multi-component fitting technique is consistent with techniques that do not fit the stellar continuum or Fe II emission simultaneously. We find that uncertainties in Hβ line widths

decrease by a factor of 2.3 on average for our sample compared to line widths measured conventionally where multi-component fitting is not implemented. This is likely due to the requirement of a more complex line models (two or more Gaussian components) needed to fully account for the asymmetric broad Hβ profile. Uncertainties in the fit for broad Hβ widths in our sample range from 1% to 6%, and depend largely on the S/N of the spectrum and how well other components of the model are constrained.

Variability of the line profile of Hβ can also contribute to the random uncertainties of single-epoch width measurements. Woo et al. (2007) found a 7% rms scatter when comparing Lick rms Hβ FWHM measurements to Keck single-epoch measurements, which we adopt in our random uncertainties for measured Hβ FWHM. The total random uncertainty for our Hβ FWHM measurements is $\sim$8%.

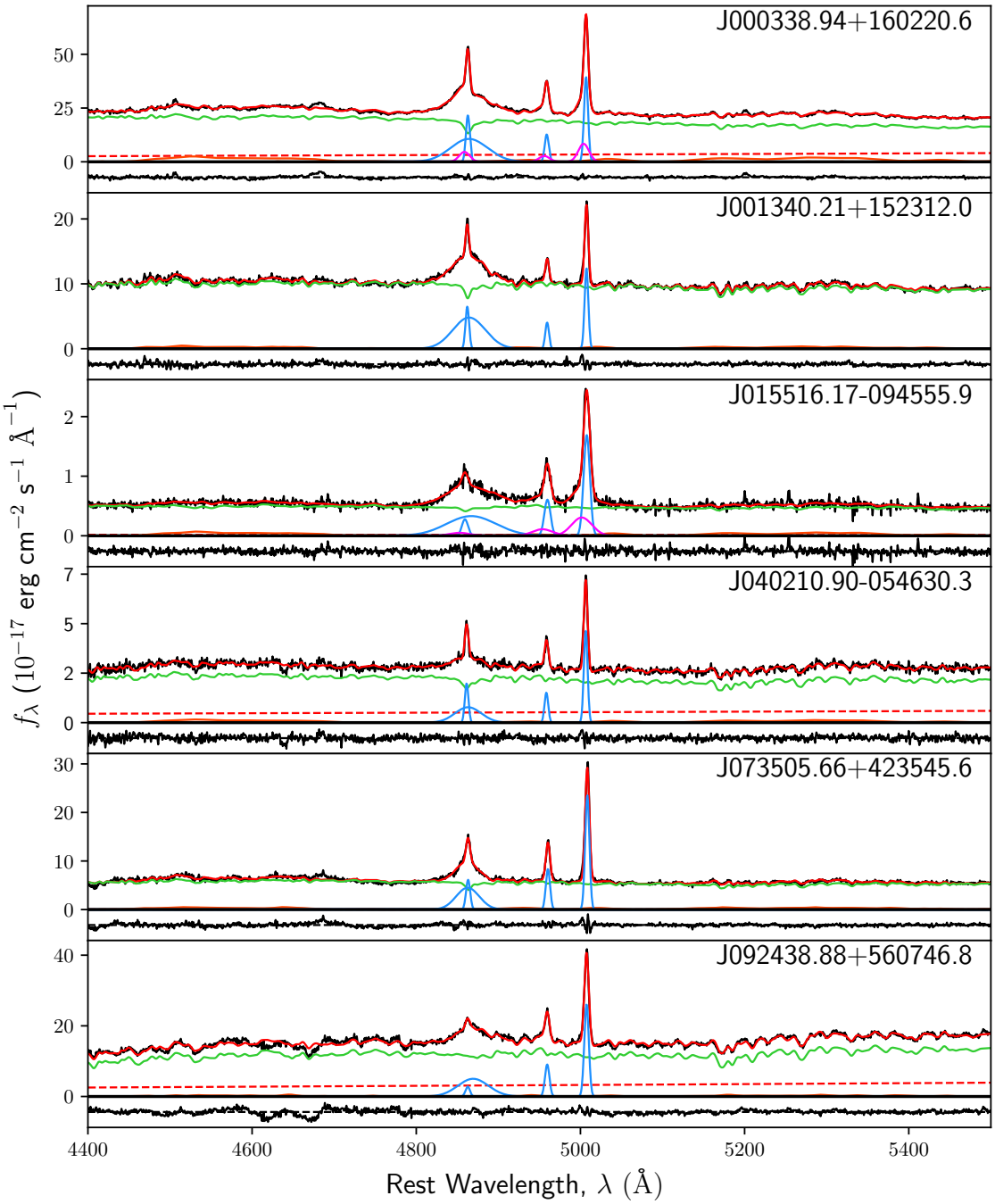

Figure 2.4: Multi-component fitting of the the Hβ/[O III] region. The reduced Keck/LRIS spectra (black) are overplotted with the total best-fit model (red), comprised of the stellar continuum (green), the AGN power-law continuum (dashed red), broad and narrow Fe II emission (orange), broad and narrow emission lines (blue) and their corresponding blue-wing outflow components (magenta) if present. Residuals are shown below each spectrum.

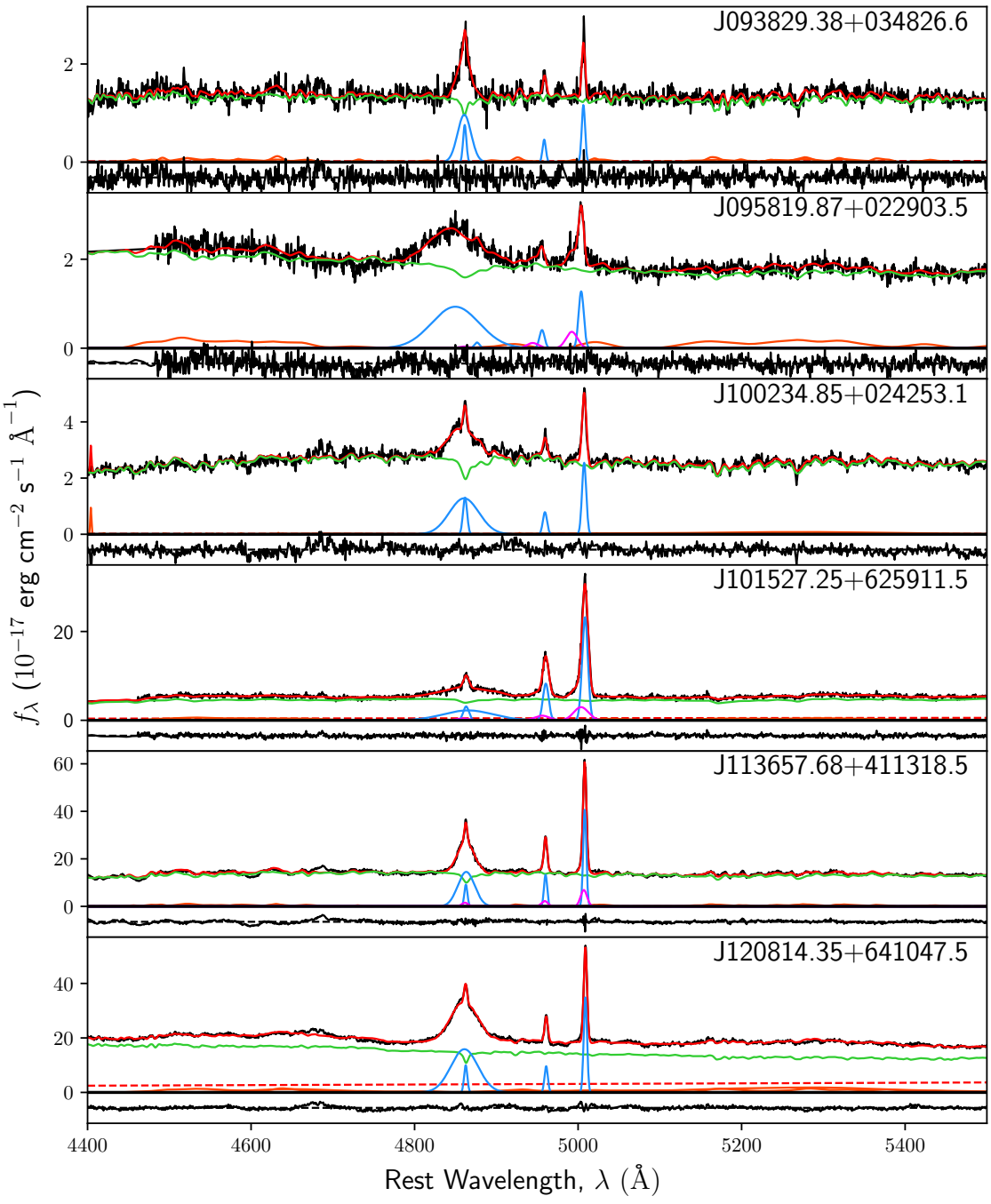

Figure 2.4: *Continued.*

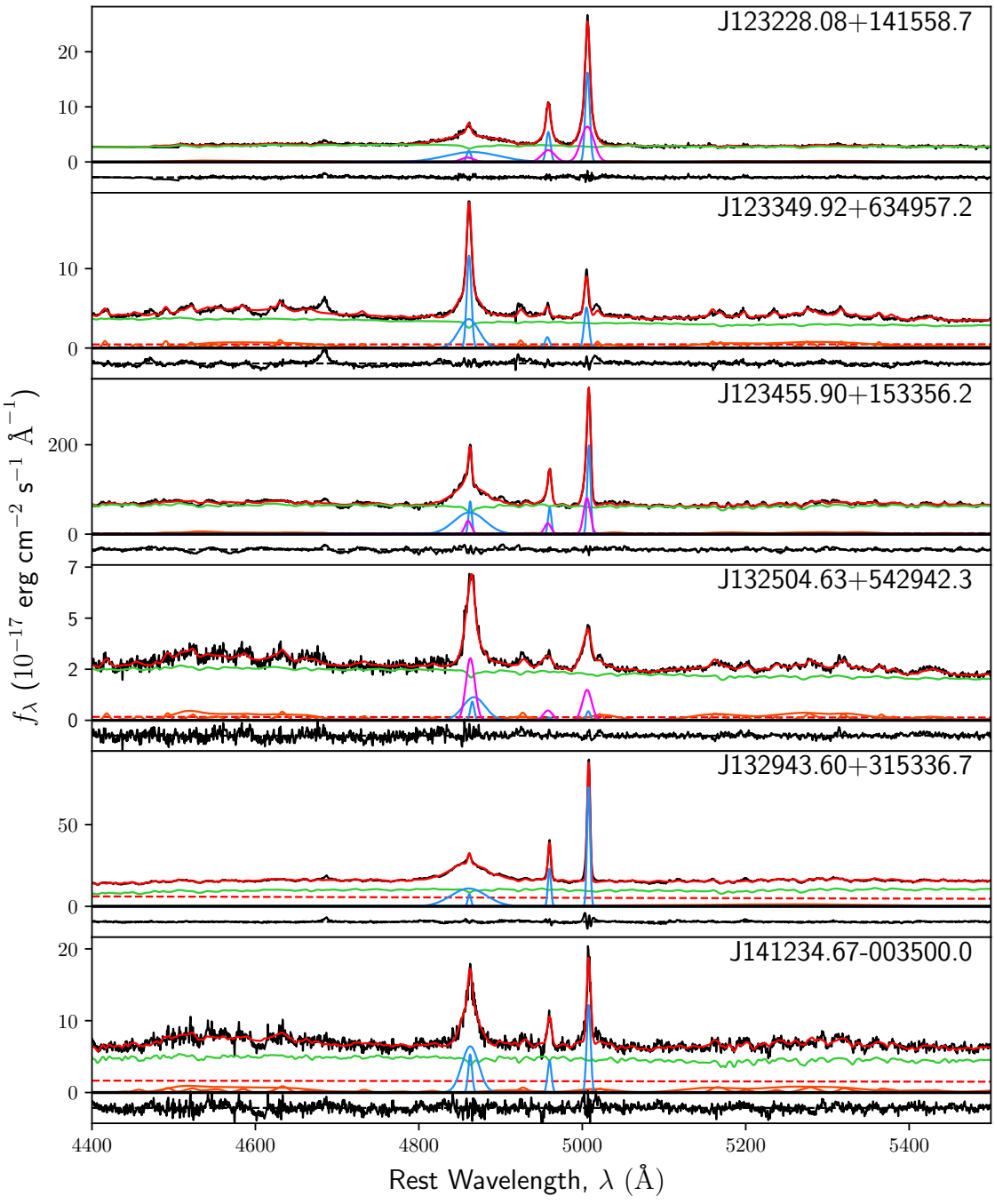

Figure 2.4: *Continued.*

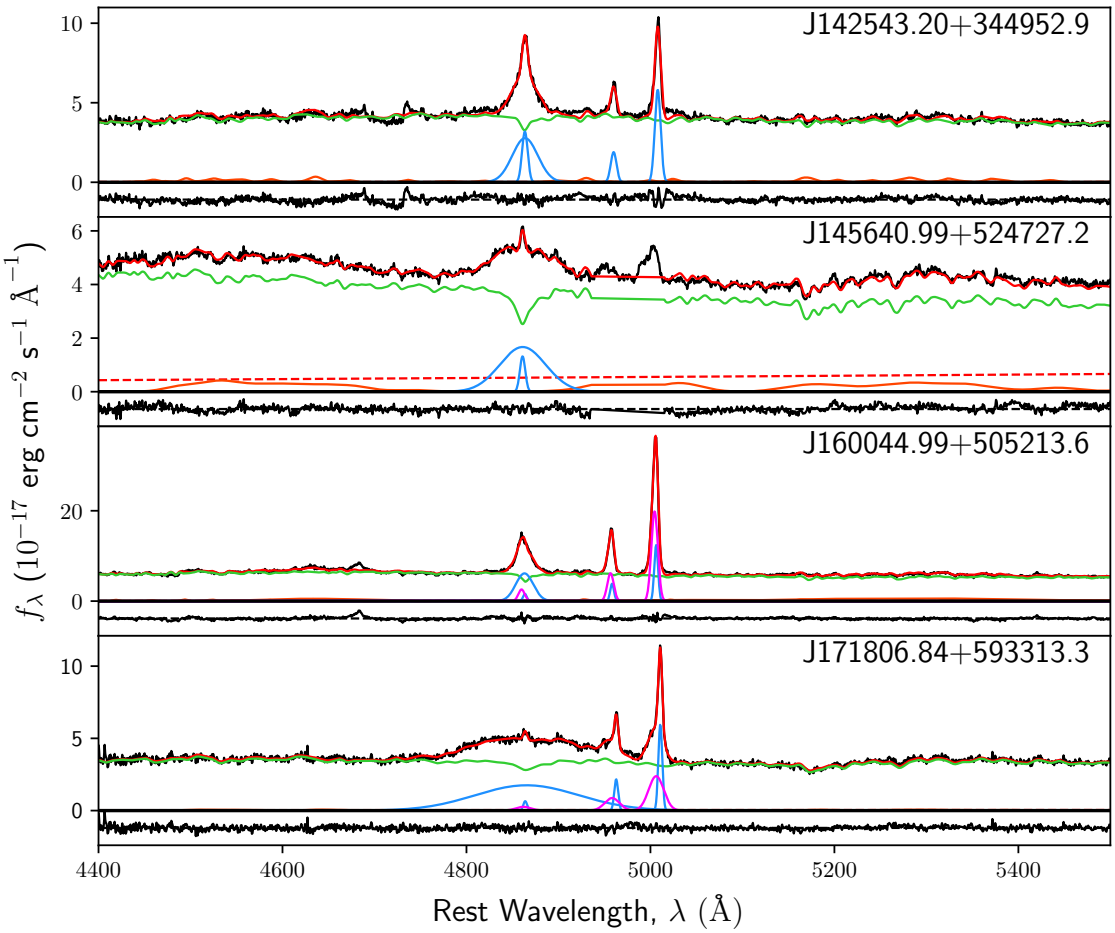

Figure 2.4: *Continued.*

2.3.4.2 [O III] as a Surrogate for Stellar Velocity Dispersion

Measurements of stellar velocity dispersion for Type 1 AGNs at $z > 0.4$ are often complicated by the large light fraction from the AGN coupled with surface brightness dimming of the host galaxy, resulting in stellar absorption features that are difficult or impossible to measure. Previous studies have suggested that the widths of strong narrow-line region (NLR) emission lines, such as [O III]λ5007, may be suitable surrogates for the stellar velocity dispersion if the NLR velocity field is strongly coupled with the gravitational potential of

the bulge (Nelson & Whittle, 1996). However, non-gravitational kinematic components in ionized-gas emission can be present, manifested as a broad and blueshifted wing component indicative of possible gas outflows (Heckman et al., 1980; Nelson & Whittle, 1996). Non-gravitational kinematics can also manifest themselves as a blueshift of the entire [O III] line profile, which comes with a dramatic line profile broadening (Komossa et al., 2008a, 2018), again likely indicating strong outflows. Studies with large surveys such as the SDSS show considerable scatter in a linear relation between $\sigma_{[\mathrm{O\ III}]}$ and σ_*, even after blue-wing outflow components have been removed (Boroson, 2003; Greene & Ho, 2005). However, the scatter decreases significantly after removing sources which have their whole [O III] line profile blueshifted (so-called "blue outliers"; Figure 1 of Komossa & Xu (2007)). More recently, Woo et al. (2016) investigated [O III]λ5007 kinematics in a sample of $\sim$39,000 Type 2 AGNs at $z < 0.3$, accounting for outflows in $\sim$44% of their sample. In addition to confirming a broad correlation between $\sigma_{[\mathrm{O\ III}]}$ and σ_*, they found that objects with non-gravitational outflow components do not follow a linear correlation, and instead have higher $\sigma_{[\mathrm{O\ III}]}/\sigma_*$ ratios for higher σ_*. In a subsequent study, Rakshit & Woo (2018) found similar results to Woo et al. (2016) for $\sim$ 5000 Type 1 AGNs. Bennert et al. (2018) also performed a comprehensive analysis on the use of [O III] as a surrogate for σ_* on the $M_{\mathrm{BH}} - \sigma_*$ relation, finding that there is good statistical agreement between relations plotted with $\sigma_{[\mathrm{O\ III}]}$ versus σ_*, but only after blueshifted wing components are removed.

Higher-resolution spectra allow us the opportunity to revisit the significance of any correlation between $\sigma_{[\mathrm{O\ III}]}$ and σ_*, as well as investigate the influence, and possible bias, outflow components may introduce. In addition to fitting for outflow kinematics in [O III],

we attempt to fit for any broad or narrow Fe II contamination within the Hβ region which may bias measurements of [O III] to higher widths.

Out of the 22 objects in our sample, 10 objects exhibit line-profile asymmetry in [O III] consistent with a blueshifted wing component. Following Woo et al. (2006), we compare the [O III]λ5007 dispersion $\sigma_{[\mathrm{O\ III}]}$ as a function of stellar velocity dispersion σ_* using three methods: (1) fitting a single-Gaussian model, (2) measuring the flux-weighted dispersion of the full line profile, and (3) fitting a double-Gaussian model. The flux-weighted dispersion is calculated using the same method as Woo et al. (2016), which calculated the second-order Gaussian moment of the sum of the full (core+blue wing) best-fit model to [O III]λ5007. The double-Gaussian model is a decomposition of the broader blue-wing component from the narrower core component, and the core component is chosen as the proxy for σ_*. The single-Gaussian fit results in slight disagreement with σ_*, with a mean of 0.079 ± 0.038 and RMS of 0.155 ± 0.031 in $\log_{10}(\sigma_{[\mathrm{O\ III}]}/\sigma_*)$. The flux-weighted measurements result in worse agreement with a mean of 0.17 ± 0.04 and comparable RMS. Flux-weighted measurements produce, on average, higher widths than the single-Gaussian model, due to the inclusion of flux from the blue-wing component. The best agreement with σ_* resulted from the double-Gaussian decomposition of the [O III] line profile, with a mean of 0.004 ± 0.044 and an RMS of 0.187 ± 0.034. Despite the extra consideration in taking into account the stellar and Fe II components, the RMS scatter is consistent with respect to σ_* for all three fitting methods. In the best case we find that a double-Gaussian decomposition of the [O III] line profile results in a $\sim$30% difference with respect to σ_* on average for our sample. Despite its limited size, our sample covers a wide range in σ_*, and we

find good agreement with Bennert et al. (2018) that there is good statistical agreement on average when using [O III] as a surrogate for σ_*, provided that blueshifted wing components are removed and Fe II contamination is accounted for. Komossa & Xu (2007) traced back the remaining offsets in NLS1s to the effect of [O III] blue outliers in those NLS1s. Once removed, $\sigma_{[\mathrm{O\ III}]}$ and σ_* showed similar scatter. Of the three deviating NLS1s in our sample (rightmost panel of Figure 2.5), only one shows a significant kinematic shift in [O III] with respect to stellar absorption features. We did not find any other trends with blue outliers in our sample which can further reduce the scatter. We therefore caution the use of the [O III] line as a reliable surrogate for σ_*, and agree with Bennert et al. (2018) in that it should only be used in a statistical - and not individual - proxy for σ_* on the $M_{\mathrm{BH}} - \sigma_*$ relation.

2.3.5 Surface Brightness Decomposition

To obtain a robust measure of the AGN luminosity, archival *HST* imaging was used for accurate deconvolution of the AGN PSF uncontaminated by the host galaxy. To do this, we used the two-dimensional surface brightness fitting algorithm GALFIT (Peng et al., 2011), which convolves a given PSF with an analytical model (e.g., disk, exponential, Sérsic, etc.) to estimate model parameters, such as flux and effective radius, of the surface brightness profile of a galaxy.

Accurate deconvolution of galaxy surface brightness components requires a PSF that closely matches the signal response particular to each image. Additionally, each image undergoes numerous transformations during the data reduction process or suffers from age-dependent peculiarities (such as degrading charge transfer efficiency). We determine that

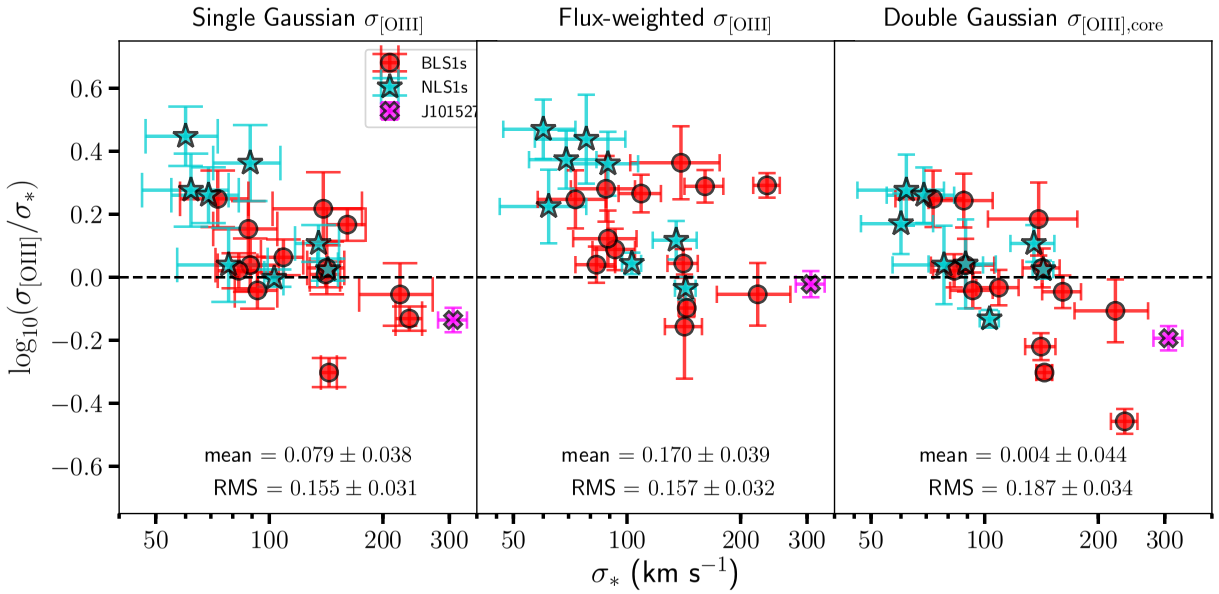

Figure 2.5: Comparisons of different models for $\sigma_{[\mathrm{O\ III}]}$ vs. σ_*. Left: single-gaussian model from which $\sigma_{[\mathrm{O\ III}]}$ is measured from the FWHM. The offset mean is caused by the presence of asymmetric blue wings which act to increase the width of the line profile. Center: the flux-weighted dispersion, which is more sensitive to the presence of blue-wing profiles than the single-gaussian model. Right: double-gaussian decomposition of the line profile, which results in the best agreement with σ_* on average.

an empirical PSF is the best suited to match each image. Ideally, the empirical PSF would be obtained from a stellar PSF from the same image data as each galaxy; however, in some cases where the galaxy was imaged with the WFPC2/PC instrument, stellar PSFs were not available. In these cases, we obtain stellar PSFs from an image of the same instrument, camera, filter, exposure time, and observation date. We use *sewpy*, a Python wrapper for SExtractor (Bertin & Arnouts, 1996) to identify stellar sources within each HLA image. The brightest of these sources are examined by eye to insure each extraction is free of background contamination or saturation, and then stacked to obtain an average empirical PSF of the image. The HLA pipeline also provides a separate image of the 1σ uncertainty for each science image, which is needed as input for GALFIT. Segmentation masks are also created using SExtractor to mask contaminating objects (other galaxies or stars) and fed into GALFIT. Segmentation maps allow us to maximize the size of the usable image for GALFIT to accurately fit the background.

An iterative process was used to determine the number of models used to decompose each object. Each object was initially given a PSF component to model the AGN contribution, a single Sérsic model (Sérsic, 1963) for the host galaxy, and a background sky component. Residuals were then examined to determine if an additional Sérsic component was necessary, such as in the case of a disk component. Initially, we allow the Sérsic index for the host galaxy components to be a free parameter if it converges on a Sérsic index of $2 < n < 6$ for a bulge or $0.9 < n < 2$ for a disk component (Fisher & Drory, 2008; Gadotti, 2009), and reinforce these using soft constraints. If GALFIT does not freely converge on a reasonable Sérsic index consistent with a bulge component, the object is refit with the

Sérsic index held constant to a value of $n = 4$. This behavior occurs when GALFIT cannot reconcile contaminating sky or neighboring flux with the extended profiles of high Sérsic index models. For the majority of cases in our sample, a free Sérsic index reaches the upper boundary of the Sérsic index constraint, which is resolved by holding the Sérsic index constant and/or including additional components. Residuals are visually inspected and additional components are added when necessary. Sérsic components that do not satisfy the aforementioned definitions of a bulge or disk are designated as "other".

The results of the surface brightness decomposition for each object are listed in Table 2.3. Reported magnitudes and surface brightness values from GALFIT are corrected for Galactic extinction, intrinsic host galaxy extinction using the Balmer decrement, and k-corrected. The uncertainties output by GALFIT unrealistically assume that any residual flux in the image is due purely to Poisson noise, and does not take into account deviations from the Sérsic model which may be due to spiral arms, dust lanes, star-formation regions, or neighboring flux. As a result, uncertainties quoted by GALFIT in magnitude measurements are generally low, ~ 0.02 mag on average. Masking was used to mediate any possible contaminating flux near our objects. In general, we find that higher surface brightness components, such as the PSF and bulge, have lower quoted uncertainties than lower surface brightness components, such as disks. With the exception of disturbed systems in our sample, the residuals of the surface brightness decompositions shown in Figure 2.6 would indicate fluctuations in the residuals are on the order of ~ 0.1 mag, which we include in our uncertainties. Mismatch between the empirical PSF and the intrinsic PSF of the image can be another significant source of uncertainty of our measurements. Following Canalizo

et al. (2012), we performed direct subtraction of the PSF to determine the upper and lower bounds of the residual flux and found that the average uncertainty in PSF mismatch to be $\sim$0.1 mag, in agreement with Canalizo et al.

Table 2.3: Results from surface brightness profile measurements Using GALFIT. Column 1: object. Column 2: *HST* filter. Column 3: morphological component type from surface brightness decomposition. Column 4: extinction-corrected and k-corrected ST magnitude. Column 5: dust extinction-corrected and k-corrected effective surface brightness. Column 6: effective radius in arcseconds. Column 7: effective radius in kiloparsecs. Column 8: morphological component Sérsic index.

Object	Filter	Comp.	$m_{\rm ST}$ (mag)	$\mu_{\rm eff}$ ($\frac{\rm mag}{\rm arcsec^2}$)	$r_{\rm eff}$ ($''$)	$r_{\rm eff}$ (kpc)	n
J000338.94+160220.6	F606W	PSF	19.38				
		Bulge	17.47	21.60	1.63 ± 0.02	3.39 ± 0.04	5.93
		Other	17.95	17.94	8.51 ± 0.23	17.69 ± 0.47	2.54
J001340.21+152312.0	F475W	PSF	19.79				
		Bulge	17.89	23.45	2.60 ± 0.06	5.55 ± 0.13	5.31
J015516.17-094555.9	F110W	PSF	24.36				
		Bulge	21.72	22.05	0.31 ± 0.01	1.99 ± 0.03	4 (fixed)
		Disk	22.37	24.57	1.03 ± 0.02	6.69 ± 0.12	1 (fixed)
J040210.90-054630.3	F606W	PSF	21.68				
		Bulge	19.60	23.43	1.46 ± 0.05	6.00 ± 0.18	4 (fixed)
		Other	19.40	22.01	1.21 ± 0.01	4.98 ± 0.03	0.46
J073505.66+423545.6	F814W	PSF	20.55				
		Bulge	18.70	19.78	0.35 ± 0.02	0.56 ± 0.04	4 (fixed)
		Other	18.97	22.42	1.51 ± 0.02	2.40 ± 0.03	0.82
J092438.88+560746.8	F814W	PSF	20.81				
		Bulge	14.19	23.32	18.18 ± 0.44	9.20 ± 0.22	4.86
		Sp. Arm	16.66	21.49	6.48 ± 0.72	3.28 ± 0.36	0.14
		-B. Mode		1: -61.5, 2.7	(shear)	3: 27.4, 0.1	(S-shape)
		Disk	14.94	23.74	41.99 ± 0.94	21.25 ± 0.48	1.02
J093829.38+034826.6	F814W	PSF	21.19				
		Bulge	20.15	20.94	0.33 ± 0.04	0.71 ± 0.09	4 (fixed)
		Other	19.04	21.93	1.25 ± 0.01	2.66 ± 0.01	0.6
J095819.87+022903.5	F814W	PSF	20.93				
		Bulge	20.94	21.73	0.50 ± 0.04	2.45 ± 0.21	4 (fixed)
		Disk	18.89	22.16	1.52 ± 0.01	7.40 ± 0.03	1 (fixed)
J100234.85+024253.1	F814W	PSF	22.06				
		Bulge	20.59	22.18	0.78 ± 0.04	2.52 ± 0.14	4 (fixed)
		Disk	19.16	22.68	1.60 ± 0.01	5.14 ± 0.02	1 (fixed)
J101527.25+625911.5	F775W	PSF	20.45				
		Bulge	18.55	21.81	1.19 ± 0.01	5.85 ± 0.06	4 (fixed)
		Disk	19.21	24.18	4.54 ± 0.05	22.28 ± 0.24	1 (fixed)
J113657.68+411318.5	F814W	PSF	20.35				
		Disk	18.44	20.67	0.98 ± 0.01	1.32 ± 0.01	1.38
J120814.35+641047.5	F814W	PSF	19.52				
		Bulge	18.22	23.32	2.29 ± 0.05	4.37 ± 0.10	4 (fixed)
		Other	19.57	21.82	1.24 ± 0.01	2.37 ± 0.02	0.11
J123228.08+141558.7	F606W	PSF	20.44				
		Bulge	18.85	21.69	0.90 ± 0.03	5.02 ± 0.17	4 (fixed)
J123349.92+634957.2	F814W	PSF	20.45				
		Bulge	20.80	21.26	0.34 ± 0.04	0.79 ± 0.09	4 (fixed)
		Disk	19.41	22.41	1.31 ± 0.01	3.06 ± 0.03	0.99
J123455.90+153356.2	F814W	PSF	18.48				
		Bulge	16.11	22.26	4.60 ± 0.14	4.09 ± 0.13	4 (fixed)
		Other	18.41	17.17	0.21 ± 0.00	0.19 ± 0.00	0.41
		Other	15.39	21.73	6.70 ± 0.01	5.95 ± 0.01	0.43
J132504.63+542942.3	F814W	PSF	20.31				
		Bulge	20.66	18.21	0.08 ± 0.01	0.19 ± 0.02	4 (fixed)
		Other	18.76	21.57	1.15 ± 0.02	2.95 ± 0.04	1.85

Table 2.3: *Continued.*

Object	Filter	Comp.	$m_{\rm ST}$ (mag)	$\mu_{\rm eff}$ ($\frac{\rm mag}{\rm arcsec^2}$)	$r_{\rm eff}$ ($''$)	$r_{\rm eff}$ (kpc)	n
J132943.60+315336.7	F814W	PSF	20.28				
		Bulge	17.63	18.78	0.43 ± 0.02	0.74 ± 0.03	4 (fixed)
		Other	18.64	21.08	1.55 ± 0.01	2.63 ± 0.01	0.16
		Other	17.69	22.75	4.31 ± 0.01	7.33 ± 0.02	0.23
J141234.67-003500.0	F814W	PSF	20.63				
		Bulge	19.18	23.87	2.61 ± 0.04	5.84 ± 0.09	4 (fixed)
		Other	18.55	22.57	2.86 ± 0.00	6.40 ± 0.01	0.4
J142543.20+344952.9	F814W	PSF	20.90				
		Bulge	19.34	20.33	0.40 ± 0.01	1.20 ± 0.04	4 (fixed)
		Other	20.16	22.45	1.28 ± 0.01	3.82 ± 0.04	0.39
J145640.99+524727.2	F606W	PSF	20.86				
		Bulge	19.22	19.99	0.51 ± 0.02	2.16 ± 0.06	4 (fixed)
		Disk	18.16	21.26	1.22 ± 0.01	5.11 ± 0.02	1 (fixed)
J160044.99+505213.6	F814W	PSF	20.99				
		Bulge	19.34	19.80	0.30 ± 0.02	0.55 ± 0.04	4 (fixed)
		Other	19.08	21.08	0.85 ± 0.01	1.55 ± 0.01	0.77
J171806.84+593313.3	F814W	PSF	21.87				
		Bulge	19.05	22.35	1.15 ± 0.01	4.74 ± 0.03	3.9

2.3.6 Measuring λL_{5100}

Surface brightness decomposition of *HST* imaging using GALFIT was used to obtain an estimate of the optical continuum AGN luminosity at 5100 Å, uncontaminated by the host galaxy. To do this, the AGN component is modeled using a single PSF component, and other Sérsic components are added to minimize residuals (see Section 2.3.5). The PSF magnitudes are then corrected for Galactic extinction, intrinsic host galaxy extinction using the Balmer decrement, and k-corrected. To obtain the luminosity at 5100 Å , we model the full (LRIS-B + LRIS-R) spectrum for each object using the IDL-based multi-component quasar spectrum fitting software QSFit (Calderone et al., 2017). QSFit differs from the multi-component fitting method described in Section 2.3.4 in that it only fits a single galaxy template and uses a least-squares minimization technique, providing a means to fit full

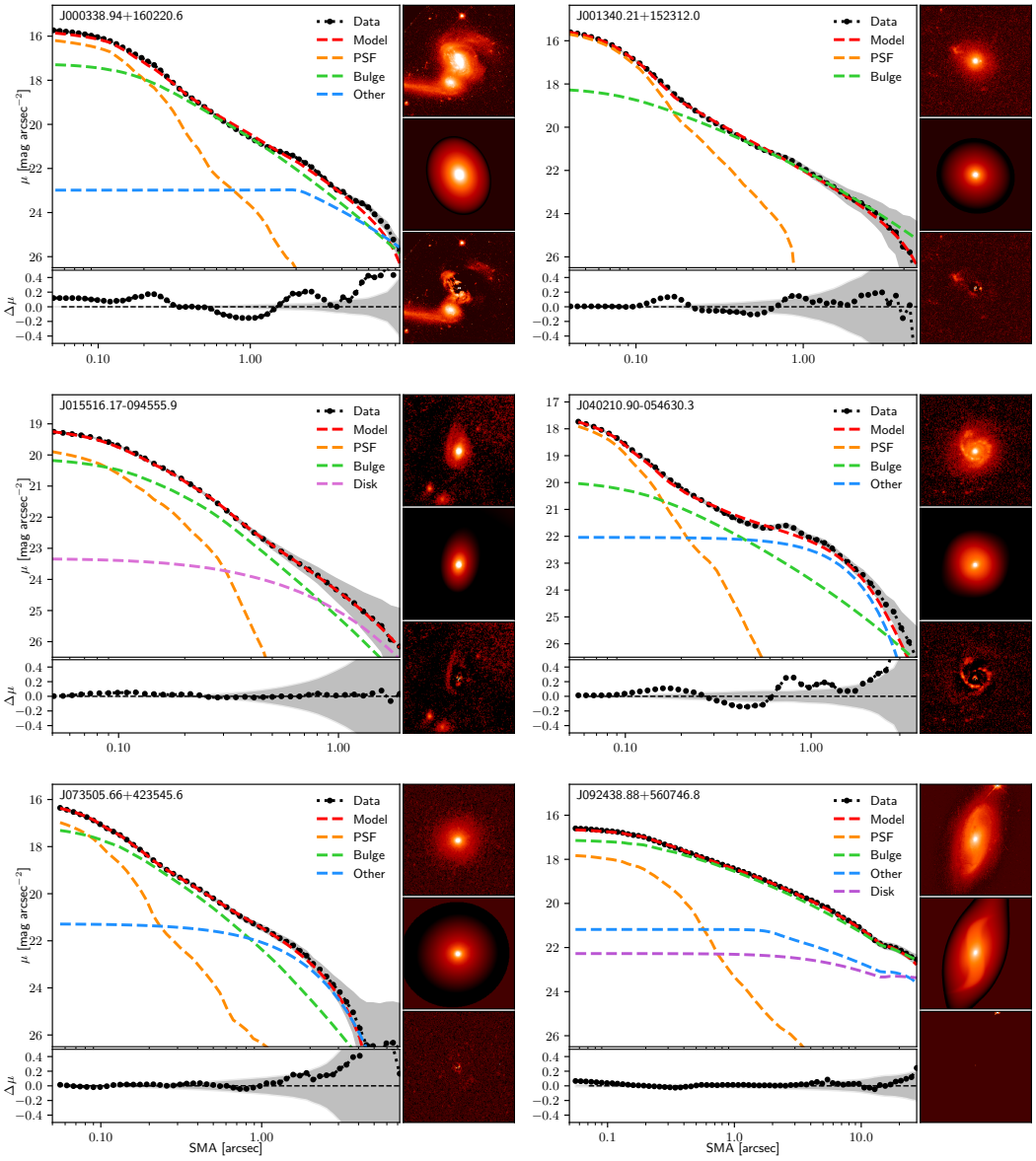

Figure 2.6: Surface brightness decomposition of the AGN from the host galaxy for our sample. The large inset is the surface brightness profile, including each of the modeled components, with residuals plotted in the inset below. The gray shaded region represents the 1σ uncertainty. On the right, from top to bottom, the *HST* image of each object, the model output from GALFIT, and the corresponding residuals.

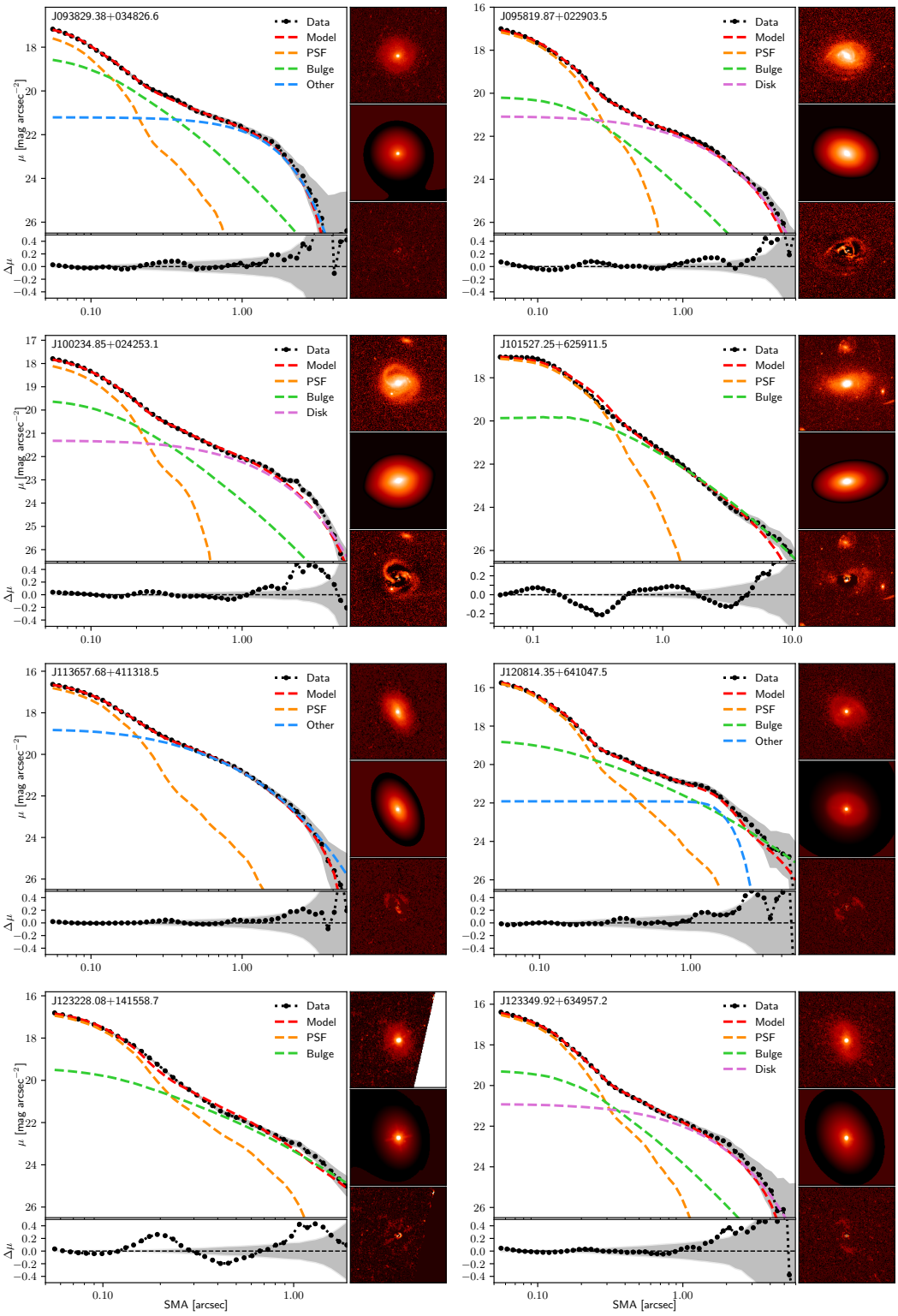

Figure 2.6: *Continued.*

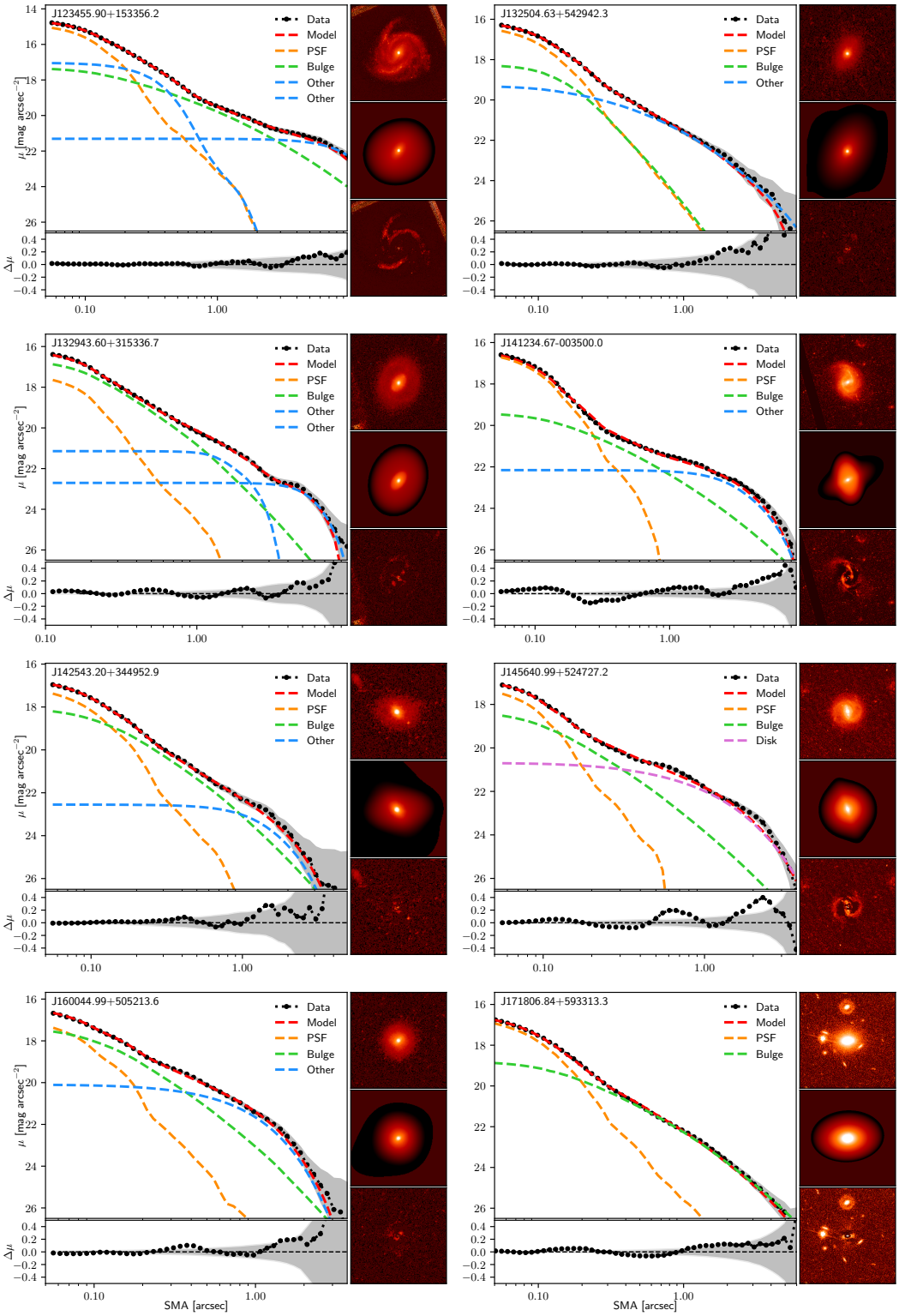

Figure 2.6: *Continued.*

spectra with a large number of free parameters in a computationally efficient way. Using QSFIT, we fit each object's full spectrum (shown in Figure 2.2) with the default settings, which include a 5 Gyr elliptical galaxy template (Silva et al., 1998; Polletta et al., 2007), Fe II templates from (Véron-Cetty et al., 2004), a simple power-law model for the AGN continuum, and all known emission lines from 3500 to 7000 Å . Uncertainties in the power-law slope were estimated using the Monte Carlo resampling option included in QSFIT. The power-law model was then used to scale the AGN luminosity at the observed *HST* filter wavelength to a luminosity at 5100 Å. Using this method, we expect uncertainties in λL_{5100} to be smaller if the pivot wavelength of the *HST* filter is close to 5100 Å, while filters with pivot wavelengths farther from 5100 Å are dependent on how accurately the AGN continuum model can be determined (i.e., the slope of the adopted simple power-law continuum model). The use of a single host galaxy template does not have a significant effect on our measurements since luminosities measured from *HST* imaging are measured at filter pivot wavelengths close to - but typically at longer wavelengths than - 5100 Å, where the effects of the power-law slope vary appreciably less than at shorter wavelengths.

Uncertainty in measured luminosities due to variability can be appreciable and vary significantly (5-30%) from object to object. Detailed analysis on the flux variability of our objects would require detailed reverberation mapping which is currently unavailable. We therefore adopt a median uncertainty of 15% from reverberation-mapped objects from Bentz et al. (2013) as an additional uncertainty due to AGN variability.

We estimated the total uncertainty in our measured luminosities to be ∼30% on average for our sample. Measured values of λL_{5100} are given in Table 2.4.

2.3.7 BH Mass

Single-epoch BH masses are estimated using the virial relation commonly used within the context of reverberation studies (see Peterson (2004)) given as

$$M_{\rm BH} = f\frac{(\Delta V)^2 R_{\rm BLR}}{G} \tag{2.2}$$

where f is the virial coefficient, ΔV velocity of the BLR gas at radius $R_{\rm BLR}$, and G is the gravitational constant. The $R_{\rm BLR}$ is estimated empirically via proxy using the optical luminosity of the AGN (Kaspi et al., 2000, 2005; Bentz et al., 2009, 2013). Following Woo et al. (2015), we adopt the most recent measurements of the $R_{\rm BLR} - \lambda L_{5100}$ relation from Bentz et al. (2013) given as

$$\log\left(\frac{R_{\rm BLR}}{\text{1lt-day}}\right) = K + \alpha\log\left(\frac{\lambda L_{5100}}{10^{44}\ \text{L}_\odot}\right) \tag{2.3}$$

where $K = 1.527^{+0.031}_{-0.031}$ is the zero point, and $\alpha = 0.533^{+0.035}_{-0.033}$ is the slope of the log-linear relation. The velocity of the BLR is typically measured via the line dispersion $\sigma_{\rm H\beta}$; however, it is often easier to measure FWHM$_{\rm H\beta}$ in low-S/N spectra and convert to $\sigma_{\rm H\beta}$ using a constant factor. It is well known that the FWHM/σ ratio is velocity dependent (Peterson, 2004; Collin et al., 2006; Kollatschny & Zetzl, 2011). To account for any systematic uncertainties in choice of velocity proxy, Woo et al. (2015) derived separate virial coefficients for $\sigma_{\rm H\beta}$ and FWHM$_{\rm H\beta}$. Since our sample consists of spectra with variable S/N, we measure line widths using a Gaussian FWHM and adopt the appropriate virial coefficient of $\log f = 0.05 \pm 0.12$ from Woo et al. (2015). By adopting the aforementioned relations, the BH mass equation

becomes

$$M_{\rm BH} = 10^{6.867^{+0.155}_{-0.153}} \left(\frac{\rm FWHM_{H\beta}}{10^3 \text{ km s}^{-1}} \right)^2 \left(\frac{\lambda L_{5100}}{10^{44} \text{ erg s}^{-1}} \right)^{0.533^{+0.035}_{-0.033}} \text{M}_\odot \tag{2.4}$$

Values for calculated BH masses for our sample can be found in Table 2.4. The uncertainties quoted for BH mass in Table 2.4 include uncertainties from measurements of $\rm FWHM_{H\beta}$ and λL_{5100}, as well as the uncertainties derived from the virial coefficient f and the $R_{\rm BLR} - \lambda L_{5100}$ relation. The most significant contribution to the uncertainties in BH mass is derived from the calibration of the virial coefficient f.

2.4 Results

2.4.1 The $M_{\rm BH} - \sigma_*$ Relation

We plot the results of our measurements for the $M_{\rm BH} - \sigma_*$ relation in Figure 2.7. We include other non-local objects from previous studies of red 2MASS quasars at $0.14 < z < 0.37$ (Canalizo et al., 2012), post-starburst quasars at $z \sim 0.3$ (Hiner et al., 2012), Seyfert 1 galaxies at $z = 0.36$ and $z = 0.57$ (Woo et al., 2006, 2008), as well as local and non-local reverberation-mapped AGN samples from Woo et al. (2015) and Shen et al. (2015), respectively, for comparison.

To compare our measurements to the local relation, we recalculate BH masses for all objects with $z < 0.1$ for the combined sample of AGNs from Bennert et al. (2011a), local inactive galaxies from McConnell & Ma (2013), and local reverberation-mapped BH masses

from Woo et al. (2015) using the most recent BH mass calibration from Woo et al. (2015), which adopts a virial coefficient of $\log f = 0.05 \pm 0.12$ for Hβ line widths measured using a Gaussian FWHM. The local comparison sample consists of a total of 124 objects ranging in mass from 6.1 to 10.3 in $\log_{10}(M_{\rm BH})$. We perform linear regression using a maximum-likelihood approach and estimate uncertainties using MCMC. The linear fit to the local $M_{\rm BH} - \sigma_*$ relation is given by

$$\log_{10}\left(\frac{M_{\rm BH}}{M_\odot}\right) = (8.323^{+0.046}_{-0.046}) + (4.613^{+0.230}_{-0.231}) \log_{10}\left(\frac{\sigma_*}{200 \text{ km s}^{-1}}\right) \tag{2.5}$$

with an intrinsic scatter of $\epsilon_0 = 0.427^{+0.033}_{-0.032}$. The best-fit local relation is plotted as a black dashed line, and the 68% confidence interval is given by the dotted lines and shaded region in Figure 2.7. Our local relation has a shallower slope than that of McConnell & Ma (2013) ($\beta = 5.64 \pm 0.32$) and is nearly consistent with that of the Woo et al. (2015) updated reverberation-mapped sample ($\beta = 4.97 \pm 0.28$). Additionally, we plot the relation from Kormendy & Ho (2013) (red dashed line), which measured local BH masses in inactive galaxies using stellar and gas kinematics. Since single-epoch BH masses are calibrated using local inactive galaxies, the good agreement between the Kormendy & Ho (2013) relation and our local relation indicates that BH masses for AGNs are well-calibrated.

The 22 objects in our sample span a mass range of two orders of magnitude from 6.1 to 8.3 in $\log_{10}(M_{\rm BH})$. The mean offset of our sample from the local relation is $-0.018^{+0.111}_{-0.108}$ dex, with a scatter of $0.385^{+0.099}_{-0.112}$ dex. The scatter in our sample is comparable to that of the 0.43 ± 0.03 dex found for local reverberation-mapped objects (Woo et al., 2015) as well as the 0.38 dex for objects from stellar dynamical measurements (McConnell & Ma, 2013).

Overall, the distribution of objects in our sample does not preferentially lie above or below the local relation. NLS1s in our sample span a mass range from 6.3 to 7.1 in $\log_{10}(M_{\rm BH})$ and, on average, fall on the local relation with comparable scatter to the overall sample. Overall, our sample expands on the non-local relation by occupying the lower to intermediate SMBH mass range with a scatter comparable to the local relation.

2.4.2 Evolution in the $M_{\rm BH} - \sigma_*$ Relation

In Figure 2.8 we plot $\Delta \log_{10}(M_{\rm BH})$ as a function of redshift. Following Woo et al. (2006, 2008), we investigate the possibility of evolution in the $M_{\rm BH} - \sigma_*$ relation, by performing linear regression of $\Delta \log_{10}(M_{\rm BH})$ with respect to to the local $M_{\rm BH} - \sigma_*$ relation as a function of redshift following the linear model used by Park et al. (2015), given by

$$\Delta \log_{10}(M_{\rm BH}) = \gamma \log_{10}(z+1). \tag{2.6}$$

Since we have defined $\Delta \log_{10}(M_{\rm BH})$ with respect to the local relation, we exclude an intercept as free parameter. We also avoid binning BH masses by redshift to avoid introducing any biases due to the fact that our objects are not at discrete redshift intervals, unlike the samples of Woo et al. (2006, 2008), which were - by design - selected at discrete intervals of $z = 0.36$ and $z = 0.57$, respectively. We perform maximum-likelihood regression and estimate uncertainties using MCMC finding the value in the best-fit slope to be $\gamma = 2.16 \pm 0.62$ with a scatter of $\epsilon_0 = 0.43 \pm 0.03$, which implies a 3.5σ confidence for a non-zero positive slope.

Previous analysis by Woo et al. (2008) compared $z = 0.36$ and $z = 0.57$ Seyfert 1

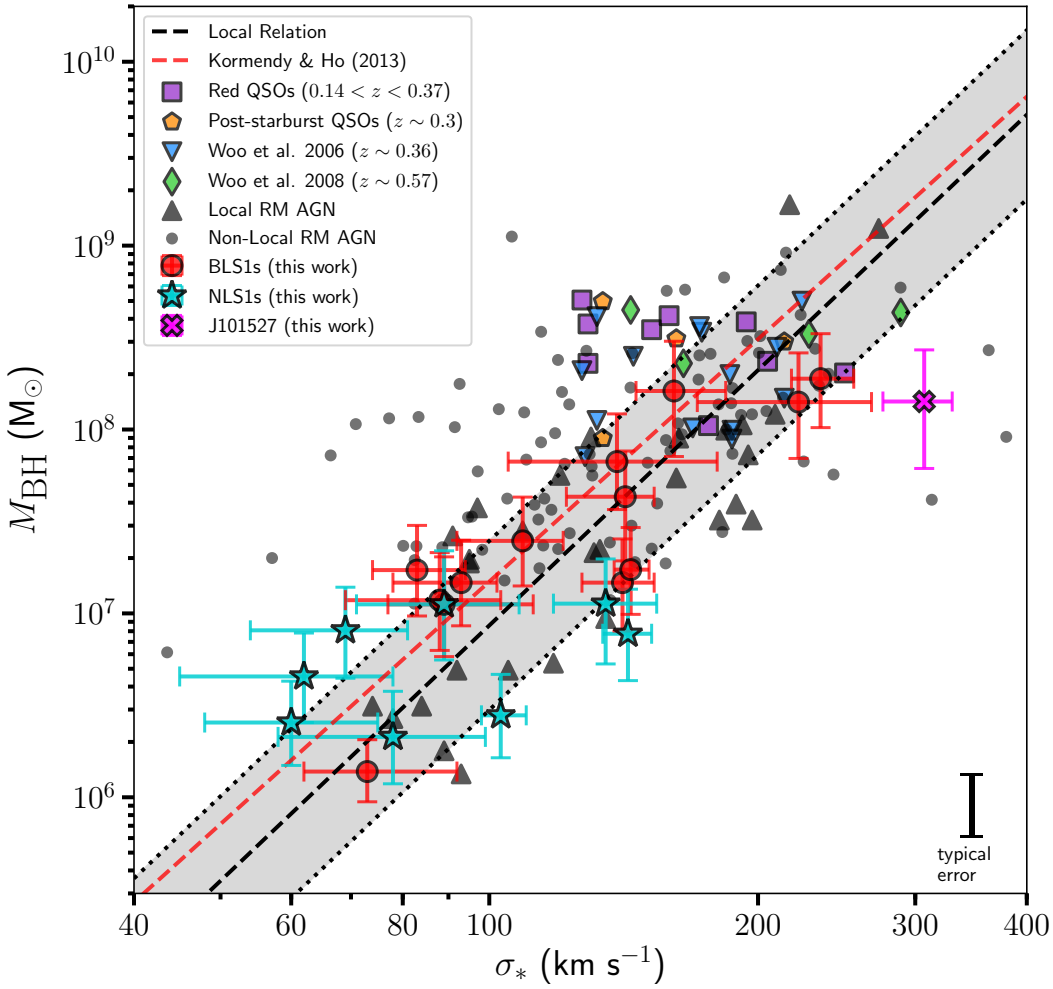

Figure 2.7: The $M_{\rm BH} - \sigma_*$ relation for our sample, including objects from selected non-local studies. The black dashed line indicates the local relation we derived using BH masses of local AGNs from Bennert et al. (2011a), local inactive galaxies from McConnell & Ma (2013), and local reverberation-mapped AGNs from Woo et al. (2015), using the most recent BH mass calibration from Woo et al. (2015) (Equation 2.5). The black dotted lines and shaded area represent the local scatter. The red dashed line represents the relation from Kormendy & Ho (2013), based on BH masses of local inactive galaxies measured using stellar and gas kinematics. Additionally, we include local reverberation-mapped objects from Woo et al. (2015) and non-local reverberation-mapped objects from Shen et al. (2015) for comparison.

objects (Woo et al., 2006, 2008) found a slope of $\gamma = 3.1 \pm 1.5$, however, they compared their sample to the local inactive relation fit available at the time by Tremaine et al. (2002), which is a shallower local relation (a slope of $\beta = 4.02 \pm 0.44$), and enhances the apparent offset in $M_{\rm BH}$ by 0.43 dex and 0.63 dex at $z = 0.36$ and $z = 0.57$, respectively. If we perform the same analysis of the non-local objects from Woo et al. (2008) with our revised local relation we find a slope of $\gamma = 1.93 \pm 0.73$ or 2.6σ confidence for a non-zero slope and an offset in $M_{\rm BH}$ of only 0.26 dex and 0.38 dex at $z = 0.36$ and $z = 0.57$, respectively, which is less than the ~ 0.4 dex scatter of these data at these redshifts. Including dust-reddened 2MASS QSOs from Canalizo et al. (2012), and post-starburst QSOs from Hiner et al. (2012) enhances the slope further to $\gamma = 2.43 \pm 0.68$ (3.6σ confidence) due to these objects being preferentially above the relation by $\sim$0.5 dex in $\Delta \log_{10}(M_{\rm BH})$ at $z \sim 0.3$. With the inclusion of our objects, the significance of a non-zero slope decreases slightly to 3.5σ confidence. If we were to omit higher-luminosity QSOs and consider only Seyfert 1 objects the slope decreases to $\gamma = 1.69 \pm 0.65$ (2.6σ confidence).

From Figure 2.8, there is ample reason to be skeptical of any underlying trend in $\Delta \log_{10}(M_{\rm BH})$ as a function of z, as it is clear that there remains considerable scatter in $\Delta \log_{10}(M_{\rm BH})$. We can quantify the strength of a linear correlation for our data in the context of the scatter by computing the nonparametric Spearman's correlation coefficient, assuming there exists some monotonically increasing relationship in $\Delta \log_{10}(M_{\rm BH})$ as a function of z. We calculate the Spearman's coefficient and its uncertainty using Monte Carlo methods. Spearman's correlation coefficient of the non-local sample, including our objects, is $r_s = 0.23 \pm 0.04$, indicating a very weak to weak positive correlation. The weakness

of the correlation is due primarily to the consistent scatter of $\sim$0.4 dex across the entire sampled redshift range. In other words, the scatter we observe locally and at low redshifts is comparable to the scatter we observe at the highest redshifts, which implies there is - at best - a weak dependence of $\Delta \log_{10}(M_{\rm BH})$ on redshift. If we instead fit a constant model to $\Delta \log_{10}(M_{\rm BH})$ to all non-local objects, we find that the constant offset from the local relation is $C = 0.19 \pm 0.08$ with a scatter of $\epsilon_0 = 0.40 \pm 0.07$. Most importantly, the residual scatter is nearly identical regardless of the model chosen, due solely to the large amount of scatter at all redshifts. Additionally, because the intercept of the linear fit to $\Delta \log_{10}(M_{\rm BH})$ is held constant to zero (because we are comparing it to the local relation at $z = 0$), any datum at high redshift can have considerable influence on the slope of the linear fit, especially for our small sample. Considering the level of scatter across the sampled redshift range, the weak correlation of $\Delta \log_{10}(M_{\rm BH})$ with respect to z, and the fact that the majority of these data reside well within the local scatter (see Figure 2.8), we conclude that any evolution in the $M_{\rm BH} - \sigma*$ relation in the past 6 Gyr is very weak at best.

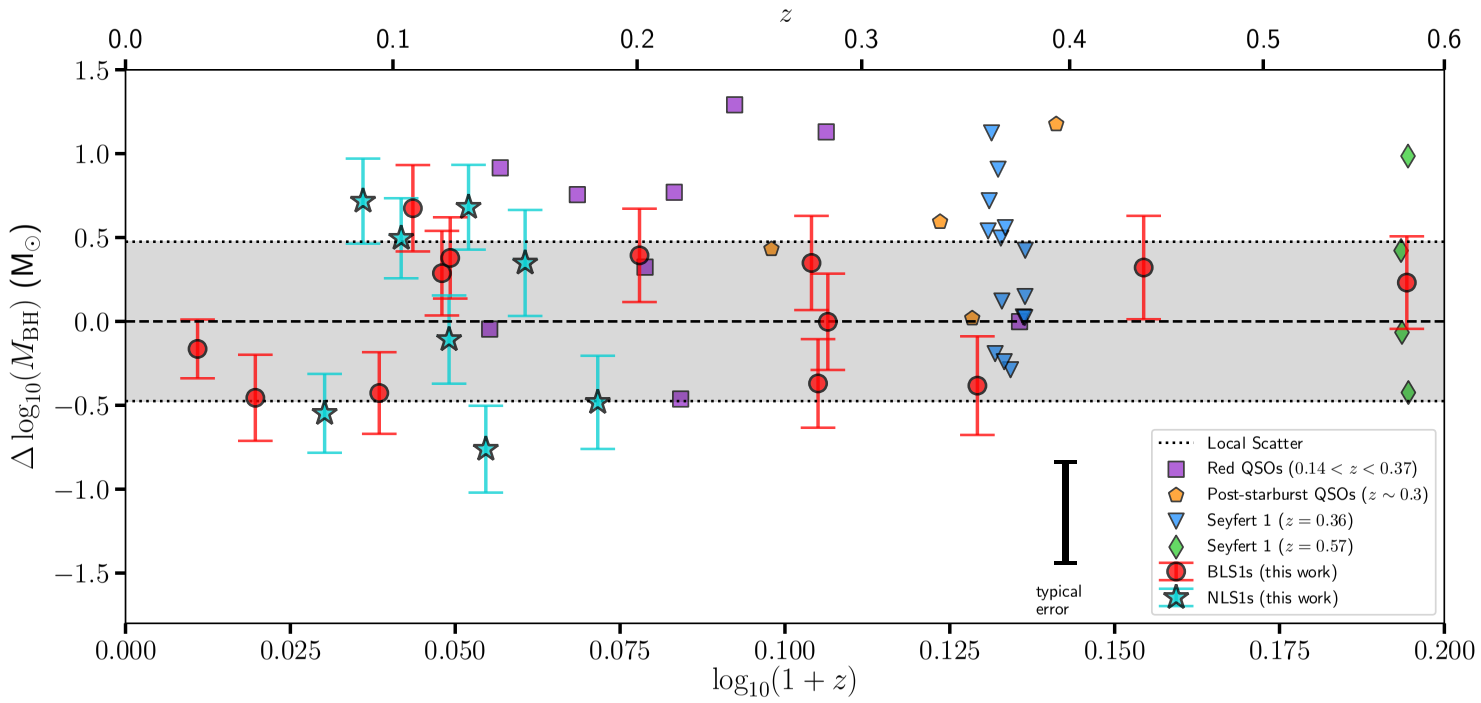

Figure 2.8: $\Delta \log_{10}(M_{\rm BH})$ as a function of redshift with respect to the local $M_{\rm BH} - \sigma*$ relation to investigate any offset. The gray shaded area corresponds to the scatter in the local relation. The majority of non-local objects reside well within the local scatter. While the slope of $\gamma = 2.16 \pm 0.62$ can be fit, implying a significant offset, the correlation is weak due to the consistent scatter across all sampled redshifts, indicating that the offset is driven by only a small number of objects at the high-redshift regime. Alternatively, the average offset of non-local objects, found by fitting a constant, is $C = 0.19 \pm 0.08$, and results in an identical residual scatter as a linear fit. While the offset remains non-zero, this does not necessarily indicate evolution, as we see greater offset in lower-redshift objects on average than higher-redshift objects, indicating that we may still be sampling the higher-mass BH regime due to selection effects.

Table 2.4: Measurements of $M_{\rm BH}$ and σ_*. Column 1: object. Column 2: redshift as measured from stellar absorption features, repeated here for reference. Column 3: intrinsic extinction as measured from the Balmer decrement. Column 4: Hβ FWHM. Column 5: base 10 logarithm of the AGN luminosity at 5100 Å, as measured from GALFIT surface brightness decomposition. Column 6: inclination-corrected stellar velocity dispersion. Column 7: base 10 logarithm of calculated BH mass from Equation

Object	z	$E(B-V)$	FWHM$_{\rm H\beta}$ (km s^{-1})	$\log_{10}(\lambda L_{5100})$ (erg s^{-1})	σ_* (km s^{-1})	$\log_{10}(M_{\rm BH})$ ($M_\odot$)
J000338.94+160220.6	0.11681	0.010	3253^{+233}_{-233}	$43.07^{+0.11}_{-0.10}$	109^{+12}_{-17}	$7.39^{+0.32}_{-0.19}$
J001340.21+152312.0	0.12006		2854^{+205}_{-206}	$42.85^{+0.11}_{-0.10}$	93^{+9}_{-15}	$7.17^{+0.30}_{-0.18}$
J015516.17−094555.9	0.56425	0.019	4350^{+366}_{-333}	$43.40^{+0.11}_{-0.10}$	139^{+41}_{-34}	$7.83^{+0.36}_{-0.20}$
J040210.90−054630.3	0.27065	0.051	2308^{+232}_{-204}	$42.98^{+0.11}_{-0.14}$	89^{+23}_{-12}	$7.05^{+0.35}_{-0.21}$
J073505.66+423545.6	0.08646		2019^{+148}_{-155}	$42.93^{+0.11}_{-0.13}$	69^{+12}_{-15}	$6.91^{+0.31}_{-0.20}$
J092438.88+560746.8	0.02548		2650^{+209}_{-199}	$41.05^{+0.11}_{-0.08}$	65^{+19}_{-11}	$6.14^{+0.21}_{-0.14}$
J093829.38+034826.6	0.11961		1186^{+118}_{-102}	$42.71^{+0.11}_{-0.11}$	78^{+21}_{-20}	$6.33^{+0.33}_{-0.19}$
J095819.87+022903.5	0.34643		4845^{+361}_{-360}	$43.83^{+0.11}_{-0.15}$	222^{+46}_{-51}	$8.15^{+0.37}_{-0.22}$
J100234.85+024253.1	0.19659	0.115	2607^{+187}_{-186}	$42.82^{+0.18}_{-0.15}$	88^{+15}_{-19}	$7.07^{+0.35}_{-0.20}$
J101527.25+625911.5	0.35064		4379^{+369}_{-324}	$44.01^{+0.11}_{-0.21}$	307^{+23}_{-31}	$8.15^{+0.39}_{-0.25}$
J113657.68+411318.5	0.07200		1476^{+109}_{-104}	$42.57^{+0.11}_{-0.11}$	103^{+7}_{-5}	$6.45^{+0.29}_{-0.18}$
J120814.35+641047.5	0.10555	0.140	2400^{+169}_{-170}	$43.26^{+0.11}_{-0.10}$	83^{+11}_{-9}	$7.24^{+0.33}_{-0.19}$
J123228.08+141558.7	0.42692		4704^{+333}_{-334}	$44.00^{+0.11}_{-0.20}$	161^{+23}_{-15}	$8.21^{+0.37}_{-0.24}$
J123349.92+634957.2	0.13407		1767^{+133}_{-143}	$43.11^{+0.11}_{-0.10}$	143^{+9}_{-9}	$6.89^{+0.32}_{-0.19}$
J123455.90+153356.2	0.04637		2742^{+211}_{-206}	$42.92^{+0.11}_{-0.13}$	141^{+12}_{-14}	$7.17^{+0.32}_{-0.20}$
J132504.63+542942.3	0.14974	0.039	1929^{+248}_{-198}	$43.27^{+0.11}_{-0.13}$	89^{+19}_{-18}	$7.05^{+0.41}_{-0.22}$
J132943.60+315336.7	0.09265	0.021	3122^{+221}_{-224}	$42.84^{+0.11}_{-0.11}$	144^{+7}_{-6}	$7.24^{+0.30}_{-0.19}$
J141234.67−003500.0	0.12724		1475^{+109}_{-125}	$42.97^{+0.11}_{-0.10}$	62^{+16}_{-17}	$6.66^{+0.31}_{-0.19}$
J142543.20+344952.9	0.17927	0.144	2004^{+145}_{-150}	$43.21^{+0.11}_{-0.20}$	135^{+19}_{-17}	$7.05^{+0.33}_{-0.23}$
J145640.99+524727.2	0.27792	0.166	3608^{+263}_{-256}	$43.35^{+0.11}_{-0.22}$	142^{+11}_{-20}	$7.63^{+0.34}_{-0.24}$
J160044.99+505213.6	0.10104		1363^{+102}_{-101}	$42.63^{+0.11}_{-0.10}$	60^{+15}_{-12}	$6.41^{+0.30}_{-0.18}$
J171806.84+593313.3	0.27356	0.031	8179^{+600}_{-598}	$43.22^{+0.11}_{-0.12}$	235^{+21}_{-17}	$8.28^{+0.33}_{-0.20}$

2.5 Systematics

The following sections outline possible systematic uncertainties and selection effects that may affect our measurements.

2.5.1 Hβ Width Measurements

Previous studies (Woo et al., 2006, 2008) use the second moment of the Hβ emission line, showing that line measurements from single-epoch spectra are consistent with those of reverberation studies; however, it is often easier to measure FWHM in lower-S/N spectra. One caveat of adopting a FWHM parameterization for the Hβ width is the fact that the relationship between FWHM and σ is not necessarily FWHM/$\sigma = 2.355$, and previous studies have attempted to account for the discrepancy (Park et al., 2012). Woo et al. (2015) derived a virial factor that takes into account the systematic uncertainty added to mass estimates derived from calibrations from reverberation studies, given by $f = 0.05 \pm 0.12$, which we adopt here. We found that asymmetries in the broad Hβ line profile are due to underlying stellar absorption, and that when broad Hβ and the stellar continuum are fit simultaneously, a single Gaussian component fully accounts for any line asymmetries. We find that our single-component Gaussian measurements are consistent with measurements using multiple Gaussian components to account for line asymmetries. We also find that the uncertainties in our estimates of the FWHM decrease by a factor of 2.3 when fit simultaneously with the stellar continuum and Fe II emission. Uncertainty due to variability of the FWHM of Hβ with respect to rms line widths from reverberation studies are estimated to be 7% (Woo et al., 2007), which we add to our random uncertainties in quadrature. On average, the total uncertainty in our measurements for broad Hβ FWHM is $\sim$8%, corresponding to a 0.06 dex uncertainty in $M_{\rm BH}$. One object in our sample, J015516, was observed independently by Woo et al. (2008) to have $\sigma_{\rm H\beta} = 2103$ km s^{-1}, which is consistent with our measurement of FWHM$_{\rm H\beta} = 4350$ km s^{-1} if we assume FWHM/$\sigma \sim 2$. We conclude that our estimates

for Hβ width measured from the FWHM of the line profile are not a significant source of systematic uncertainty, and do not significantly affect estimates of $M_{\rm BH}$.

2.5.2 λL_{5100} Measurements

Residuals of surface brightness photometry performed on *HST* imaging show there is very good agreement of the empirically constructed PSF and the central surface brightness of the AGN for each object. Large residuals in surface brightness profiles are at most $\Delta\mu = 0.3$ mag arcsec^{-2} and appear to result from intrinsic properties of each object, such as the presence of dust lanes and spiral arms. On average, the uncertainty due to PSF mismatch is $\sim$0.1 mag. We do not suspect PSF mismatch to be a significant source of error in our measurements for the AGN luminosity. For comparison, Park et al. (2015) independently fit J073505 from *HST*/NICMOS/F110W imaging and obtained a $\lambda L_{5100} = 1.02$ (10^{44} erg s^{-1}), while we obtained $\lambda L_{5100} = 1.01$ (10^{44} erg s^{-1}) with *HST*/ACS-WFC/F775W imaging.

The simple power-law parameterization used to model the AGN continuum from the full spectrum (LRIS-B + LRIS-R) also contributes an uncertainty of $\sim$0.1 mag. Uncertainties in various corrections, e.g. extinction, AGN fraction, k-correction, and passive evolution, we conservatively estimate at $\sim$0.1 mag.

To account for uncertainty due to variability in our measured luminosities, we adopt an additional 15% uncertainty based on the median uncertainty from reverberation-mapped luminosities from Bentz et al. (2013).

The overall uncertainty in our estimates for λL_{5100} is $\sim$30% on average, corresponding to a 0.08 dex uncertainty in $M_{\rm BH}$, consistent with the uncertainties estimated by Treu et al. (2007). Given that $M_{\rm BH} \propto \lambda L_{5100}^{0.533}$, we do not expect our measurements for

λL_{5100} to contribute a significant offset in our estimates for $M_{\rm BH}$.

Extinction, if left unaccounted for, can also lead to an underestimate of λL_{5100}, and therefore an underestimate of BH mass. We correct for Galactic extinction, as well as intrinsic extinction estimated from measurements of narrow Balmer line ratios. We do not use broad-line emission ratios to correct for extinction within the BLR. However, given the low dependence of λL_{5100} on BH mass, we do not suspect extinction from the BLR to significantly affect our results except in extreme cases. For instance, not accounting for a reddening value of $E(B-V) = 0.1$ corresponds to a 0.06 dex underestimation of BH mass.

2.5.3 BH Mass Calibration

The derivation of Equation 2.3.7 used to calculate single-epoch BH mass is empirically calibrated using local ($z < 0.3$) reverberation-mapped AGNs to obtain the $R_{\rm BLR} - \lambda L_{5100}$ relation. The behavior of the $R_{\rm BLR} - \lambda L_{5100}$ relation at $z > 0.3$ however is still unknown due to a lack of reverberation-mapping studies at higher redshifts, which may be problematic for the high-z objects in our sample. Furthermore, it is possible that the the behavior of the $R_{\rm BLR} - \lambda L_{5100}$ relation may be dependent on accretion rate. Recent reverberation-mapping measurements performed by Du et al. (2016) of super-Eddington accreting massive BHs in AGNs found that $R_{\rm BLR}$ scales inversely with accretion rate, i.e. higher accretion rates result in smaller $R_{\rm BLR}$. If not taken into consideration, this dependence could systematically cause us to overestimate the BH mass of NLS1 objects in our sample per given λL_{5100}, which have higher accretion rates (12% on average) than the BLS1s in our sample (4% on average). However, since the NLS1s in our sample have gener-

ally lower accretion rates than those studied by Du et al. (2016), we expect the contribution of accretion rate on the calculation of BH mass for objects in our sample to be negligible.

2.5.4 σ_* Measurements

2.5.4.1 Template Mismatch

Template fitting performed to measure the LOSVD of the host galaxy is typically performed using a set of template stars observed on the same night as the science targets; however, if the stellar population of the host galaxy is not known, it can result in template mismatch which can bias measurements of σ_*. To minimize the effects of template mismatch, we instead use a large number ($N = 636$) of template stars of various types from the Indo-US Library of Coudé Feed Stellar Spectra (Valdes et al., 2004). The random uncertainty is estimated via Monte Carlo methods, which sample all possible templates until a stable LOSVD solution is met. Given the large number of stellar templates used in the fit, it is unlikely template mismatch contributes to significant uncertainties in our measurements in σ_*.

2.5.4.2 Fitting Region

The choice of fitting region used to measure σ_* can also potentially contribute to significant bias. Greene & Ho (2006b) investigated the viability and systematics of measuring σ_* in the Ca H+K, Mg Ib, and Ca T regions and found that while the Ca T region is the least susceptible to template mismatch and Fe II contamination, it is the region most affected by AGN continuum dilution, which acts to bias measurements of σ_* to higher val-

ues (decrease line EW). On the other hand, the Ca H+K region is the least affected by continuum dilution, but the most susceptible to template mismatch. Additionally, both the Ca T and Ca H+K regions can be biased by their stellar populations, most notably by the presence of A stars which significantly broaden hydrogen lines. Greene & Ho (2006b) concluded that Mg Ib is the most practical region to measure σ_* at redshifts $0.05 < z < 0.76$ under the conditions that the amount of AGN continuum dilution is $\leq 85\%$ and Eddington ratios are ≤ 0.5. The average AGN dilution in our sample is 41% and does not exceed 82%, as measured by taking the AGN-to-total flux ratio from surface brightness decomposition of *HST* imaging. Figure 2.9 shows that our objects have Eddington ratios well below the 50% threshold for accurate measurements of σ_*, therefore we do not suspect continuum dilution to contribute significant bias. While measurements of σ_* in the Mg Ib region can be significantly biased by the presence of Fe II emission, this effect can be mitigated by including Fe II templates in our fitting process, as discussed below.

2.5.4.3 Fe II Contamination

Broad and narrow Fe II emission is present in all objects in our sample to some extent and can have significant effects. To account for this, we include 20 narrow and 91 broad Fe II templates to be fit simultaneously with stellar templates. We avoid subtracting off Fe II emission prior to stellar template fitting due to the presence of strong narrow emission in some objects, which can mimic variations in the stellar continuum and make determination of the relative contribution of narrow Fe II impossible. Narrow emission, if unaccounted for, can bias measurements of σ_* to larger values by as much 90%, corresponding

to a $0.2-0.3$ dex offset in $\log_{10}(\sigma_*)$ on the $M_{\rm BH}-\sigma_*$ relation. We show the offset of measured values of σ_* caused by the presence of Fe II in the fitting region in Figure 2.10. We also show that NLS1s in our sample are the most affected by Fe II contamination, particularly due to the presence of strong narrow Fe II contamination in these objects. There is a well known anti-correlation between the strength of Fe II and other properties of NLS1 galaxies like BH mass and Eddington ratio (e.g., Grupe & Mathur (2004), Komossa (2008b), Xu et al. (2012)), and we observe the same trend in our sample. One such object, J123349, remains offset in $\log_{10}(\sigma_*)$ by $+0.16$ dex, which could be due to Fe II template mismatch. This highlights the importance of correcting for Fe II emission, especially in samples of high luminosity and NLS1 (high Eddington ratio) where narrow Fe II contamination is most common, as they can significantly bias σ_* measurements.

2.5.4.4 Morphology

The observed scatter in our sample could be attributed to properties such as host galaxy morphology, which can have a significant influence on the measurement of σ_*. Morphological biases in σ_* may arise if hosts are not elliptical or do not exhibit "classical" bulges. For instance, Graham et al. (2011) showed that barred hosts tend to fall $\sim$0.5 dex below the $M_{\rm BH}-\sigma_*$ relation compared to non-barred hosts. From our sample, five objects (J095819, J100234, J132943, J141234, and J145640) show clear bar morphologies within their disks; however, we see no such offset of barred hosts compared to non-barred hosts on the $M_{\rm BH}-\sigma_*$ relation within our sample.

Another more obvious source of potential offset in σ_* could be the result of a bulge

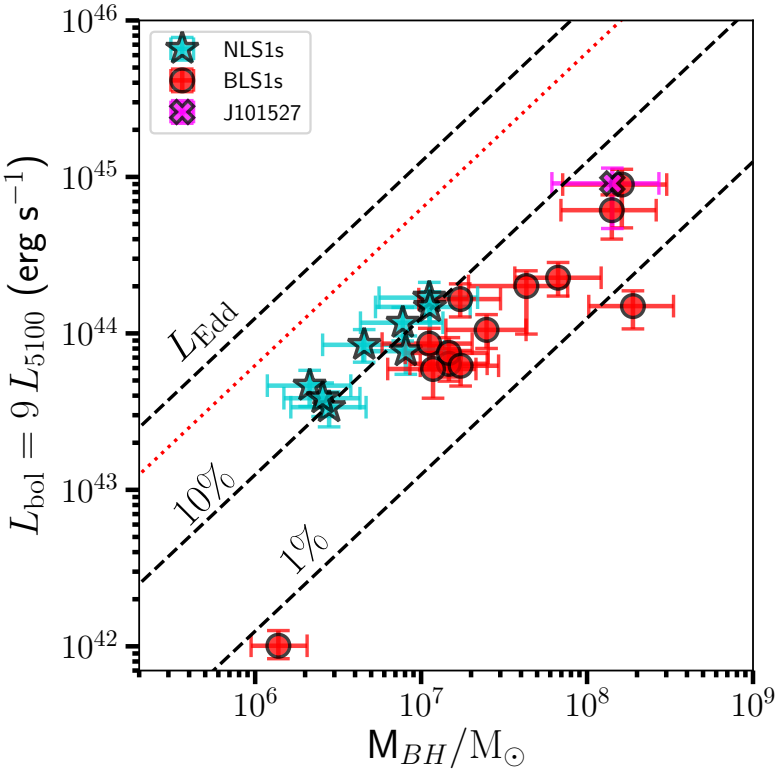

Figure 2.9: Bolometric luminosity vs. BH mass. Dashed lines correspond to Eddington ratios. The dotted red line indicates 50% of the Eddington limit, beyond which it is ill-advised to measure σ_* due to significant AGN continuum dilution. All NLS1 objects in our sample have the highest Eddington ratios, consistent with previous studies which indicate that NLS1s have high accretion rates.

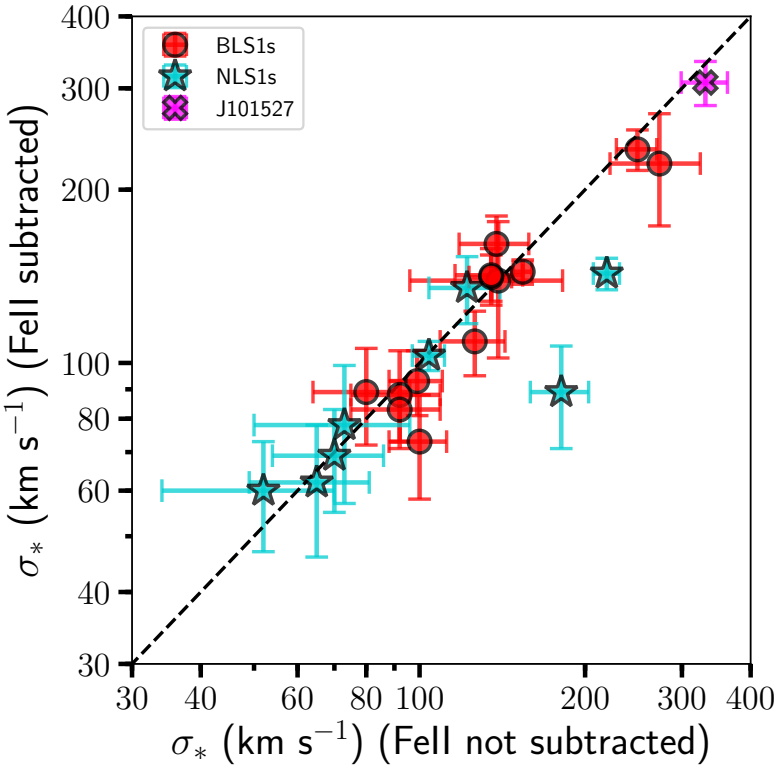

Figure 2.10: Effect of Fe II emission on measurements of σ_*. For the majority of our sample, the effect is negligible. However, Fe II contamination can significantly affect σ_* measurements if strong narrow Fe II is present, as this emission can mimic stellar absorption features. Narrow Fe II emission seems to be strongest in NLS1 objects, possibly due to their high accretion rates.

that is no longer in dynamical equilibrium, such as in the case of a merger event. Previous studies have shown that mergers in progress have been found to have increased scatter on the $M_{\rm BH} - \sigma_*$ relation and tend to have undermassive BHs relative to their hosts, corresponding to a larger velocity dispersion than inferred from the local relation (Kormendy et al., 2011; Kormendy & Bender, 2013). More recently, high spatial resolution near-IR integral field spectroscopy performed by Medling et al. (2015) of nuclear disks of late-stage, gas-rich mergers have shown that their BHs are overmassive by a significant amount, suggesting that they grow more quickly than their hosts. One object in our sample, J000338, appears to be in the early stages of a merger in *HST* imaging and falls above the local relation by a factor of 0.31 dex in BH mass but well within 1σ scatter of the local relation. This is most consistent with time-resolved N-body simulations used to investigate the evolution of σ_* during mergers performed by Stickley & Canalizo (2014), which found that σ_* in the bulge component in the early stages of the interaction does not significantly deviate from the value of σ_* measured before the interaction. They also found that, while the value of σ_* oscillates during the merger process, it is unlikely that the deviation from the equilibrium value will be large. Considering the large separation distance between the two progenitors (~ 11 kpc, not considering any projection effects), and that the measured σ_* is within 15% of the value of σ_* implied by the local relation, we conclude that the σ_* measured for J000338 is consistent for a dynamically relaxed bulge and do not omit it from our analyses.

Another object, J101527, appears to show evidence of interaction from *HST* imaging, and surface brightness decomposition of J101527 also reveals a double nucleus, consisting of an AGN and another low-surface-brightness object. Kim et al. (2017) classified J101527

as a candidate recoiling SMBH resulting from a merger, and the host galaxy is likely a bulge-dominated elliptical in the late stages of a merger (see Kim et al. (2017) for a detailed analysis of J101527). Kim et al. estimated the stellar velocity dispersion from Keck/LRIS spectra using the [S II]λ6716 width following Komossa & Xu (2007), obtaining a value of $\sigma_{[\mathrm{S\ II}]} = 190 \pm 20$ km s^{-1}, which places J101527 very close to our local $M_{\mathrm{BH}} - \sigma_*$ relation. We measure a nearly identical value using the [O III]λ5007 width of $\sigma_{[\mathrm{O\ III}]} = 197 \pm 3$ km s^{-1} from our Keck/LRIS spectra. Measuring σ_* directly from the stellar continuum, we find $\sigma_* = 307 \pm 27$ km s^{-1}, a 56% difference from what is measured from the [O III] width. The large offset in σ_* results in a BH mass that is undermassive by $\sim$1.0 dex, making it the largest outlier in our sample. However, this offset may indicate that the stellar component is not yet dynamically relaxed. Numerical simulations indicate that measurements of σ_* are enhanced for merging nuclei as separation distance decreases (Stickley & Canalizo, 2014). The clear morphological peculiarities of this object, as well as the large uncertainty in measured σ_* values, warrant the omission of J101527 from analyses when considering evolution in the $M_{\mathrm{BH}} - \sigma_*$ relation. We however include its measurements in Table 2.4 as well as flag this object as a merger in our diagrams.

To further investigate possible biases due to morphology, we consider the location of bulges of our sample on the fundamental plane relation (FP; Djorgovski & Davis (1987)). Surface brightness measurements are obtained using the `sersic2` option in GALFIT and appropriate corrections for extinction, k-correction, surface brightness dimming, filter transformations, and passive evolution are applied. The FP relation for our sample is shown in Figure 2.11. Following Canalizo et al. (2012), we compare our objects to the SDSS-r or-

thogonal fit to ∼50,000 SDSS DR6 of early-type galaxies at $0.0 < z < 0.35$ from Hyde & Bernardi (2009), given by the solid line in Figure 2.11. We find that the majority of our sample is in good agreement with the FP relation. One object, J123349, falls completely outside the SDSS scatter. This object is classified as an NLS1 and exhibits a high fraction of Fe II contamination in its spectra, which is likely biasing the measurement of σ_* to higher values despite our best efforts to account for it using Fe II templates. The measured stellar velocity dispersion of J123349 also places this object high on the Faber-Jackson relation (Faber & Jackson, 1976) relative to its bulge luminosity, indicating that Fe II contamination is likely contributing to its offset on the FP relation.

It is worth noting that the NLS1s in our sample have consistently smaller bulges than the BLS1s. Some previous studies have suggested that NLS1s fall below the $M_{\rm BH} - \sigma_*$ relation (Mathur et al., 2001; Grupe & Mathur, 2004). These were based on $\sigma_{[\rm O\ III]}$ as a proxy for σ_*; however, they did not remove blue outliers, which are completely dominated by outflows (Komossa & Xu, 2007). After removing blue outliers, the remaining NLS1 galaxies scatter around the relation like BLS1 galaxies. In a study of 93 local SDSS NLS1 galaxies, Woo et al. (2015) found similar agreement with the local relation when stellar velocity dispersions are measured directly from stellar absorption features.

The use of *HST* imaging of NLS1s in our sample allows us to further investigate the morphologies of these objects in greater detail. The location of NLS1s on the FP relation in Figure 2.11 would imply that they do indeed have smaller bulges, as we would expect from their location on the $M_{\rm BH} - \sigma_*$ relation. This also presents a strong case for narrow Hβ emission being indicative of a lower-mass BH, and not due to any peculiar geometry of

the BLR (Decarli et al., 2008, 2011). However, one caveat is that the NLS1 sample used by Decarli et al. (2008) (originating from Grupe et al. (1999)) was specific in selecting NLS1s with strong Fe II, whereas our sample contains only two (of eight) NLS1s with strong Fe II. Despite this, it is worth noting that aside from measurements of σ_* (which are directly influenced by Fe II contamination), the NLS1s in our sample appear to show similar physical characteristics (lower $M_{\rm BH}$, higher $L/L_{\rm Edd}$, and $L_{\rm Bulge,V}$) that do not appear to be a function of Fe II strength. However, a larger comparison sample of NLS1 objects of varying Fe II strength is needed to make any conclusive statements on how Fe II strength affects other properties of NLS1s.

As a final test for any morphological bias, we investigate where our sample falls on the $M_{\rm BH} - L_{\rm bulge}$ relation. We transform bulge luminosities from each respective *HST* filter to Johnson-V luminosities, making all the necessary corrections, to compare our sample to the $M_{\rm BH} - L_{\rm bulge}$ relation from McConnell & Ma (2013). We plot the $M_{\rm BH} - L_{\rm bulge}$ relation of our sample in Figure 2.12 alongside points and best-fit from McConnell & Ma, with the 68%, 95% and 99% confidence intervals of the scatter. We find good agreement with the relation from McConnell & Ma, with our sample having a comparable scatter. One of our objects on the $M_{\rm BH} - L_{\rm bulge}$ relation, J092438, is a clear outlier and we discuss possible reasons for its apparent undermassive BH relative to its host bulge luminosity in the Appendix.

2.5.4.5 Selection Effects

In addition to measurement uncertainties, we investigate any possible uncertainties and biases that may result from selection criteria. The selection criteria used for our sample

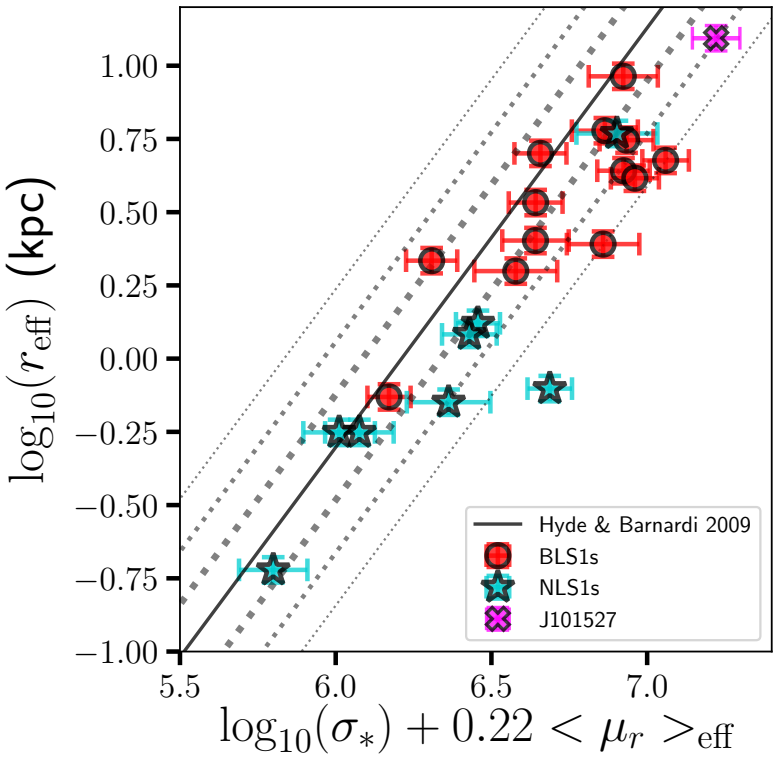

Figure 2.11: Fundamental plane relation for objects in our sample with magnitudes converted to SDSS-r band. Dashed lines enclose 68%, 95%, and 99% of SDSS early-type galaxies from the orthogonal fit to ∼50,000 SDSS DR6 of early-type galaxies in SDSS-r band at $0.0 < z < 0.35$ from Hyde & Bernardi (2009).

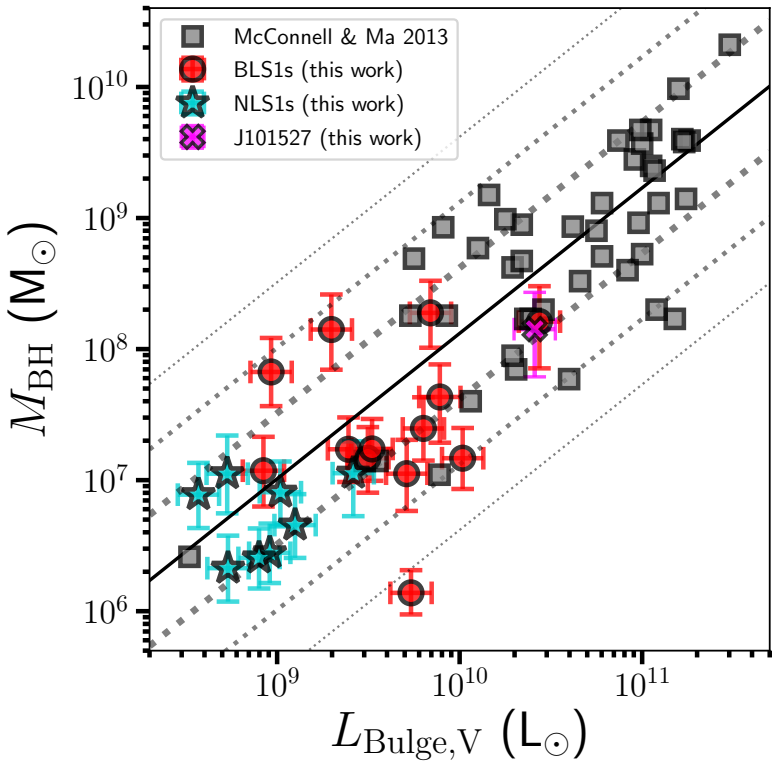

Figure 2.12: The $M_{\rm BH} - L_{\rm bulge}$ relation for objects in our sample compared to local inactive objects from McConnell & Ma (2013). Dashed lines represent the the 68%, 95% and 99% confidence intervals of the scatter.

required a broad Hβ FWHM within the range 500 km s^{-1} $\leq$ FWHM$_{\mathrm{H}\beta}$ $\leq$ 2000 km s^{-1} to select candidate NLS1 objects, and visible stellar absorption features (typically Ca H+K equivalent width EW$_{\mathrm{CaH+K}} > 0.5$ Å) to ensure that σ_* could be accurately measured.

In general, the presence of broad lines may select against host galaxies with higher (edge-on) inclinations, which have systematically higher σ_* values relative to host galaxies at lower inclinations due to the presence of contaminating disk stars along the line of sight (Bellovary et al., 2014). We correct σ_* for objects in our sample which contain disks to face-on σ_* values to account for any σ_* values that may be inflated due to the presence of a disk and thus give the appearance of an undermassive BH on the $M_{\mathrm{BH}} - \sigma_*$ relation (see Section 2.3.1).

The broad Hβ line width requirement, by design, biases our sample toward lower BH masses. Our original intention was to detect lower-mass BHs at high redshifts using NLS1 galaxies. Unfortunately, our selection in FWHM$_{\mathrm{H}\beta}$ was not rigorously met due to the nature of the SDSS DR7 line-fitting algorithm, and no NLS1 objects were found at $z > 0.2$. On the other hand, our sample covers a broad range in mass: two orders of magnitude in the range $6.3 < \log_{10}(M_{\mathrm{BH}}) < 8.3$. Finally, the requirement for visible absorption lines to accurately measure σ_* in the Mg Ib region also preferentially selects objects with AGN luminosities lower than or comparable to the host galaxy, therefore requiring lower average AGN luminosities and lower BH masses, assuming the AGN luminosity is due entirely to BH accretion and a function of BH mass. Indeed, the average AGN-to-total light fraction of our sample (as measured from *HST* imaging) is $41 \pm 12\%$ with no objects exceeding 82%, which ensures we should be able to accurately measure σ_* and should not be significantly

biased toward higher dispersions due to AGN dilution of stellar absorption features.

However, by selecting objects with visible stellar absorption features with a minimum EW (line strength), we may implicitly introduce some maximum AGN luminosity threshold relative to the host galaxy per given redshift. A requirement for visible stellar absorption features implies that stellar light from the host galaxy is not significantly diluted by the light from the AGN, which implies there is some maximum AGN-to-total light ratio beyond which σ_* cannot be measured, and therefore a maximum luminosity threshold for the AGN. Additionally, the S/N requirements for visible absorption features in higher-redshift objects would require more massive, and therefore more luminous host galaxies, of which there are fewer due to the steep drop in the luminosity function of galaxies. Therefore selection by absorption line visibility at higher redshifts could still be biased to overmassive BHs. We do see that the highest-redshift BHs in our sample tend to be overmassive, which may be the result of our implicitly imposed AGN luminosity threshold.

Lauer et al. (2007) explained that intrinsic scatter in the $M_{\rm BH}-$bulge scaling relations implies that, for a given $L_{\rm bulge}$ or σ_*, there exists a range of BH masses. However, samples selected by some given AGN luminosity threshold (as is typically done for high-redshift samples) results in a distribution of $L_{\rm host}$ and σ_* per $M_{\rm BH}$, assuming that AGN luminosity is determined solely by BH mass. This, combined with the steep drop in the luminosity function of galaxies, preferentially selects overmassive BHs relative to their hosts, which can thus produce a false signature of evolution in high-redshift studies. Woo et al. (2006, 2008) selected objects with a minimum Hβ EW of 5 Å, but using Monte Carlo simulations to model a sharp selection in luminosity, Treu et al. (2007) found that this bias is

negligible for the $M_{\rm BH} - \sigma_*$ relation unless the scatter at high redshift increases considerably.

In addition to the Lauer et al. (2007) bias, Shen & Kelly (2010) suggest that luminosity-threshold samples tend to be biased toward high SE virial BH masses by as much as 0.2 to 0.3 dex, due to the uncorrelated variations between continuum luminosity and line widths in reverberation-mapping studies, from which we obtain BH virial mass estimates. Together, it is possible the Lauer et al. (2007) and Shen & Kelly (2010) biases can account for the offset in BH mass at high redshift, with biases becoming worse as a function of z for higher-luminosity thresholds.

We plot $\log_{10}(\lambda L_{5100})$ as a function of z in Figure 2.13, comparing our and other non-local samples with the local AGN samples from Bennert et al. (2011a, 2015). We also include objects from the Park et al. (2015) sample, which expanded the number of $M_{\rm BH} - L_{\rm bulge}$ measurements at $z = 0.36$ and $z = 0.57$. There is clear offset in AGN luminosity as a function of redshift for all non-local samples with respect to local AGN luminosities. As Canalizo et al. (2012) pointed out, the AGN luminosities of non-local objects tend to reside at $\log_{10}(L_{5100}/\text{erg s}^{-1}) > 43.6$. Objects in our sample have AGN luminosities consistent with the local AGN sample up until to $z \sim 0.3$, at which point $\log_{10}(L_{5100}/\text{erg s}^{-1}) > 43.6$. At $z > 0.3$, three out of the four high-luminosity objects in our sample also lie above the $M_{\rm BH} - \sigma_*$ relation. The same trend was observed by Shen et al. (2015) who, by using SDSS virial BH masses to probe the $M_{\rm BH} - \sigma_*$ relation out to $z = 1.0$, found a similar trend with BH mass and AGN luminosity as a function of z. They pointed out that the limited dynamic range and higher average AGN luminosities in Woo et al. (2006, 2008) are responsible for

the observed offset compared to local objects with considerably lower average luminosities. This trend, which is observed here and in other studies of the non-local $M_{\rm BH} - \sigma_*$ relation (Shen et al., 2008; Canalizo et al., 2012; Hiner et al., 2012; Park et al., 2015; Shen et al., 2015), makes it clear that significant statistical biases are at work in luminosity threshold samples. However, as we have shown here, these biases can be overcome by probing lower luminosities and lower BH masses at higher redshifts. Our selection criteria, which selected objects only by broad-line width and the presence of absorption features, was able to probe lower AGN luminosities than previously observed in SE studies, out to $z \sim 0.3$. The eight NLS1s in our sample also have similar AGN luminosities to the local AGN sample up to $z \sim 0.2$. A larger sample of objects selected with similar criteria is necessary to show if we can further probe similar local luminosities at higher redshifts. We note, however, that our ability to probe similar BH mass regimes at higher redshifts assumes that the shapes of the luminosity and BH mass functions do not significantly change with redshift. Likewise, if the scatter in the $M_{\rm BH} - \sigma_*$ relation changes significantly with redshift, it may indicate the presence of additional statistical biases which must be accounted for.

2.6 Discussion

We consider the effects of an evolution of the $M_{\rm BH} - \sigma_*$ relation as a function of cosmic time and its physical interpretation, if real. Woo et al. (2008) measured a significant offset in $M_{\rm BH}$ in non-local BHs, implying a significant evolution in bulge mass over relatively short timescales. Using the scaling relation for central velocity dispersion with stellar mass of SDSS quiescent galaxies from Zahid et al. (2016), we estimate that the offset in $M_{\rm BH}$ from

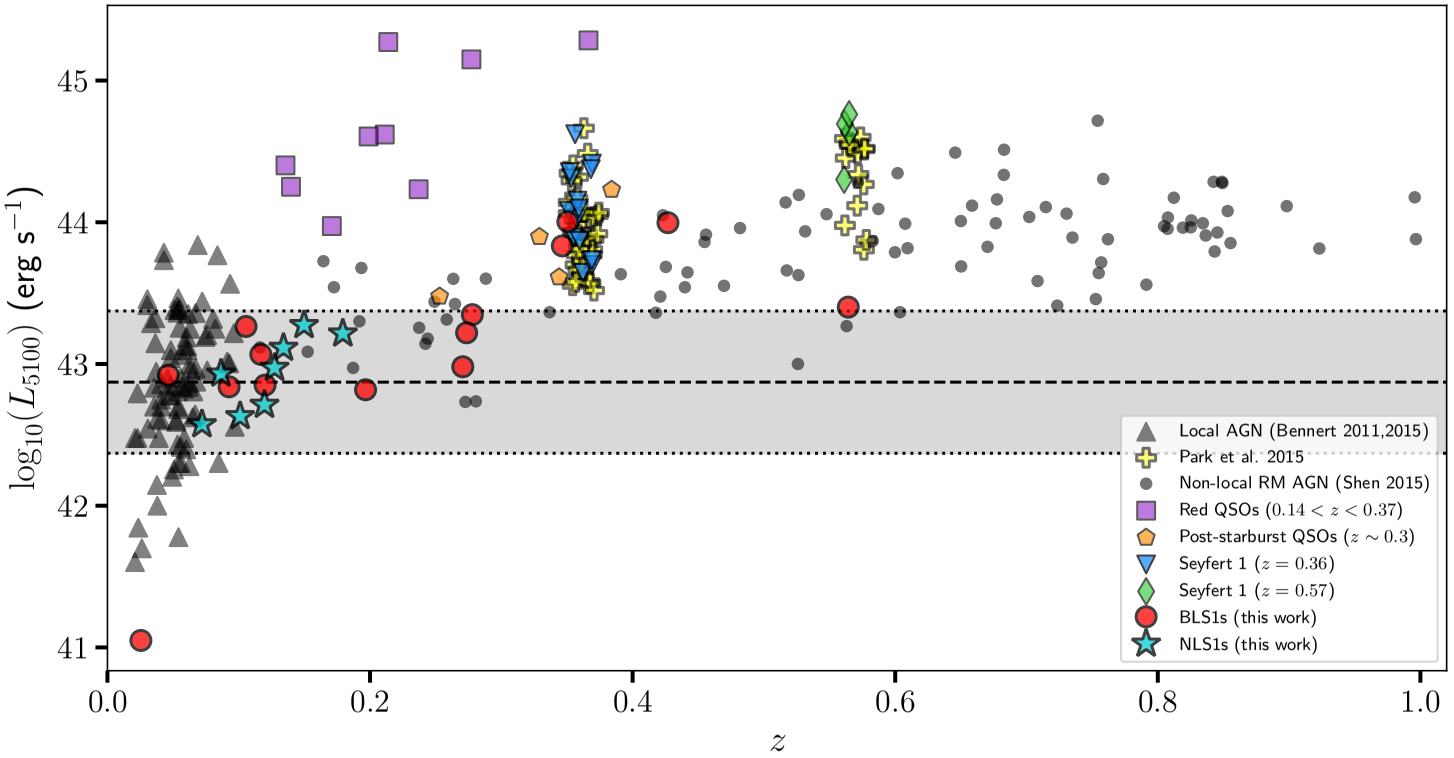

Figure 2.13: Comparison of AGN luminosities for non-local samples as a function of redshift. The dashed line indicates the local average and the gray shaded area represents the scatter of local AGNs from the combined samples of Bennert et al. (2011a, 2015). Non-local objects which have considerable offset from the local $M_{\rm BH} - \sigma_*$ have AGN luminosities higher than the local average, indicating that these samples may be sampling the upper envelope of BH masses at these redshifts due to the luminosity-threshold selection effects. Our sample was able to probe lower-mass BHs out to $z \sim 0.3$, however, it likely suffers from selection effects at higher redshifts.

Woo et al. (2008) implies that bulges must grow by a factor of ~ 6 within 5.5 Gyr ($z = 0.57$) to be consistent with the local relation at $z = 0$. Objects from Canalizo et al. (2012) and Hiner et al. (2012), which also fall significantly above the local relation, further increase the evolution slope and required amount stellar mass assembly. With the inclusion of our objects, we measure an evolution slope of $\gamma = 2.16 \pm 0.62$, which relaxes the amount of bulge growth required to a factor of ~ 4 within 5.5 Gyr. Despite the improved constraints in the local relation and increased non-local sample size, the required mass assembly for non-local bulges necessary to be consistent with the local $M_{\rm BH} - \sigma_*$ relation remains high. The means by which bulges achieve such considerable secular mass assembly are the subject of ongoing debate. It is possible that disruption of stellar disks and/or minor mergers can cause significant bulge growth without significantly growing the SMBH (Croton, 2006a; Jahnke et al., 2009; Bennert et al., 2011b; Cisternas et al., 2011).

It is certainly possible that the evolutionary trend we measure in the $M_{\rm BH} - \sigma_*$ relation is not of physical origin, but the confluence of selection effects and large scatter. In Section 2.5.4.5, we discussed possible biases due to our selection criteria, which may lead to the overmassive BHs we observe at $z > 0.4$ and consequent significant evolution we measure in the $M_{\rm BH} - \sigma_*$ relation. Figure 2.13 clearly shows that we are likely still sampling the upper envelope of BH masses at higher redshifts, which could be driving the evolution slope upwards at the high-redshift end. These biases present the greatest challenge in acquiring an unbiased sample at high redshift, however, we have shown that AGN selection by Hβ line width (and not luminosity) allows us to probe lower SE BH masses at higher redshifts than previously measured, assuming strong stellar absorption features are present to accu-

rately measure σ_*. Furthermore, the 0.44 dex scatter we observe as a function of redshift (see Figure 2.8) is significant and consistent across the entire redshift range of our sample, indicating that any linear trend - and therefore evolution - in the $M_{\rm BH} - \sigma_*$ relation as a function of redshift is weak at best ($r_s = 0.23 \pm 0.04$). The fact that we can fit the points in Figure 2.8 with a constant model (as opposed to a linear model) and achieve nearly identical residual scatter indicates that we lack sufficient evidence for significant evolution in the $M_{\rm BH} - \sigma_*$ relation up to $z \sim 0.6$, and that any measured offset is being driven by a sampling of higher-luminosity AGNs, and therefore higher-mass BHs, at higher redshifts.

We stress that measurements of σ_* are the largest single source of systematic uncertainty for objects on the $M_{\rm BH} - \sigma_*$ relation due mainly to low S/N at high redshift. Even if σ_* can be directly measured from stellar absorption features, biases due to the choice of fitting region, the presence of Fe II contamination, possible AGN dilution, and host galaxy morphology can introduce significant uncertainties which may contribute the scatter in the $M_{\rm BH} - \sigma_*$ relation. The obvious alternative to measuring faint stellar absorption features at high redshift is to use brighter gas emission features, such as the [O III]λ5007 width, as a proxy for σ_*, assuming that the NLR gas traces the stellar LOSVD of bulges. We found that obtaining accurate measurements of the [O III] width is not trivial, as one must correct for both Fe II contamination and the presence of blue-wing features which may indicate the presence of gas outflows (also see, e.g., Komossa et al. (2008a), Woo et al. (2016) and Bennert et al. (2018)). Still, there remains considerable scatter in the relationship between σ_* and [O III] width, and therefore studies of the $M_{\rm BH} - \sigma_*$ relation using [O III] as a proxy should only be used in statistical samples.

We have shown that, aside from their high Eddington ratios, the host galaxies of NLS1 objects contain BHs that reside on the local $M_{\rm BH} - \sigma_*$ relation. Furthermore, the NLS1s in our sample are in good agreement with lower-mass bulges on the FP relation, indicating that their observed narrow broad-lines are likely due to having lower BH masses (as the $M_{\rm BH} - \sigma_*$ relation would imply) and not an observational or geometrical peculiarity of the BLR as previous studies have suggested. However, a larger sample of NLS1s is still required to determine their behavior on the $M_{\rm BH} - \sigma_*$ relation at higher redshifts.

We conclude that there is insufficient evidence for evolution in the $M_{\rm BH} - \sigma_*$ relation up to $z \sim 0.6$ due to comparable scatter of objects on the local $M_{\rm BH} - \sigma_*$ relation and for objects at lower redshifts. The case for no evolution within our sampled redshift range is consistent with the results found by Schramm & Silverman (2013), who found good agreement with the local $M_{\rm BH} - M_{\rm bulge}$ relation using a sample of 18 X-ray-selected AGNs at $0.5 < z < 1.2$. It is still possible that there is significant offset at higher redshifts than those sampled here. For instance, using gravitationally lensed quasar hosts, Peng et al. (2006) found that BHs grew significantly faster than their hosts at $z > 1.7$. Bennert et al. (2011b) also found significant offset in the $M_{\rm BH} - M_{\rm bulge}$ relation at $z \sim 2$, implying the BH mass growth pre-dates bulge formation. However, current studies of the non-local $M_{\rm BH} - \sigma_*$ relation still lack statistically representative samples of BHs at the currently sampled redshifts, as we are likely still sampling the upper envelope BH masses due to selection effects. These are the hurdles that must be overcome in order to conclusively determine any evolution in the $M_{\rm BH} - \sigma_*$ relation, and which we will address in future studies.

2.7 Notes on Individual Objects

2.7.1 J092438.88+560746.8

This object is a clear outlier on the $M_{\rm BH} - L_{\rm bulge}$ relation shown in Figure 2.12, characterized by an apparent undermassive BH relative to its host-bulge luminosity. The *HST* imaging of this object clearly shows it is host to a disk and spiral arm component, which we fit using GALFIT to ensure accurate deconvolution of the bulge component (see Figure 2.6). It is also worth noting that the host-disk component appears to have a considerably low axis ratio (b/a), which implies that the disk is being viewed at high inclination assuming that the disk is circular. As a result, we correct the measured stellar velocity dispersion for inclination in Section 2.3.2. Curiously, this object is not an outlier on either the $M_{\rm BH} - \sigma_*$ or FP relations. The offset from the $M_{\rm BH} - L_{\rm bulge}$ relation appears to be due not from an intrinsically high bulge luminosity, but an undermassive BH stemming from a faint AGN continuum. The luminosity at 5100 Å is the lowest measured in our sample, resulting in an Eddington ratio of $< 1\%$ (the lowest point in Figure 2.9).

We also observe a significant difference in broad Hβ line width between the Keck and SDSS spectra. Here we classify this object as a BLS1 galaxy, since we measure FWHM$_{\rm H\beta} = 2650 \pm 205$ km s^{-1} with the Keck spectrum; however, a fit to the SDSS spectrum of this object indicates that it is closer to an NLS1 galaxy with FWHM$_{\rm H\beta} = 2036 \pm 75$ km s^{-1}. One possibility for the difference in line width could be due to the aperture size between Keck and SDSS observations. Since this object has $z = 0.025$, the $3''$ diameter fiber of the SDSS contains significantly more host-galaxy flux, and therefore absorption, than the $1''$ slit we used for our Keck observations, leading to a more asymmetric – and possibly

narrower – line profile.

The second possibility is that J092438 could be a "changing-look AGN". These are AGNs showing strong variability in their broad Balmer lines, and their continuum emission, and in the most extreme cases they change completely from Seyfert 2 (no BLR at all detected) to a Seyfert 1 (very strong BLR), the cause of which remains debated. This could be caused by cases of extreme extinction, but perhaps more likely by strong intrinsic continuum variability, to which the BLR responds. In most cases, the Seyfert type does not change completely, but the broad-line widths do vary significantly. Runco et al. (2016) found that, in a sample of 102 local SDSS AGNs, followed up using Keck, $\sim 38\%$ showed appreciable BLR line variability.

Both Keck and SDSS observations are consistent with J092438 being in a low state, indicated by its very faint AGN continuum and Balmer lines. If one assumes that the AGN continuum is intrinsically stronger, and its BLR lines are stronger and broader, then J092438 would be more consistent with the $M_{\rm BH} - L_{\rm bulge}$ relation and fall within the upper limits of the scatter of the local $M_{\rm BH} - \sigma_*$ relation.

2.7.2 J145640.99+524727.2

This BLS1 object is characterized by a strong attenuation in the [O III] complex, requiring the region to be masked during the multi-component fitting process, as shown in Figure 2.4. Narrow Hβ does not appear attenuated and could be fit without constraints. The [O III]$\lambda\lambda 4959, 5007$ lines appear to have a considerably larger width than the narrow component of Hβ, and appear to be asymmetric with respect to the expected [O III] line centers, implying that this object exhibits the asymmetric blue-wing components discussed in

Section 2.3.4.2. The decomposition of the [O III]$\lambda\lambda$4959, 5007 lines could not be performed, however, due to the severe attenuation. The strong attenuation does not appear to be the result of poor skyline subtraction during the spectral reduction process, as the SDSS spectrum appears to show the same attenuation. Cales et al. (2013) also studied this object as part of a sample of 38 post-starburst quasars with spectra obtained from the Kitt Peak National Observatory Mayall 4 m telescope, but could not fit the [O III]$\lambda\lambda$4959, 5007 lines in their spectrum either. The spectrum also exhibits very strong broad Fe II emission, which can be seen on either side of the Hβ/[O III]$\lambda\lambda$4959, 5007 complex in Figure 2.2. More notably, [O III]λ4363, which requires higher temperatures and densities than [O III]$\lambda\lambda$4959, 5007 (Osterbrock, 1989), is very strong. The shape of [O III]λ4363 is also much more symmetric than the more attenuated and more asymmetric [O III]$\lambda\lambda$4959, 5007 doublet. Zakamska et al. (2016) found similar line profiles in high-redshift red quasars, which may indicate that [O III]$\lambda\lambda$4959, 5007 may originate from a region of lower-density and more easily accelerated gas than [O III]λ4363. Finally, our Keck observations also reveal absorption blueward of broad Mg II. These features are common characteristics in low-ionization broad absorption line (LoBAL) QSOs. Zhang et al. (2010) studied a sample of 68 SDSS LoBAL QSOs at $0.4 < z \leq 0.8$, some of which show similar Mg II absorption as J145640. No previous studies classify J145640 as a LoBAL, likely due to the fact that at $z = 0.278$, Mg II remains ($\sim$ 220 Å) below the wavelength coverage of the SDSS. We plot the full Keck spectrum of J145640 in Figure 2.14. LoBALs are thought to be associated with high accretion rates and/or early stages of AGN/galaxy evolution (Canalizo & Stockton, 2001; Lazarova et al., 2012; Hamann et al., 2019). We find no significant differences between the properties of J145640 and those

of the rest of the sample, with the exception of its Eddington ratio, which is the second lowest in the sample.

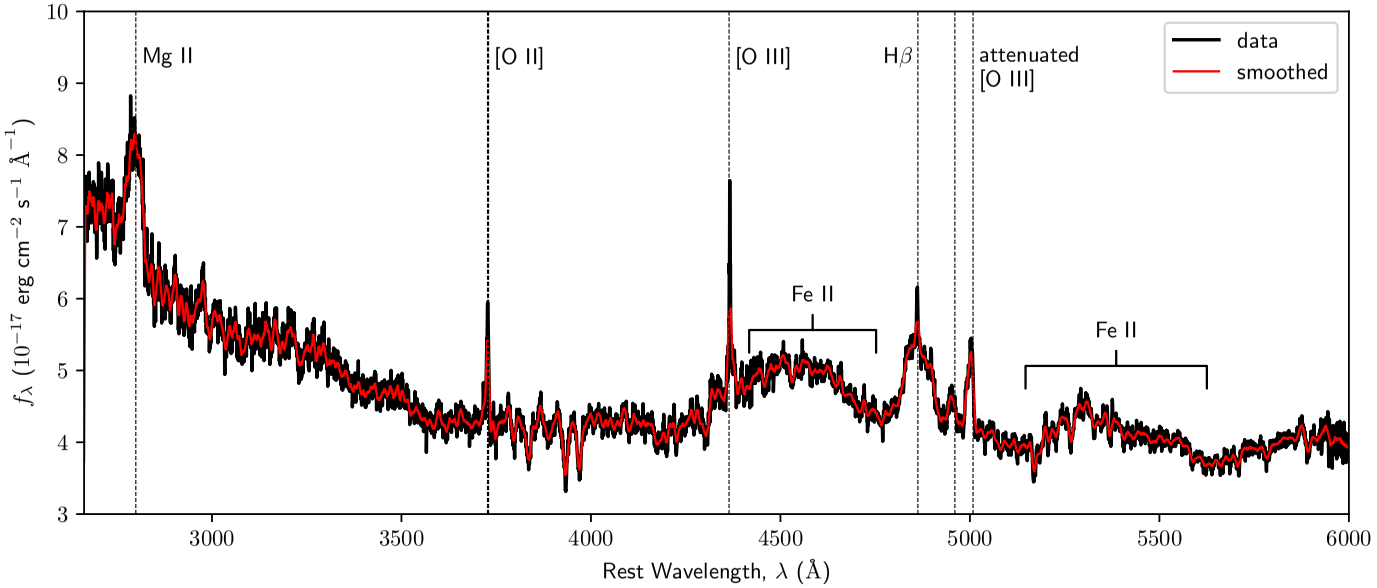

Figure 2.14: Full Keck/LRIS spectrum of J145640, the features of which are consistent with that of a low-ionization broad absorption line quasi-stellar object. We have labeled strong emission features, most notably the characteristic strong broad Fe II emission and attenuated [O III]$\lambda\lambda 4959, 5007$ emission. Absorption in Mg II can be seen blueward of the emission line.

Chapter 3

Bayesian AGN Decomposition Analysis for SDSS Spectra

3.1 Introduction

Data analysis codes, recipes, and software distributions for spectroscopic data analysis have become commonplace in the astronomy and astrophysics community, especially in the advent of large all-sky surveys, such as the Sloan Digital Sky Survey (SDSS; York et al., 2000) and the highly-anticipated Large Synoptic Survey Telescope (LSST; Ivezić et al., 2019). Despite their widespread use, many of the computational methods used to perform these analyses are either (1) not shared by authors for various reasons, or (2) not open source and cannot be accessed without the purchasing of proprietary software. In addition to this, many data analysis pipelines designed for large-scale surveys are written with the intent of fitting as many objects as possible in the shortest amount of time, while other analysis recipes may

be suited for more-detailed analyses. Finally, many software packages are suited for fitting for specific types of objects, usually either galaxies or active galactic nuclei (AGNs), with no general means of fitting for both or other types of objects. As astronomy advances through the 21st century, sacrificing quality for speed will no longer be necessary given the increasingly widespread use and availability of supercomputing resources in astronomy. Likewise, software designed for fitting specific astronomical objects will yield to more general fitting algorithms which can fit a diverse set of objects autonomously and in great detail.

Some notable existing software packages and codes have attempted to address the aforementioned issues. The Gas AND Absorption Line Fitting (GANDALF; Sarzi et al. (2006)) code was one of the first large-scale algorithms to fully decompose gas emission from stellar absorption features, using penalized pixel-fitting (pPXF; Cappellari & Emsellem (2004); Cappellari (2017)) to measure the stellar line-of-sight velocity distribution (LOSVD) with stellar templates. In the context of AGN studies, GANDALF was ill-suited for the complexities of fitting type 1 AGNs, which contain additional features such as broad lines, Fe II emission, power-law continuum, and possible "blue-wing" components indicative of outflowing narrow-line gas. The Quasar Spectral Fitting package (QSFit; Calderone et al. (2017)) allowed for fitting of type 1 AGNs with a variety of optional features, making it ideal for large-scale surveys of many thousands of objects. More recently, the release of PyQSOFit (Guo et al., 2018) includes many similar features of QSFit with the added functionality of Python. However, since QSFit and PyQSOFit use a library of galaxy templates to model the host galaxy component instead of attempting to model the LOSVD using stellar templates, AGNs with a strong stellar continuum component, such as type 2 AGNs, suffer from poor

continuum modelling. Furthermore, while both GANDALF and QSFit are technically open source, they are implemented using proprietary software and language (namely IDL). While certain licensed software may have once been prevalent in the astronomical community, there is a growing push toward open source software that can be easily shared, modified, and used among the research community. Among these open source languages is Python, which is one of the fastest growing programming languages for data analysis today, and its widespread use makes it ideal for research in the astronomical community.

We address the limitations of current spectral fitting codes with a comprehensive fitting package implemented in Python and utilizing a Markov-Chain Monte Carlo (MCMC) fitting approach for accurate estimation of parameters and uncertainties, which we call *Bayesian AGN Decomposition Analysis for SDSS Spectra* (BADASS). In its current version, BADASS is written for the SDSS spectra data model in the optical (specifically 3460 Å to 9463 Å, based on choice of stellar template library), however, because it is written in Python and is open source[1], it can be easily modified to accommodate other instruments, wavelength ranges, stellar libraries, templates, and has already been used successfully to perform decomposition on 22 type 1 AGNs observed with the Keck-I LRIS instrument (Sexton et al., 2019).

The BADASS software attempts to address some notable and relevant problems with spectral fitting software available today. Because BADASS was designed for detailed decomposition of type 1 AGNs, which contain various components such as forbidden "narrow" (typical FWHM < 500 km s^{-1}) and permitted "broad" (typical FWHM > 500 km s^{-1}) emission lines, broad and narrow Fe II emission, AGN power-law continuum, "blue-wing"

[1] https://github.com/remingtonsexton/BADASS3

outflow components, and the host galaxy stellar continuum, these components can be optionally turned on or off to fit less-complex objects such as type 2 AGNs or non-AGN host galaxies altogether, with all of these options easily configured through the Jupyter Notebook (Kluyver et al., 2016) interface. As a result, BADASS can be deployed for fitting a diverse range of astronomical objects and customized to the user's needs. Additionally, the choice of Python as the programming language of BADASS follows suit with a number of other software packages, such as Astropy (Astropy Collaboration et al., 2013), which aim to replace antiquated software such as IRAF (Valdes, 1984) or proprietary languages such as IDL, for astronomers now entering the field and/or adopting the Python programming language for their analyses. If anything, the open source nature of the BADASS software will serve as a template for developing various implementations of the software for individual specific needs.

To our knowledge, the BADASS algorithm is the first of its kind to address a number of issues specific to the fitting of AGN spectra that other algorithms have yet to implement. First, BADASS was initially designed to fit all spectral components simultaneously, as opposed to masking regions of spectrum and fitting components separately. This is specifically advantageous for the decomposition of the stellar continuum and Fe II emission from other components for studies of AGN and host galaxy relations such as the the $M_{\rm BH}-\sigma_*$ relation. As noted in Sexton et al. (2019), stellar kinematics remain the single-most difficult quantity to measure in type 1 AGN, and obtaining reliable values and uncertainties for stellar quantities is a non-trivial effort that includes a number caveats and systematics which can be difficult to account for (Greene & Ho, 2006b). Simultaneous fitting with Fe II

emission templates also allows for detailed study of Fe II emission properties of type 1 AGN while taking into account the underlying stellar continuum. Finally, BADASS is the first software of its kind to use specific criteria for the automated detection and decomposition of outflow components in forbidden emission lines, which have recently become a topic of much study in the context of AGN and host galaxy evolution (see Section 4.1 and references therein).

The Bayesian MCMC approach used by BADASS for fitting spectral parameters is unique in that it provides an easily-extensible framework for the user to modify the fitting model, free parameters, and convergence criteria. Many fitting software packages typically utilize a simpler least-squares minimization approach, however, it is recommended (almost universally) to perform Monte Carlo resampling of the data and re-fitting (also known as "bootstrapping") to ensure accurate estimation of uncertainties. While the least-squares approach is typically faster, an MCMC approach allows the user to estimate robust uncertainties, visualize possible degeneracies, and assess how well individual parameters are constrained or if they have properly converged on a solution. While fitting algorithms that utilize random-sampling techniques admittedly suffer from slower runtimes, modern personal computers capable of multi-processing to decrease runtimes are becoming commonplace. Since BADASS utilizes the affine invariant MCMC sampler *emcee* (Foreman-Mackey et al., 2013), multi-processing is also an available option for fitting large samples of objects. The use of powerful Bayesian and computational techniques, open source framework, and diverse fitting options together make help achieve the ultimate goal of BADASS, which is to provide the most detailed and versatile fitting software for optical spectra in future sky

surveys.

We describe the BADASS model construction, fitting procedure, and autocorrelation analysis used to assess parameter convergence in Section 3.2. We then discuss tests of the recovery of σ_* as a function of signal-to-noise (S/N), Fe II strength, and AGN continuum dilution in Section 3.3. In Chapter 4 we discuss the significant correlations between stellar velocity dispersion σ_*, the decomposed [O III] core and outflow dispersions of the [O III]λ5007 emission line found using BADASS.

Throughout this work, we assume a standard cosmology of $\Omega_m = 0.27$, $\Omega_\Lambda = 0.73$, and $H_0 = 71$ km s^{-1} Mpc^{-1}.

3.2 The BADASS Algorithm

In the following subsections, we discuss the BADASS model construction, spectral components, fitting procedure, and autocorrelation analysis used to assess parameter convergence.

3.2.1 Model Construction

BADASS constructs a model for each spectrum under the assumption that all AGN components (i.e., the AGN power-law continuum, emission lines, possible outflows, and Fe II emission) reside atop a host galaxy component whose stellar contribution we wish to measure. A general overview of the model construction is as follows.

First, each spectral component is initialized using reasonable assumptions from the data. For example, the stellar continuum and power-law continuum are initialized at

amplitudes that are each half of the total galaxy continuum level, which is estimated using the median flux of the fitting region. As another example, emission line amplitudes are initialized at the maximum flux value within fixed wavelength regions centered at the expected rest frame locations of the emission line. These initial parameter values need not be exact, as BADASS will iteratively improve on their estimated values with each fitting iteration.

Models of each spectral component are then sequentially subtracted from the original data, and any remaining continuum is assumed to be the stellar continuum contribution, which is then fit with a predefined host galaxy template or empirical stellar templates to estimate the LOSVD. Once all parameters have been estimated and all model components have been constructed, their sum-total is used to assess the quality of the fit to the original data. This process is repeated for each iteration of the algorithm until a best-fit is achieved.

We describe each of the spectral components used for constructing the model below.

3.2.1.1 AGN Power-Law Continuum

In the simplest construction, the non-stellar thermal continuum in type 1 AGNs can be modeled as the sum of different temperature blackbodies at various radii within the AGN accretion disk (Malkan, 1983). This manifests itself in the UV and optical as a "big blue bump", which flattens out at longer wavelengths towards the near-IR, resembling a power-law continuum. We adopt the QSFit simple power-law implementation from Calderone et al. (2017) given by

$$p(\lambda) = A \left(\frac{\lambda}{\lambda_b} \right)^{\alpha_\lambda}, \tag{3.1}$$

where A is the power-law amplitude, α_λ is the power-law index (or spectral slope), and λ_b which is a reference wavelength chosen to be the central wavelength value of the fitting region and determines the break in the power-law model. The power-law amplitude A and slope index α_λ are free parameters throughout the fitting process. The flat priors we set on these parameters dictate that A must be non-negative and no greater than the maximum flux density value of the data, and α_λ can vary in the range [-4,2]. As in QSFit, the reference break wavelength λ_b is fixed by default to be the center wavelength value of the fitting region (i.e., $(\lambda_{\rm max}$-$\lambda_{\rm min})/2$), since the power-law slope is poorly constrained at optical wavelengths, however, this constraint can be relaxed if there is sufficient wavelength coverage in the near-UV. We show different values of the power-law slope in Figure 3.1.

We find that the simple power-law model adequately describes the AGN continuum in the optical, especially if the object fitting region is limited to rest-frame $\lambda_{\rm rest} > 3460$ Å, which is the lower limit of the wavelength range of the Indo-US Stellar Library (Valdes et al., 2004) used for fitting the stellar LOSVD. To better model the true shape of the power-law continuum, a large fitting region at $\lambda_{\rm rest} < 3500$ Å is necessary to better constrain the power-law index α_λ. For fitting regions $\lambda_{\rm rest} > 3500$ Å, the AGN continuum can become highly degenerate with the host galaxy stellar continuum, especially if the shape of the power-law continuum is relatively flat. We nevertheless include a power-law continuum in our fitting model because its inclusion does not affect the overall fitting process.

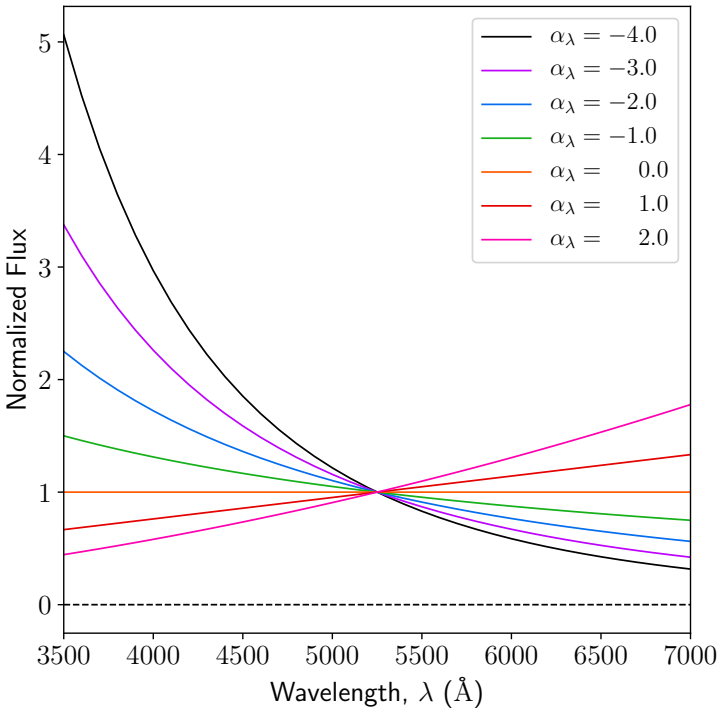

Figure 3.1: The AGN simple power-law model adopted from Calderone et al. (2017). Colors represent different values of α_λ in the range [-4,2] for the wavelength range [3500,7000]. The reference wavelength for this wavelength range, $\lambda_b = 5250$ Å, is the locus of different models for α_λ and is held fixed by default to be the center of the fitting range.

3.2.1.2 Broad and Narrow Emission Lines

All broad and narrow emission line features are, by default, modeled as a simple Gaussian function given by

$$g(\lambda) = A \exp\left[-\frac{1}{2}\left(\frac{(\lambda - v)^2}{\sigma^2}\right)\right], \tag{3.2}$$

where A is the line amplitude, σ is the Gaussian dispersion, and v is the velocity offset of the Gaussian profile from the rest frame wavelength of the line. Some types of objects, such as NLS1s, exhibit broad lines with extended wings (Moran et al., 1996; Leighly, 1999; Véron-Cetty et al., 2001; Berton et al., 2020), for which BADASS can optionally model the emission line with a Lorentzian function given by

$$\ell(\lambda) = \frac{A\gamma^2}{\gamma^2 + (\lambda - v)^2}, \tag{3.3}$$

where $\gamma = \mathrm{FWHM}/2$. A comparison of the two emission line models is shown in Figure 3.2.

Because SDSS spectra are logarithmically-rebinned, each pixel represents a constant velocity scale measured in $\mathrm{km\,s^{-1}}$. This convenience allows us to initialize width and velocity parameters in units of $\mathrm{km\,s^{-1}}$ and fitting performed in units of pixels without the conversion from Å, which is wavelength dependent. All narrow and broad line widths are corrected for the wavelength-dependent instrumental dispersion of the SDSS spectrograph during the fitting process so that final reported widths do not have to be corrected by the user. However, we still place a minimum value for all measured emission line widths to be the velocity scale of our spectra (in units of km $\mathrm{s^{-1}}$ $\mathrm{pixel^{-1}}$), to ensure that emission line

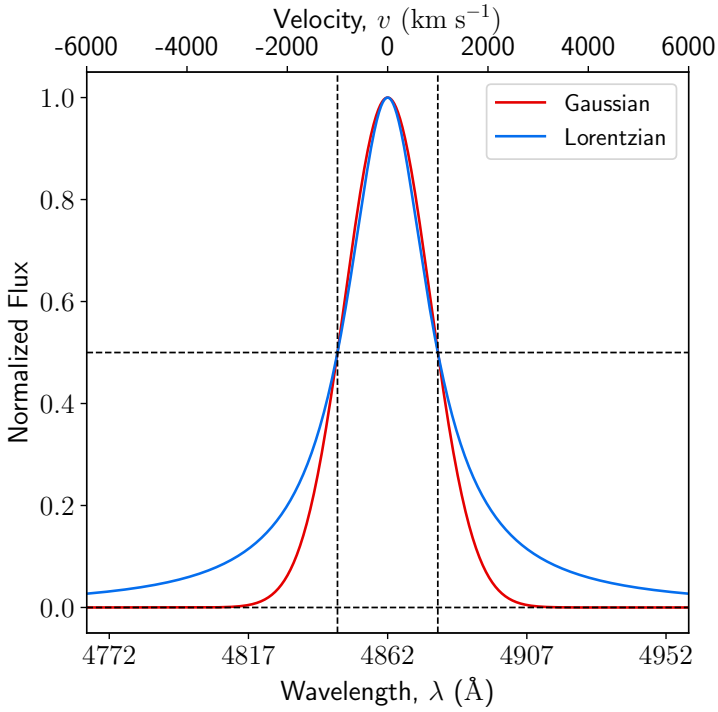

Figure 3.2: A comparison of the Gaussian and Lorentzian emission line models centered on the location rest frame Hβ with a FWHM of 2000 km s^{-1}. Dashed lines indicate the location and width of the FWHM.

widths are at least greater than a single pixel in width to avoid the fitting the noise spikes.

Given the modest resolution ($\sigma \sim 69$ km s^{-1}) and S/N of SDSS spectra , we find that in most cases a simple Gaussian function is sufficient to model the full shape emission lines. Other fitting algorithms attempt to model emission lines in higher detail, using Gauss-Hermite polynomials or additional higher-order moments, in order to account of line asymmetries, which are especially obvious in broad line emission. Sexton et al. (2019) however showed that some line asymmetries can be attributed to strong absorption near Balmer features, and that emission line asymmetries are generally resolved with simple Gaussian models as long as the underlying stellar population is modeled. Narrow lines that exhibit a "blue wing" outflow component, as typically seen in the [O III] emission lines, can be fit as an additional Gaussian component and is a standard feature of BADASS (see Section 3.2.2.2). Higher resolution spectra of nearby objects with strong emission lines can exhibit further complex non-Gaussian profiles even after outflow components are accounted for. These non-Gaussian profiles are best modeled iteratively using multiple Gaussian components until a optimal fit is achieved, and adding additional components can be easily achieved by modification of the BADASS code.

Many line fitting algorithms tie the widths of narrow lines to be the same across the entire fitting region, however, we leave this as an optional constraint in BADASS. The advantage of tying the widths only decreases the number of free parameters, while the disadvantage of tying all narrow line widths to each other can lead to a worse fit. Instead, BADASS ties widths of lines that are nearest to each other in groups. For example, the narrow [N II]/Hα/[S II] line group's widths are tied, and the narrow Hβ/[O III] line group's

widths are tied and fit separately. The Hα/[N II]/[S II] line widths can be biased due to line blending, and/or the presence of outflows and broad lines, and since these lines tend to have larger fluxes than most other lines, they carry greater statistical weight in determining widths if they are tied to other lines in the spectrum. A similar argument can be made for the Hβ/[O III] line group. Ideally, one would model each individual line separate from the rest, however, tying widths is still required for narrow forbidden lines obscured by broad permitted lines. Thus tying widths of groups of lines both reduces fitting bias within each group while also reducing the number of free fitting parameters.

3.2.1.3 Fe II Templates

To account for Fe II emission typically present in the spectra type 1 AGNs, BADASS uses the broad and narrow Fe II templates from Véron-Cetty et al. (2004), which are optimal for subtraction since they include emission features that are commonly found in many Seyfert 1 galaxies, as opposed to a single template based solely on I Zw 1 (Barth et al., 2013). Figure 3.3 shows the narrow the broad Fe II emission features from the Véron-Cetty et al. (2004) template.

All Fe II lines from Véron-Cetty et al. (2004) are modeled as Gaussian functions using Equation 3.2 and are summed together into two separate broad and narrow templates, each of which can be scaled by a multiplicative free-parameter amplitude A during the fit. Following QSFit, the default FWHM of broad and narrow Fe II lines are fixed at 3000 $\mathrm{km\,s^{-1}}$ and 500 $\mathrm{km\,s^{-1}}$, respectively, which are adequate given the resolution and typical S/N of SDSS data. The velocity offset of each line is also fixed by default. We justify holding the FWHM and velocity offsets fixed due to the fact that broad and narrow emission

are blended together and superimposed atop one another, usually at varying amplitudes. This leads to a strong degeneracy in both the FWHM and velocity offsets in these features. However, the FWHM and velocity offset constraints can be optionally turned off or adjusted to particular values for each the broad and narrow templates for more-detailed fitting.

In addition to the template from Véron-Cetty et al. (2004), BADASS can alternatively use the temperature-dependent Fe II model from Kovačević et al. (2010), which independently models each of the F, S, and G atomic transitions of Fe II, as well as some strong lines from I Zw 1, in the region between 4400 Å and 5500 Å, with amplitude, FWHM, velocity offset, and temperature as free parameters. The template from Kovačević et al. (2010), while slightly smaller in wavelength coverage compared to the Véron-Cetty et al. (2004) template, can more accurately model objects with particularly strong Fe II such as NLS1s (Véron-Cetty et al., 2001; Xu et al., 2012; Rakshit et al., 2017). Individual transition amplitudes, widths, and velocity offsets can be optionally fixed during the fitting process as well.

3.2.1.4 Host galaxy & Stellar Absorption Features

The original purpose of BADASS was to extract the host galaxy contribution in type 1 AGN spectra, and in particular, estimate the stellar LOSVD to obtain stellar velocity v_* and stellar velocity dispersion σ_*. In this regard, BADASS serves as a wrapper for the stellar-template fitting code pPXF (Cappellari & Emsellem, 2004; Cappellari, 2017), allowing the user to optionally fit the underlying stellar population to extract stellar kinematics. After subtracting off all the aforementioned components from the original data, BADASS

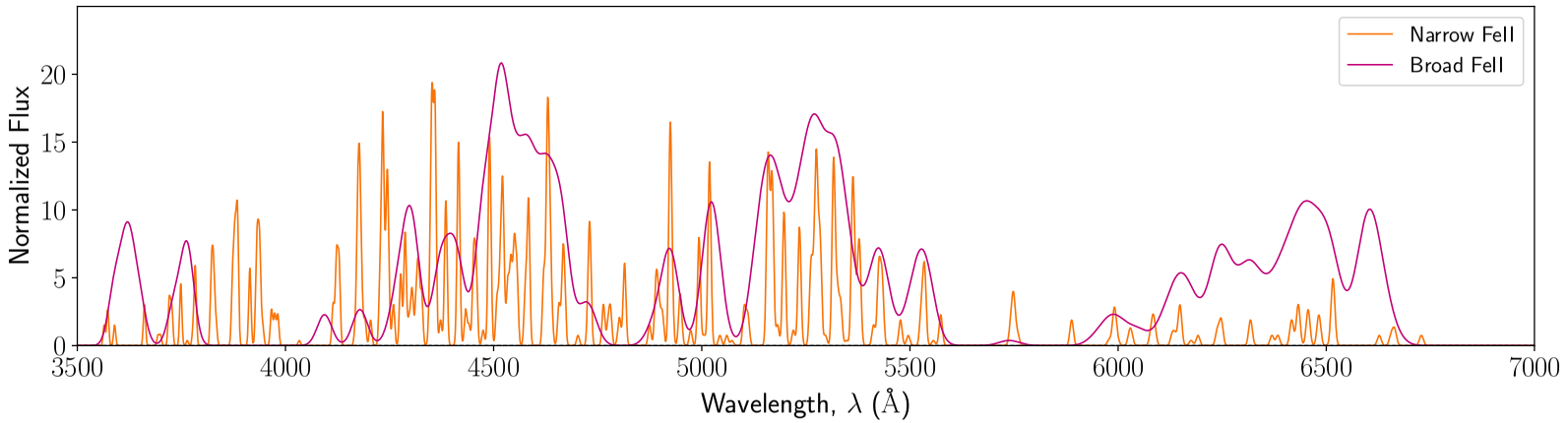

Figure 3.3: Broad and narrow Fe II templates from Véron-Cetty et al. (2004), which (by default) have fixed zero velocity offset and fixed width in BADASS. Broad Fe II is initialized with a FWHM of 3000 $\mathrm{km\,s^{-1}}$, and narrow Fe II with a FWHM of 500 $\mathrm{km\,s^{-1}}$, and held constant throughout the fitting process, following the implementation of QSFit (Calderone et al., 2017).

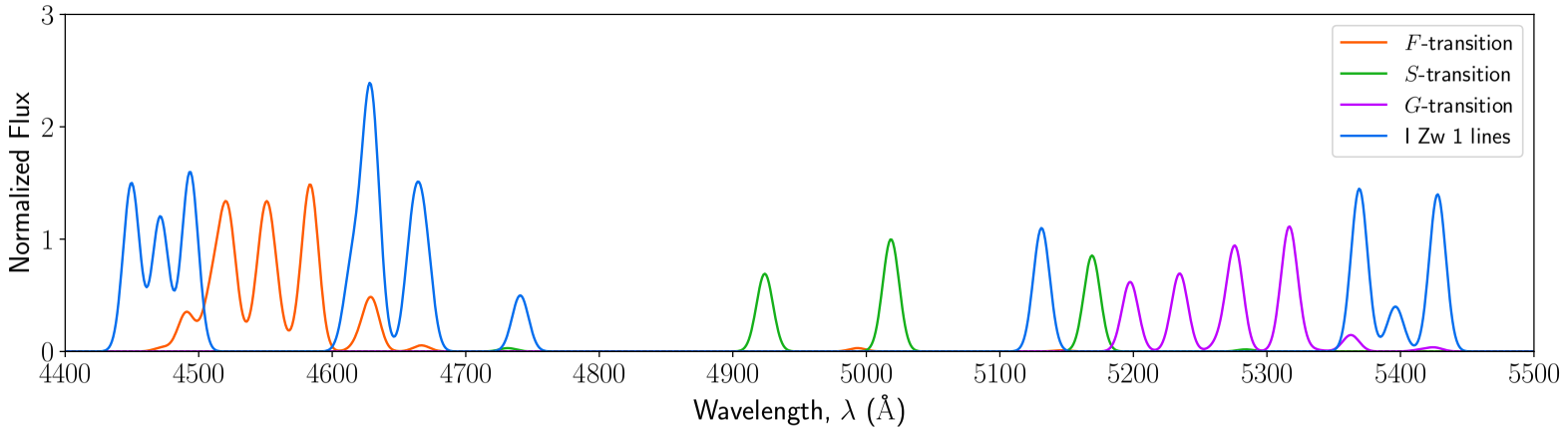

Figure 3.4: The temperature-dependent Fe II template from Kovačević et al. (2010) for a more-detailed analysis of optical Fe II emission. BADASS independently models each of the F, S, and G atomic transitions of Fe II, as well as some strong lines from I Zw 1, in the region between 4400 Å and 5500 Å, with amplitude, FWHM, velocity offset, and temperature as a free-parameters.

models the stellar population using 50 empirical stellar templates from the Indo-US Library of Coudé Feed Stellar Spectra (Valdes et al., 2004). The Indo-US Library was chosen for its high-resolution (FWHM resolution of 1.35 Å; Beifiori et al. (2011)) as well as its wide wavelength coverage from 3460 Å to 9464 Å. The 50 chosen templates include the full range of spectral types from O to M, and were specifically chosen for minimal gaps in coverage. We find that using 40-50 stellar templates strikes an optimal balance between reducing the chances of template mismatch and large computation times, since the non-negative least squares routine used by pPXF for choosing templates and calculating weights carries the largest computational overhead for BADASS and scales with the number of templates used in the fit.

By default, only v_* and σ_* are fit for SDSS spectra, however, if given higher-resolution spectra, it is still possible for pPXF to estimate the higher-order Gauss-Hermite moments of the LOSVD. One caveat to fitting the LOSVD via stellar template fitting is the limited wavelength range of the stellar template library chosen for fitting the LOSVD. In this regard, the Indo-US Library is provides the largest optical range and highest resolution for currently available empirical stellar libraries. However, if one chooses to use a different library of stellar templates, the LOSVD fitting range can be extended.

In general, the quality of the fit to the LOSVD is S/N dependent. We find that if if the continuum S/N< 10, estimates of v_* and σ_* can have uncertainties $> 50\%$, therefore, we allow the user to optionally disable fitting of the LOSVD and instead fit the stellar continuum with a single stellar population (SSP) model generated using the MILES Tune Stellar Libraries Webtool (Vazdekis et al., 2010), which is initialized with a metallicity [M/H] $= 0.0$,

age of 10.0 Gyr, and dispersion of 100 $\mathrm{km\,s^{-1}}$ to match the depth of stellar absorption features typically seen in SDSS galaxies. The SSP template is normalized at 5500 Å and is scaled by a multiplicative factor that is a free-parameter during the fitting process. We also include alternative MILES SSP models with ages ranging from 0.1 Gyr to 14.0 Gyr which can be used as optional substitutes. We show a range of MILES SSP models which can be used by BADASS in Figure 3.5.

Due to the limited range of the MILES stellar library, if the fitting range is outside (3525 Å $\leq \lambda \leq$ 7500 Å), SSP models from Maraston et al. (2009) are used instead, which have a coverage of (1150 Å $\leq \lambda \leq$ 25000 Å), however have much larger dispersions that do not match strong stellar absorption features in SDSS spectra.

We note that dispersions measured with pPXF already take into account the instrumental dispersion of the SDSS, since it first convolves input templates to the resolution of the SDSS before the fitting process. We nonetheless place a lower limit on the allowed values for σ_* to be the velocity scale (in units of km $\mathrm{s^{-1}}$ $\mathrm{pix^{-1}}$) of the input spectra.

3.2.2 Fitting Procedure

3.2.2.1 Determination of Initial Parameter Values

As is true for all fitting algorithms, the number of required MCMC iterations required for convergence on a solution is sensitive to the initial parameter values. Ideally, one should initialize parameters as close as possible to their actual posterior values in order to minimize the number of iterations used for searching parameter spaces and maximize the number of posterior sampling iterations. To do this, we employ maximum likelihood esti-

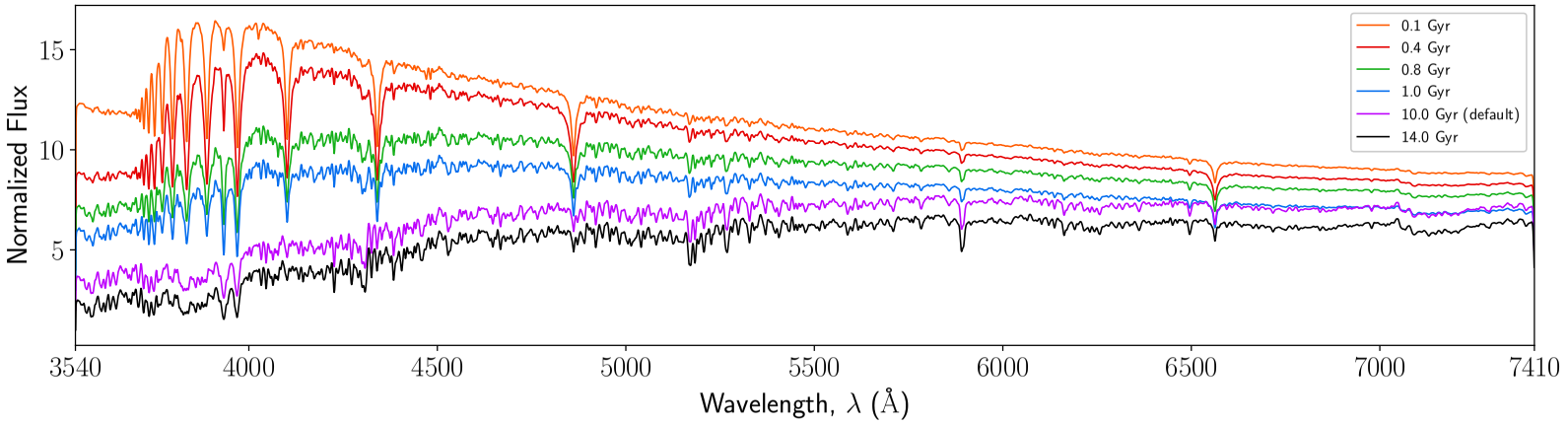

Figure 3.5: Single stellar population models from Vazdekis et al. (2010) generated using the MILES Tune Stellar Libraries webtool used for fitting the host galaxy contribution if the LOSVD (stellar template) fitting is not performed.

mation of all parameters using the SciPy (Virtanen et al., 2020) `scipy.optimize.minimize` function to find the *negative* maximum (minimum) of the log-likelihood function, which we derive as follows.

We assume that each datum of the spectrum can be approximated as a normally distributed random variable of mean $y_{\rm data,i}$ and standard deviation σ_i. The likelihood of the data given the model $y_{\rm model}$ is given by

$$L = \prod_{i=1}^{N} \frac{1}{(2\pi\sigma^2)^{1/2}} \exp\left[-\frac{(y_{\rm data,i} - y_{\rm model,i})^2}{\sigma_i^2}\right] \tag{3.4}$$

Since Equation 3.4 can result in very large values, which often times exceeds the numerical precision of most computing machines, it is easier to use the natural log of the likelihood, i.e., the *log-likelihood*:

$$\mathcal{L} = \log(L) = -\frac{1}{2}\sum_{i=1}^{N} \log(2\pi\sigma_i^2) + \frac{(y_{\rm data,i} - y_{\rm model,i})^2}{\sigma_i^2}, \tag{3.5}$$

The constant terms in this sum that do not change from one iteration to the next, including $\log(2\pi\sigma_i^2)$, can be dropped, as they do not play a role in determination of the minimum. The log-likelihood is therefore given by

$$\mathcal{L} = \sum_{i=1}^{N} \frac{(y_{\rm data,i} - y_{\rm model,i})^2}{\sigma_i^2}, \tag{3.6}$$

where the sum is performed over each spectral channel i for each datum $y_{\rm data,i}$, $y_{\rm model,i}$ is the value of the model at each i, and σ_i is the 1σ uncertainty at each i determined from the SDSS inverse variance of the spectrum.

The *scipy.optimize.minimize* function, which employs the built-in Sequential Least SQuares Programming (SLSQP; Kraft (1988)) method, is used to include bounds and constraints on all parameters. Parameter bounds, which are the minimum and maximum values for each parameter, are determined from the data. For example, the emission line amplitudes must be non-negative, and can have a maximum value of the data in the fitting region. These simple boundary conditions, which are later used by *emcee*, are effective in limiting the parameter space for timely convergence. Constraints on parameters are used for the testing for possible blueshifted wing components in [O III] (see Section 3.2.2.2).

By default, BADASS only performs one maximum likelihood fit to obtain initial parameter values in the interest of time and a single fit is sufficient for initializing parameters for MCMC fitting. However, if one chooses not to perform MCMC fitting, or if one desires more robust initial parameter values, BADASS can optionally perform multiple iterations of maximum likelihood fitting by resampling the spectra with random normally-distributed noise from the spectral variance and re-fitting the spectrum, i.e., Monte Carlo "bootstrapping".

3.2.2.2 Testing for Presence of Outflows in Narrow Emission Lines

Additional "blue wing" components in narrow emission lines, indicative of possible outflowing gas from the central BH, are known to be commonplace in AGN-host galaxies (Nelson & Whittle, 1996; Mullaney et al., 2013; Woo et al., 2016; Zakamska & Greene, 2014; Rakshit & Woo, 2018; DiPompeo et al., 2018; Davies et al., 2020). If present, failure to account for the blue excess in narrow line emission can lead to significant difference in measured line quantities, especially if one uses narrow line width as a proxy for σ_*

(Woo et al., 2006; Komossa & Xu, 2007; Sexton et al., 2019; Bennert et al., 2018).

Blue wings are most visibly obvious in the narrow [O III] emission line in type 1 AGNs because [O III] is not significantly contaminated by nearby broad lines. To determine if blue wings are present, BADASS can optionally perform preliminary single-Gaussian and double-Gaussian fits to the Hβ/[O III] or Hα/[N II]/[S II] narrow line complexes to test if an additional Gaussian component in the model is justified. The test for outflows is identical to the process used for fitting initial parameter values using maximum likelihood estimation (i.e., Monte Carlo bootstrapping). The double-Gaussian fit makes the assumption that outflows are present by including a narrower "core" and a broader "outflow" component for the narrow emission lines. Monte Carlo bootstrapping for a user-defined set of iterations is then used to obtain uncertainties on core and outflow components to assess the quality of the fit. During the fitting process the FWHM of the outflow component is constrained to be greater than the core component, and the amplitude of the outflow component is constrained to be less than the core component, following what is typically seen in the literature. However, since outflows are not necessarily always blueshifted, but sometimes at equal or redshifted velocities with respect to the core component (albeit in rare occurrences), we do not constrain the velocity offset of either component during the fitting process. This feature is useful for detecting outflow components found in star forming galaxies, which are known to be less offset from the core component causing a more symmetric [O III] line profile (Cicone et al., 2016; Davies et al., 2019; Manzano-King et al., 2019).

To quantify the presence of outflows in [O III], we visually identify 63 objects from a sample of 173 known type 1 AGN that both (1) exhibit the characteristic line profile

asymmetry commonly seen in the literature, and (2) have a measurable non-gravitational component in [O III] relative to the systemic (stellar) velocity dispersion (this is discussed in detail in Section 4.2) and derive empirical relationships between measurable parameters that recover these objects. After BADASS performs fits for both the single-Gaussian (no-outflow) and double-Gaussian (outflow) models, the following empirical diagnostics are used to determine if a secondary outflow component is justified in the model:

$$\text{Amplitude metric:} \quad \frac{A_{\rm outflow}}{\left(\sigma^2_{\rm noise} + \delta A^2_{\rm outflow}\right)^{1/2}} > 3.0 \tag{3.7}$$

$$\text{Width metric:} \quad \frac{\sigma_{\rm outflow} - \sigma_{\rm core}}{\left(\delta\sigma^2_{\rm outflow} + \delta\sigma^2_{\rm core}\right)^{1/2}} > 1.0 \tag{3.8}$$

$$\text{Velocity metric:} \quad \frac{v_{\rm core} - v_{\rm outflow}}{\left(\delta v^2_{\rm core} + \delta v^2_{\rm outflow}\right)^{1/2}} > 1.0 \tag{3.9}$$

$$F\text{-statistic:} \quad \frac{\left(\dfrac{\rm RSS_{no\ outflow} - RSS_{outflow}}{k_2 - k_1}\right)}{\left(\dfrac{\rm RSS_{outflow}}{N - k_2}\right)} \tag{3.10}$$

where A is the line amplitude (in units of 10^{-17} erg cm^{-2} s^{-1} Å^{-1}), σ is the Gaussian dispersion (FWHM/2.355; in units of km s^{-1}), v is the velocity offset of the line relative to the rest frame of the overall spectra (in units of km s^{-1}). The quantity RSS is the sum-of-squares of the residuals within $\pm 3\sigma$ of the full (core + outflow) [O III] line profile, $k_1 = 3$ is the number of degrees of freedom in the single-Gaussian model, $k_2 = 6$ is the

number of degrees of freedom in the double-Gaussian model, and N is the size of the sample used to calculate RSS. If parameters of the core or outflow models do not adhere to their bounds or approach to the limits of their constraints, which in turn violates the number of degrees of freedom for each model, BADASS flags the relevant parameters and defaults to a single-Gaussian (no-outflow) model.

Equation 3.7 is a measure of the amplitude of outflow component above the noise, while Equations 3.8 and 3.9 are a measure of how much we can significantly detect measurable differences between the core and outflow FWHM and velocity offsets, respectively. Another way of interpreting Equations 3.7, 3.8, and 3.9 is the uncertainty overlap between parameter values, which signifies how well BADASS can separate core and outflow components in parameter space. For example, a value of 2 for the width metric indicates that there is 2σ separation between the best-fit values of the core and outflow FWHM.

Equation 3.10 is statistical F-test for model comparison between the single- and double-Gaussian models. The F-statistic in this context calculates unexplained variance between the outflow and no-outflow models as a fraction of the unexplained variance in the outflow model alone. The F-statistic is then used to calculate a p-value, which if less than a critical value (by default, $\alpha = 0.05$), indicates that we can reject the null hypothesis that there is no significant difference between the single- and double-Gaussian models, and that the difference is greater than that which could be attributed to random chance. We express our confidence in the outflow model by calculating $1 - \alpha$. For example, $\alpha = 0.05$ indicates a 95% confidence that a double-Gaussian model explains the variance in fitting the [O III] profile significantly better than a single-Gaussian model.

All of these criteria can be toggled on or off, and the significance and confidence thresholds for each can be changed to meet the user's specific needs. We find that the above criteria provides a satisfactory method in finding objects with strong blueshifted excess in [O III] with a success rate of $> 90\%$ compared to visual identification, and recommend this method to determine if strong outflows are present or if the [O III] core dispersion needed as a surrogate for σ_* when it cannot be otherwise measured. We note that while these empirical criteria are successful in describing the types of objects in our sample, more sophisticated statistical modelling and cross-validation techniques with a larger sample will be required to improve the capability of BADASS to identify objects with outflows.

If the above criteria are met, the final set of parameters that are fit with *emcee* will include a second Gaussian component for all narrow lines in the fitting region, otherwise, the final model will only fit a single Gaussian component to each narrow line. It is important to note that any emission line, whether it exhibits blue excess or not, can be fit with more than one component and produce a better fit. However, if one is using the core component of [O III] as a surrogate for stellar velocity dispersion, using a two component fit when only one component is justified by the data can significantly underestimate the stellar velocity dispersion. Likewise, not correcting for a strong and clearly visible outflow component can significantly overestimate the stellar velocity dispersion if the core component is used as a surrogate.

While BADASS can perform tests for outflows on either the Hβ or Hα region, it is recommended that if one wants to fit outflows in both the Hβ and Hα regions that it be done simultaneously, in which case BADASS uses the [O III]λ5007 outflow component to

constrain the properties of the outflow components for Hα, [N II], and [S II]. This constraint is activated because even if a broad line is not present in Hα, narrow Hα and [N II] can still be severely blended due to the resolution of the SDSS. However, if one chooses to fit outflows in Hα independently from Hβ, it is still possible at the user's discretion.

As an aside, there is no single definition or quantification of what constitutes an "outflow" in regards to emission lines. BADASS, admittedly, can only detect significantly broad and offset [O III] wings that are commonly seen in the literature, but outflows can generally produce a wide range of emission line profiles. For example, Bae & Woo (2016) modeled biconical outflows in 3D and found that the emission line profile of outflows is strongly dependent on orientation and dust extinction, resulting in sometimes redshifted and non-Gaussian profiles. Some models also indicate that a high-velocity outflow can be present without exhibiting an broad blue excess due simply to bicone orientation.

The criteria we present here constitute a *preliminary* means of filtering out objects with strong outflows which may cause significant residuals if not taken into account, and can make no claims as to whether an outflow is present if the secondary outflow component is close to the velocity offset or width of the primary core component of the emission line. The best method of determining if a secondary component is necessary is to perform a full fit with the double-Gaussian model with *emcee*, as well as fitting the LOSVD to estimate the gravitational influence of the NLR, and examining the individual parameter chains to ensure that they are not degenerate and have converged on a stable solution.

3.2.2.3 Final Parameter Fitting

Final parameter fitting performed using MCMC begins by initializing each parameter at its maximum likelihood value obtained from the initial fit. We use Equation 3.6 as the likelihood probability and initialize each parameter with a flat prior with lower and upper bounds determined by the data. If the model contains outflow components, constraints on outflow parameters (see Section 3.2.2.2) are included in their respective flat priors. We place an additional constraint on broad line components, whose widths must be greater than narrow line widths, if broad lines are included in the fit. Fitting is then performed iteratively via MCMC until each component's parameters have converged. Each parameter space is randomly sampled using the affine invariant MCMC sampler *emcee* until a user-defined number of iterations is reached or if autocorrelation analysis (recommended) has determined that parameter convergence has been sufficiently reached (see Section 3.2.2.4). Fitting using the *emcee* package is advantageous since the use of multiple simultaneous "walkers" efficiently explores each parameter space in parallel, all of which form MCMC parameter "chains" from which the final posterior distribution is estimated for each parameter, as shown in Figure 3.6.

The values of parameters estimated using the initial maximum likelihood routine (*scipy.optimize.minimize*) can differ substantially from parameters estimated using emcee, as shown in Figure 3.6. This large difference is attributed to the stellar continuum model used in each fit. The initial fit uses only a single SSP template to estimate the contribution to the stellar continuum. The *scipy.optimize.minimize* algorithm, while relatively fast, is not sensitive enough to fit the LOSVD with stellar templates in addition to many other

component parameters. Fitting the LOSVD requires many iterations due to the fact that even moderate changes in stellar velocity or stellar velocity dispersion need not drastically change the shape of the resulting stellar continuum model, or drastically change the value of the calculated likelihood, which is partly due to the number and diversity of template stars used by BADASS. Instead, the *scipy.optimize.minimize* algorithm prioritizes the fitting of components that have the greatest effect on the calculated likelihood, such as emission lines and continuum amplitudes. In short, the limitations of the *scipy.optimize.minimize* routine are due to a combination of (1) degeneracies inherent to the stellar template fitting process, and (2) the likelihood threshold requirements needed for *scipy.optimize.minimize* to achieve a solution As a result, the initial fitting routine in BADASS only fits a single SSP template for the stellar continuum.

The advantage of MCMC fitting with *emcee* allows for prolonged simultaneous fitting of parameters even after a likelihood threshold has been achieved. Components that are fit very easily (such as emission lines and continuum amplitudes) converge on solutions very quickly, while components that are less sensitive to even moderate changes (such as stellar templates) can continue to converge on a solution, even if the calculated maximum likelihood does not vary considerably. The advantage of MCMC sampling in this context allows BADASS to explore the LOSVD parameter space even after a maximum likelihood has been reached, which allows for greater variation in template stars used for achieving a best fit. In other words, parameter convergence is more heavily dependent on parameter variation (autocorrelation; see Section 3.2.2.4) rather than achieving some maximum likelihood threshold. In the case of the $\mathrm{FWHM}_{\mathrm{H}\beta}$ parameter chain shown in Figure 3.6,

the value of $\mathrm{FWHM}_{\mathrm{H}\beta}$ slowly adjusts to changing stellar templates of varying stellar Hβ absorption. These slow adjustments do not result in significant changes in the likelihood that the *scipy.optimize.minimize* are sensitive to, however, over a prolonged number of fitting iterations, a compromise is eventually reached between the value of $\mathrm{FWHM}_{\mathrm{H}\beta}$ and the stellar continuum absorption estimated from individual stellar templates.

The MCMC fitting process uses the same likelihood function, priors, and constraints used in the initial fitting procedure, but instead produces parameter distributions from which best-fit values and uncertainties can be reliably estimated. The best-fit values are then used to construct a final model, an example of which is shown in Figure 3.7.

3.2.2.4 Autocorrelation Analysis

Over a number of iterations, the values of a parameter can fluctuate significantly as each parameter space is explored. Since some parameters can be strongly correlated (for instance, the AGN power-law continuum component and the stellar continuum component amplitudes), there can exist parameter degeneracies that are not taken into account when using conventional fitting techniques. Parameter fluctuations and degeneracies can also vary as a function of S/N. The nature and diversity of galaxy and AGN data makes determination of parameter convergence a non-trivial issue, especially if the goal is to fit a large number of objects that vary intrinsically or in data quality. Fitting algorithms typically address this by setting the number of fitting iterations to an arbitrarily high number or setting a minimum tolerance in the change in the likelihood value. While these methods of convergence are generally good, they only guarantee convergence in the overall fit to the data, and not on

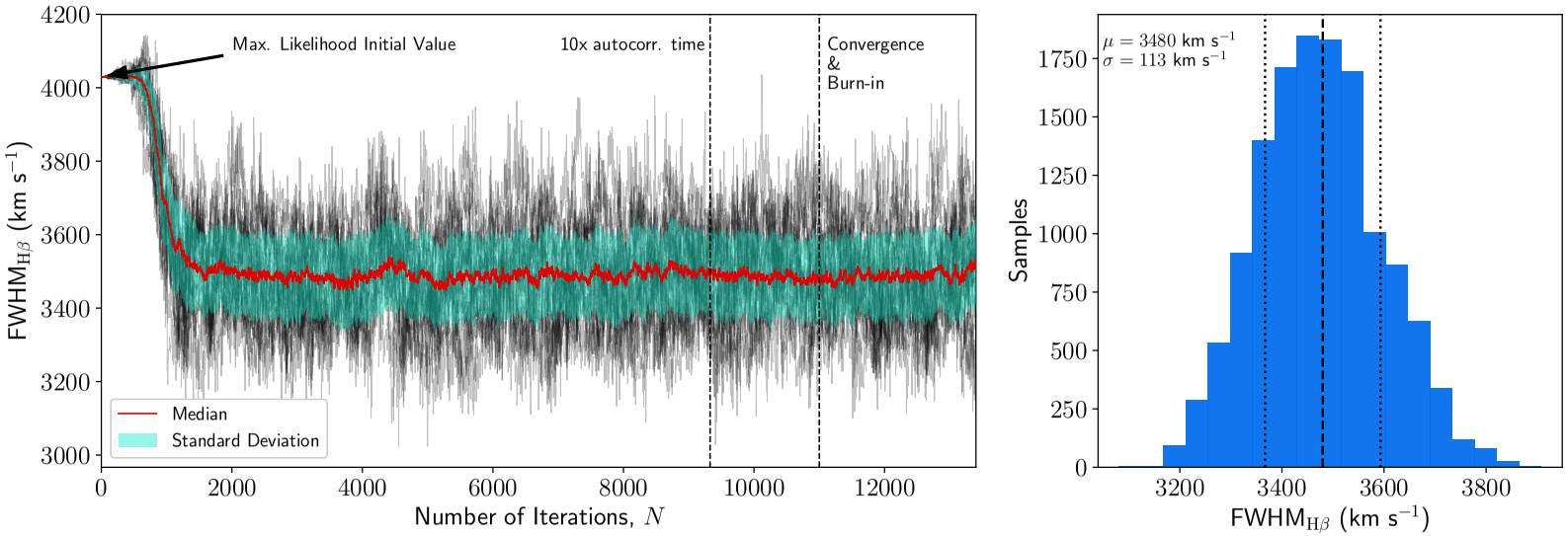

Figure 3.6: *Left*: The FWHM parameter MCMC chain for the Hβ FWHM from the above example performed using 100 walkers. The initial starting position, estimated using maximum likelihood fitting, overestimates the final width of the line by more than 500 km s^{-1}. As other parameters are fit, the value Hβ FWHM decreases and settles into a stable solution by $\sim$ 2000 iterations. Convergence is reached at $\sim$ 11000 iterations (for this example, when 10 times the autocorrelation time per parameter at 10% tolerance per parameter is achieved), and the burn-in is chosen to be the final 2500 iterations after all other parameters has been achieved. *Right*: A histogram of the last 2500 iterations of all 100 walkers.

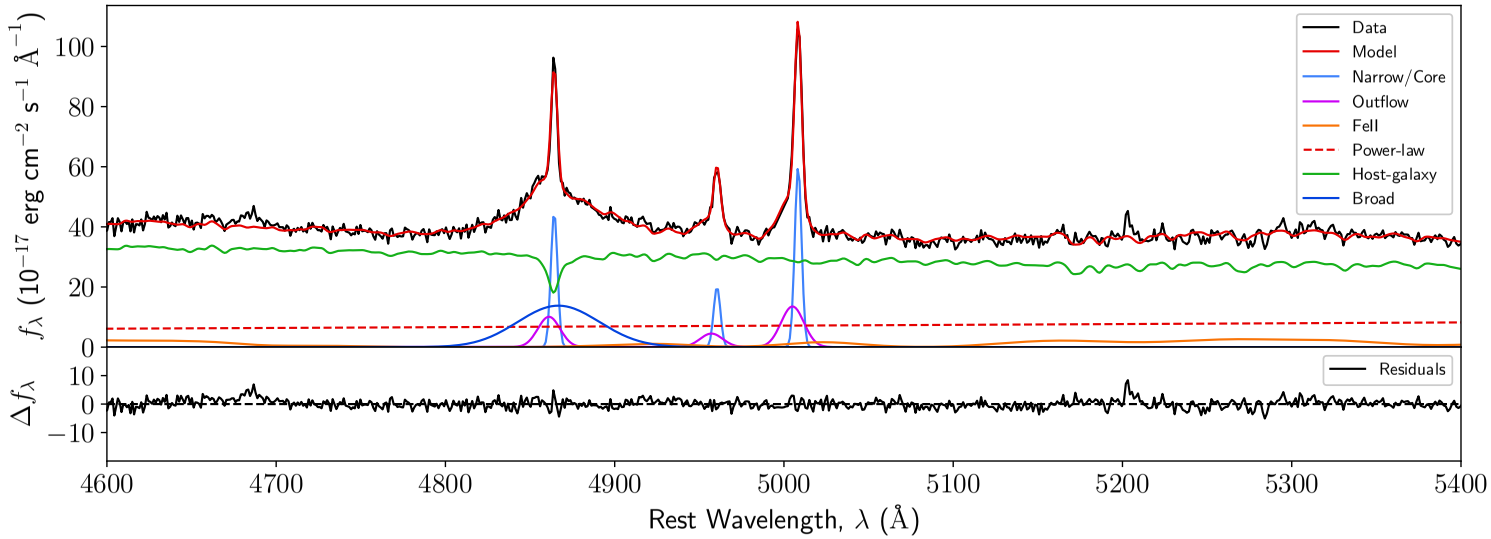

Figure 3.7: An example of the best-fit final model output of a spectrum fit in the Hβ/[O III] region with individual fitting components designated by different colors. This particular object exhibits the blueshifted [O III] outflow components (magenta) which BADASS is designed to detect and fit.

the convergence of individual parameters.

To address this, BADASS employs autocorrelation analysis to assess parameter convergence. Autocorrelation analysis functions are built into *emcee* (see Foreman-Mackey et al. (2013)), however, we tailor these functions for the purposes of spectral fitting. The integrated autocorrelation time, which is the number of iterations required for a parameter chain to produce an independent sample, is calculated for all parameters at incremental fitting iterations (by default, every 100 fitting iterations), and then the convergence criteria are checked to see if they are satisfied by the most current fit parameters. There are two criteria that must be satisfied that define convergence: (1) if calculated autocorrelation times, which are multiplied by some multiplicative factor (by default, 10.0), exceeds the number of performed fitting iterations, and (2) if the difference between the current and previous calculated autocorrelation times is less than a specified percent change (by default, 10%).

In practice, some parameters never reach adequate convergence, usually due to strong degeneracies with other model components (such as Fe II). To accommodate these instances, BADASS offers the user four modes of convergence in terms of the integrated autocorrelation time: (1) mean, (2) median, (3) user-specified parameters, and (4) all parameters. The first two options calculate the mean or median autocorrelation time of *all* free-parameters to determine when an overall solution is reached, however it does not guarantee that all parameters reach convergence. To guarantee the convergence of specific parameters of interest, option (3) allows the user to indicate which specific parameters are considered for autocorrelation analysis, which is useful for ignoring components which have high autocorrelation times (poorly constrained or highly degenerate components) or param-

eters of low importance. Finally, option (4) allows the user to specify that all parameters must converge on a solution, for which BADASS runs until all parameters satisfy the autocorrelation conditions or BADASS reaches the user-defined maximum number of iterations.

Figure 3.8 shows an example of different autocorrelation modes and the required number of iterations for a 17-parameter model. We recommend that the user either select the specific parameters of interest for convergence or simply choose the "mean" criteria. The "median" criteria is less sensitive to outlier parameters (parameters with large autocorrelation times) and will generally perform fewer iterations for convergence. The "all" convergence mode is the most strict type of convergence, however, there is no guarantee that convergence can be reached for all parameters within the set maximum number of iterations, especially if the data has low S/N or there are degenerate parameters.

Once the convergence criteria are met, BADASS continues to fit for a set number of iterations (by default, 2500), which is ultimately used for the posterior distribution to determine the best-fit parameter values and uncertainties. The iteration at which convergence is achieved defines the "burn-in" for the parameter chains, after which all following iterations contribute to the final parameter estimation (i.e, the iterations that contribute to the histogram in Figure 3.6). Note that this is only true if autocorrelation analysis is used to assess convergence (`auto_stop=True`), otherwise, BADASS runs for the maximum number of iterations using the burn-in defined by the user. If for any reason convergence criteria are met and then subsequently violated, BADASS resets the burn-in and continues to sample until convergence is met again. This ensures that convergence is maintained at all times after the burn-in and that a best-fit is not achieved prematurely.

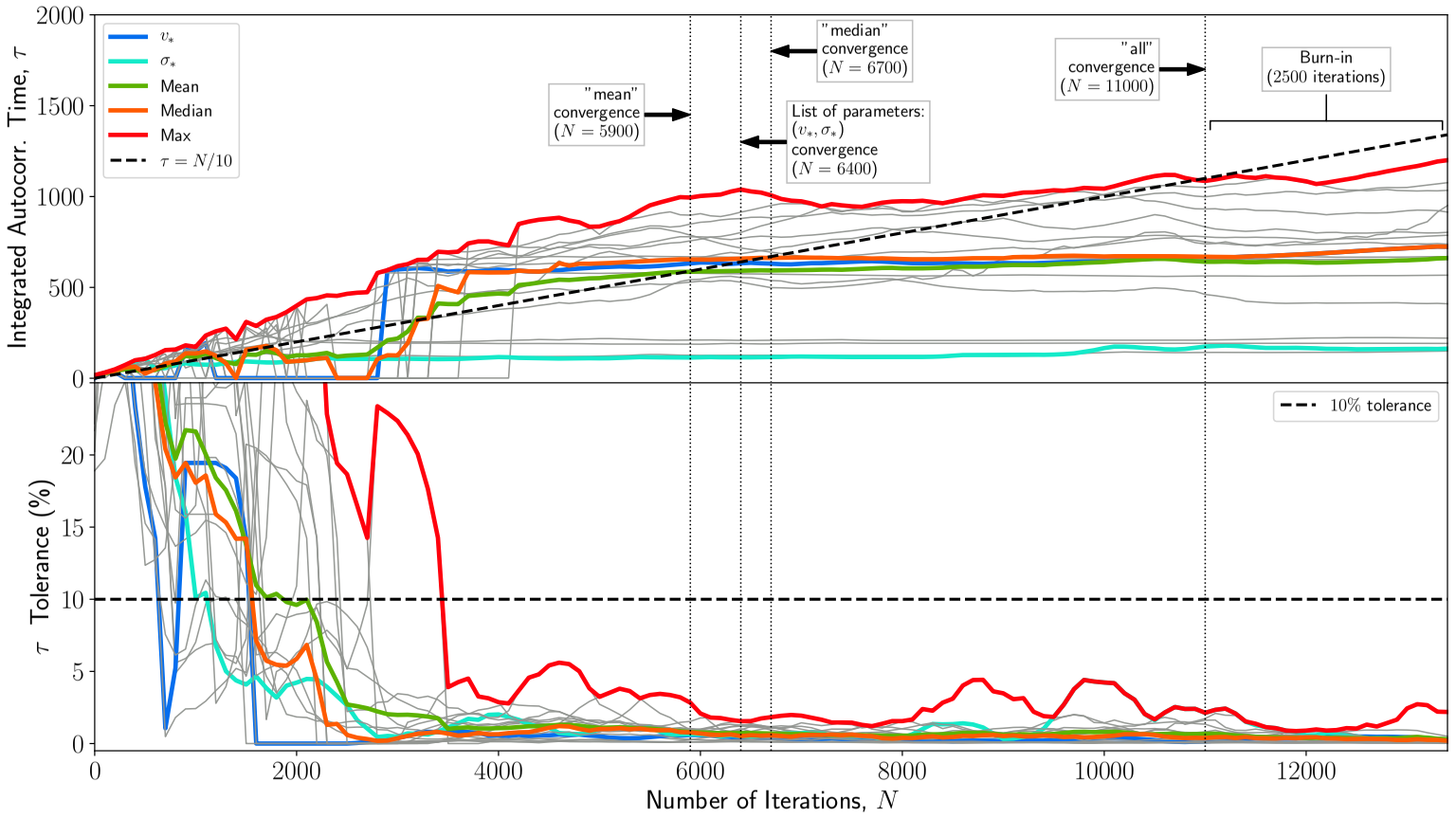

Figure 3.8: An example of different modes of autocorrelation convergence using a model spectrum with 17 free parameters. The "median" mode of convergence typically converges the fastest because it tends to omit outlier τ values, which are typically values for which there are too few iterations to determine an accurate integrated autocorrelation time. By specifying the LOSVD parameters (v_* and σ_*), convergence is reached in 6400 iterations, however many other parameters have not yet converged. The "mean" convergence, is a more strict convergence criteria because all τ estimates are weighted equally. Requiring "all" parameters to converge requires the highest number of iterations and does not guarantee convergence if some parameters cannot converge within the maximum number of iterations.

3.3 Performance Tests

Since one of the primary goals of BADASS is the recovery of the LOSVD, and specifically the stellar velocity dispersion σ_* in AGN host galaxies, we perform a series of performance tests as a function of different components and parameters which may affect measurements of σ_* in the optical Mg Ib/Fe II region from 4400 Å to 5500 Å. We note that the results of these tests are not strictly limited to BADASS, but also general fitting techniques concerned with fitting σ_* in AGN host galaxies.

3.3.1 Recovery of σ_* as a function of S/N

To investigate the effects of S/N level on the recovery of σ_*, we generate a series single stellar population model using the MILES Tune SSP model spectra webtool (Vazdekis et al., 2010). We limit the stellar population ages to 0.1, 1, 5, and 10 Gyr and metallicities [M/H]$= -0.35$, 0.15, and 0.40, and initialize the simulated spectrum at a stellar velocity dispersion $\sigma_* = 90$ km s^{-1}, taking into account the wavelength-dependent dispersion of the SDSS. We then artificially add normally-distributed random noise at various S/N ratios to simulate real observations. The S/N is measured relative to the value of the data in each spectral channel. No other spectral components are added to these SSP models, and only v_* and σ_* are fit.

Figure 3.9 shows the results of S/N tests of various SSP models, where we calculate the percent error (deviation of the best-fit value from the actual value) and the percent uncertainty in σ_*. The results of these tests provide a lower limit to the S/N of SDSS spectra for which σ_* can be reliably measured. Below a S/N of $\sim$15, the best-fit measurement of σ_*

begins to exceed the actual value by more than 10%, and becomes increasingly unreliable at lower S/N. We find a similar result for the average uncertainties of σ_*. We therefore do not recommend measuring the LOSVD at S/N < 20 if the scientific goal is to report accurate stellar kinematics.

There is also a clear offset for the youngest (0.1 Gyr) SSP models, which can be explained by the lack of younger stellar templates included with BADASS, since these stellar types are considerably more rare. In cases where BADASS is used for fitting active star forming galaxies, we recommend one include more O- and B-type templates for fitting the LOSVD and/or disabling the power-law component.

3.3.2 Recovery of σ_* as a function of Fe II Emission

To test the effects of Fe II emission on the measurement of σ_*, we hold the amplitude of the 10 Gyr, [M/H]=0.15 MILES SPP model constant and incrementally add broad and narrow Fe II at an increasing amplitudes, and fit σ_* at S/N levels of 10, 25, 50, 75, and 100. We define the Fe II fraction as a function of stellar continuum amplitude, such that when Fe II amplitude is equal to the stellar continuum amplitude, the Fe II fraction is 100%. We assume that stellar absorption features are at the same velocity (redshift) as Fe II features, and note that subtle differences in velocity may make recovery of σ_* more difficult, however, since narrow and broad Fe II features are typically blended due to the resolution of SDSS, we can only reliably measure the relative amplitude of Fe II emission. At the very least, recovery of σ_* as a function of Fe II fraction gives insight as to how stellar template fitting can recover the underlying stellar continuum when broad and narrow emission line

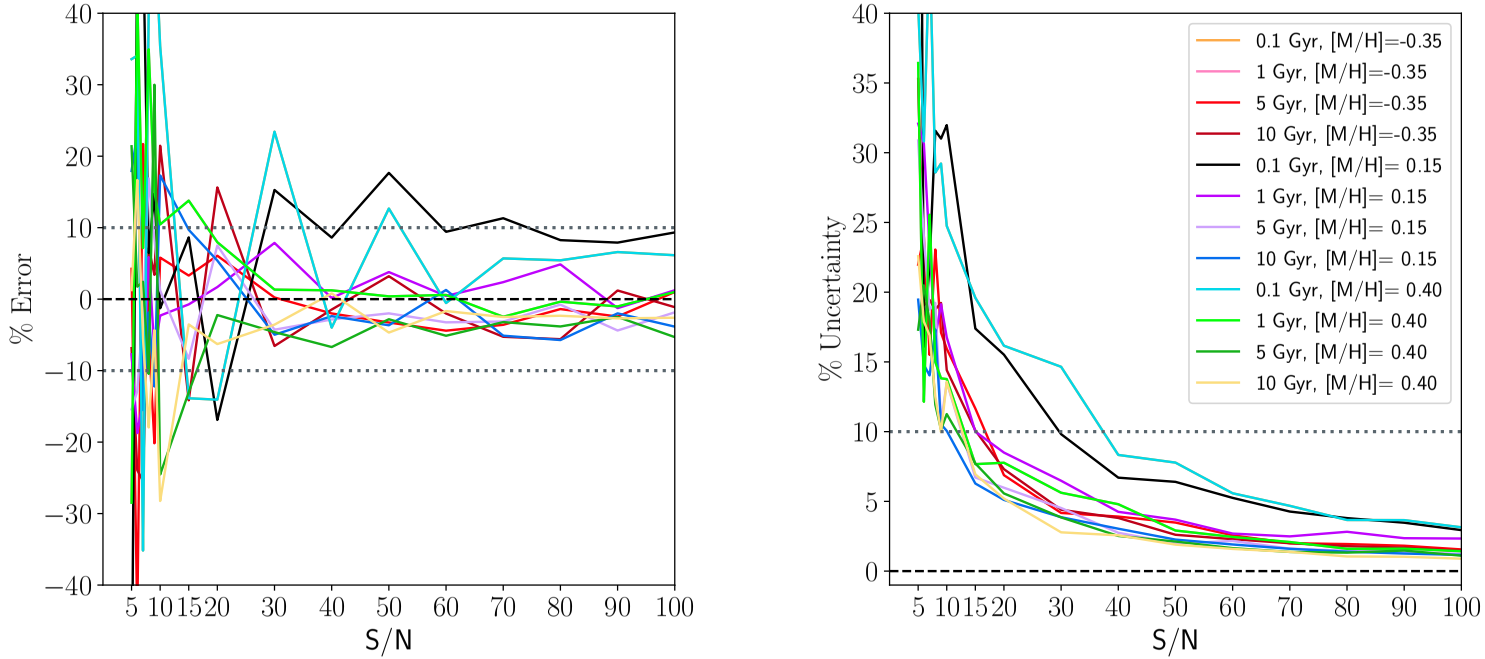

Figure 3.9: Recovery of σ_* as a function of S/N for different fitted MILES SSP models. The figure on the left shows the percent error relative to the actual value of σ_*, which exceeds 10% (green dotted line) below S/N$\sim$15. The figure on the right shows the percent uncertainty, which increases with decreasing S/N. This provides a minimum S/N for which LOSVD measurements can be recovered.

features are superimposed on them.

The results of our tests in the recovery of σ_* as a function of Fe II fraction are shown in Figure 3.10. There is a weak dependence of the best-fit value of σ_* as Fe II fraction increases, and the variance in σ_* increases with decreasing S/N. Even in the most extreme cases, where Fe II fraction exceeds 50%, σ_* can be reliably recovered. Similarly for the uncertainty in σ_*, we find that Fe II fraction has no discernible effect on the measured uncertainties, and are more dependent on S/N. While the effects of differing velocities between stellar absorption and Fe II features are not taken into consideration, these tests indicate that even extreme fractions of Fe II will not significantly affect stellar template matching of the underlying stellar continuum, as long as absorption features are not significantly diluted by the AGN continuum.

3.3.3 Recovery of σ_* as a function of AGN Continuum Dilution

To simulate the effects of AGN continuum dilution, we construct a model spectrum with a flat continuum (power-law slope = 0.0) held at constant amplitude, add the MILES SSP 10 Gyr [M/H]= 0.15 template at decreasing amplitudes, and fit σ_* at S/N levels of 10, 25, 50, 75, and 100. Because young stellar types have a similar continuum shape as an AGN power-law continuum, we do not want the effects of template mismatch to skew measurements of σ_* as a function of dilution of stellar absorption features, therefore we initialize the continuum to be flat.

Figure 3.11 shows the effects of AGN continuum dilution on the recovery of σ_*. We find that continuum dilution can have significant effects even at low S/N. At S/N$<$ 10, σ_*

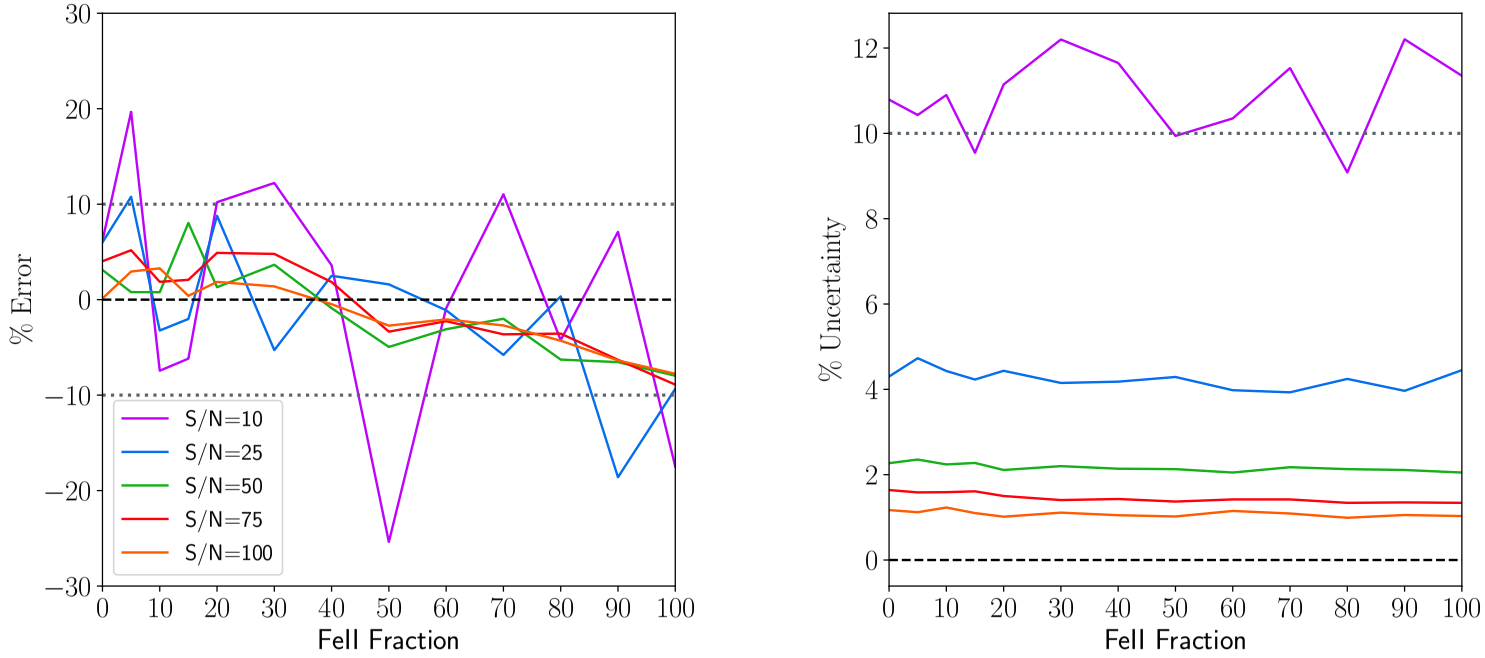

Figure 3.10: Recovery of σ_* as a function of Fe II fraction. There is a weak dependence on the value of σ_* due to Fe II fraction, and a stronger dependence on S/N. Even in the most extreme cases in which the Fe II fraction fraction exceeds 50%, Fe II emission does not significantly affect stellar template fitting.

cannot be recovered if there is more than ∼15% dilution. At S/N of 25 to 50, one can expect to recover σ_* at up to ∼60% dilution. At S/N of 75 to 100, one can reliably recover σ_* with up to ∼ 80% dilution. Beyond 90% dilution, stellar absorption features become excessively flattened out by increasing continuum contribution or are blended with noise, leading to a drastic increase in the measured value of σ_*. We find similar results for the uncertainties in σ_*. Since all type 1 AGNs have some continuum contribution in their spectra, one must use caution in the recovery of σ_* where contribution from the continuum component is greater than ∼50% of the overall spectral continuum level, and especially at low S/N.

Additionally, we tested the recovery of σ_* as a function of the power-law continuum slope to investigate the effects of possible stellar template mismatch, for example, a steep AGN power-law slope resembling the steep stellar continuum of an O- or B-type star, however, we did not find any significant difficulties in the recovery of σ_*.

For objects that exhibit strong Fe II, such as NLS1 or Broad Absorption Line (BAL) objects, we find that strong Fe II is usually accompanied by a steep power-law continuum, indicating very strong AGN continuum fraction and thus dilution. Our tests indicate that it isn't necessarily the presence of Fe II or a steep power-law slope, but the presence of strong continuum dilution that makes it nearly impossible to recover the LOSVD in NLS1 or BAL objects, and extra caution should be used when interpreting LOSVD fitting results from these types of objects.

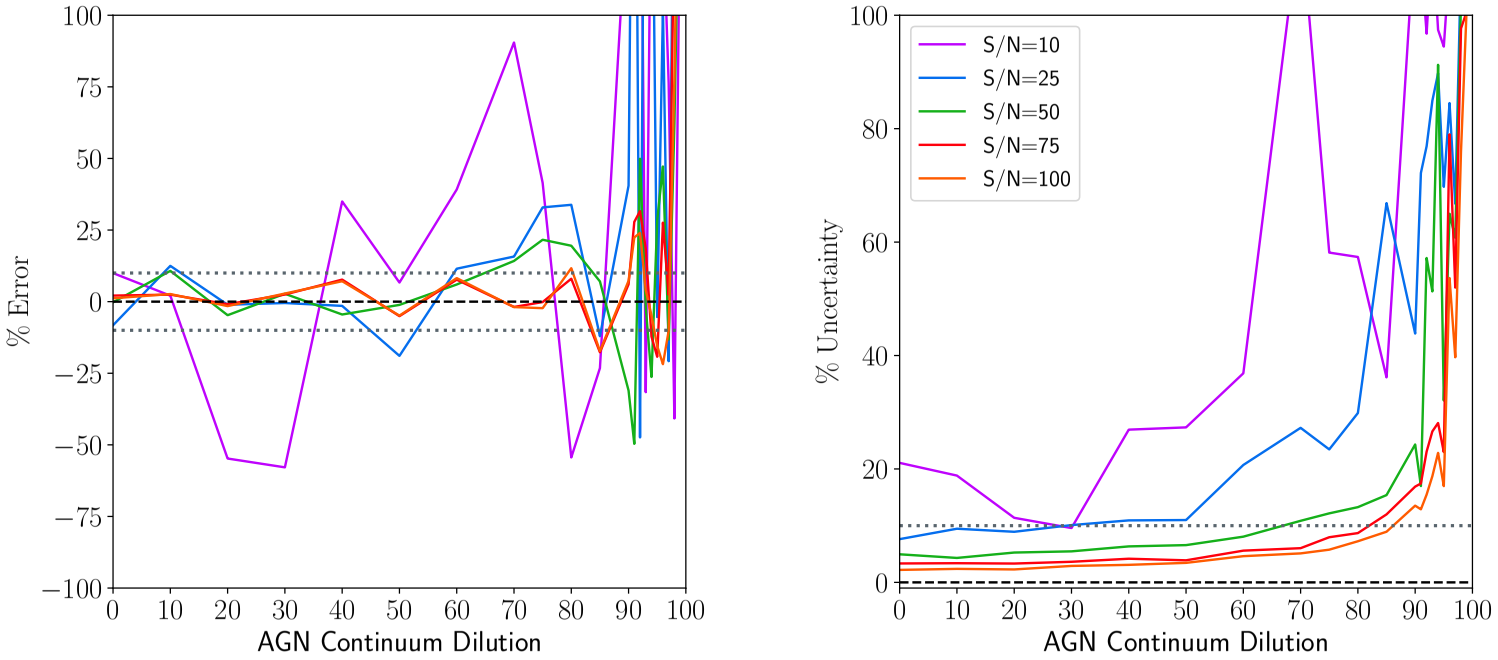

Figure 3.11: The effects of AGN continuum dilution on the recovery of σ_*. The effects of dilution are strongly dependent on S/N. Even at moderate S/N (25-50), σ_* cannot be reliably recovered if the continuum contribution to the overall spectrum is greater than $\sim 50\%$, and becomes impossible at dilutions greater than $\sim 90\%$.

3.4 Summary

To summarize, we have presented BADASS, a new, thoroughly-tested, and powerful fitting software for optical SDSS spectra that is open source and specialized for fitting AGN spectra. Since BADASS can fit numerous components simultaneously, it can be generalized to fit not just AGN spectra, but non-AGN host galaxies as well. The use of MCMC allows the user to fit objects with unprecedented detail, obtain robust uncertainties, and determine the quality of fits using a broad range of metrics and outputs. BADASS also utilizes multiprocessing to efficiently fit large samples of objects without excessive memory overhead.

At the time of this writing, BADASS is being used for a variety of research projects and number of collaborations. For instance, BADASS is being run in a cluster environment to fit over 19,000 SDSS galaxies to determine the significance of outflows as a function of separation distance and as a function of environment. BADASS will also be used to fit a larger sample of type 1 AGN to follow up on results presented here.

Performance tests with BADASS we have presented here in the recovery of σ_* can also be applied to other fitting routines which attempt to measure the LOSVD. We summarize the results of these tests below:

- In non-AGN host galaxies and Type 2 AGN, where significant Fe II and AGN continuum dilution is absent, the LOSVD can be recovered in the Mg Ib/Fe II region (4400 Å -5800 Å) with less than 10% error and uncertainty for S/N $>$ 20. For objects which exhibit active star formation, the steep continuum from young stellar popula-

tions complicates measurements of σ_*, and we recommend to include more O- and B-type template stars and disable the AGN power-law component from the fit.

- Measurements of σ_* are not significantly affected by the inclusion of Fe II, and are more affected by S/N level.

- Dilution of stellar absorption features by strong AGN continuum contributes to the largest error and uncertainty in measuring σ_*. We find that while that strong Fe II and steep AGN power-law slope can be indicative of strong continuum dilution, they are not the root cause. Continuum dilution caused to a large fraction of continuum flux being dominated by the AGN is the root cause of large uncertainties in the estimation of σ_*, and extra caution should be given in the estimate of the LOSVD to objects which exhibit strong Fe II or steep power-law slope, such as NLS1 or BAL objects.

As newer and larger surveys begin to come online, tools such as BADASS, which underscore the need for a generalized open-source framework for fitting a variety of objects with advanced statistical techniques, will be needed for increasingly-detailed analysis of astronomical spectra in the coming decade.

Chapter 4

A Correlation Analysis of [O III]λ5007 Outflow Kinematics with AGN and Host Galaxy Properties

4.1 Introduction

The emergence of scaling relations between supermassive black holes (henceforth, BHs) and their respective host galaxies implies that there is a fundamental mechanism that regulates their co-evolution (Kormendy & Ho, 2013; DeGraf et al., 2015), however the source of this mechanism remains poorly understood. Large statistical studies of galaxies have since established that galactic-scale outflows are commonplace in galaxies that harbor AGNs, hinting that AGN-driven outflows are strong candidates as the feedback messengers between BHs and their host galaxies (Woo et al., 2016; Rakshit & Woo, 2018; Wang et al.,

2018; DiPompeo et al., 2018). There is some observational evidence and theoretical arguments that point to the AGN as the central engine powering galactic scale outflows (King & Pounds, 2015; Fabian, 2012). Additionally, some numerical simulations indicate that AGN feedback can act to disrupt gas cooling and subsequent star formation on galactic scales (Croton et al., 2006; Dubois et al., 2013; Costa et al., 2020), which could give rise to the scaling relations we observe today.

Evidence of such feedback is believed to manifest itself at optical wavelengths as a broad flux-excess in the base or wings of ionized gas emission lines. The flux-excess, which is most easily identified as extended emission in [O III]λ5007, is typically found to be blueshifted with respect the core component of the line, resulting in a significantly asymmetric line profile (Woo et al., 2016; Komossa et al., 2018). These so-called "blue wing" outflow components, which have widths ranging from a few hundred to a few thousand kilometers per second (Harrison et al., 2014; Zakamska et al., 2016; Manzano-King et al., 2019), can be interpreted as outflowing ionized gas that is no longer gravitationally bound to the narrow-line region (NLR) of the galaxy. The absence of a "red wing" in the profile could also indicate significant dust attenuation of outflowing gas moving radially along the line of sight, possibly due to the presence of a galactic disk or AGN torus structure (Bae & Woo, 2016).

Ionized outflows in narrow forbidden emission lines were first identified in early studies of individual radio sources (Grandi, 1977; Afanasev et al., 1980) and it was soon found that signatures of blueshifted outflows were common in larger samples of Seyfert and radio galaxies (Heckman et al., 1980; De Robertis & Osterbrock, 1984; Whittle, 1985). It was

Heckman et al. (1980) that first suggested that because the source of radio emission is due to a compact non-thermal central radio source, the outflow emission must originate along the line of sight between the observer and nuclear region of the galaxy. Later, Heckman et al. (1984) confirmed a relatively strong correlation between radio emission and the presence of outflows which holds true to this day (Jackson & Browne, 1991; Veilleux, 1991; Brotherton, 1996; Mullaney et al., 2013; Zakamska & Greene, 2014). The interest in ionized gas outflows has accelerated within recent years to include extensive IFU observations (Müller-Sánchez et al., 2011; Bae et al., 2017; Freitas et al., 2018; Wylezalek et al., 2020) and hydrodynamical simulations (Melioli & de Gouveia Dal Pino, 2015; Costa et al., 2020).

The kinematic properties of ionized gas outflows in relation to other galaxy and AGN properties have also been explored in detail since their discovery. Nelson & Whittle (1996) first studied the relationship between the bulge and NLR stellar and gas kinematics, showing that the stellar velocity dispersion is relatively correlated with the [O III] gas dispersion, largely due to the gravitational potential of the bulge. However, they noted that [O III] lines with blue wings do not correlate as well with stellar velocity dispersion, indicating the presence of a strong non-gravitational component (Nelson & Whittle, 1996; Mullaney et al., 2013; Woo et al., 2016; Rakshit & Woo, 2018; Wang et al., 2018; DiPompeo et al., 2018). When the blue wing outflow component is properly removed from [O III] line profile, and if any possible Fe II contamination is accounted for, there is better agreement with stellar velocity dispersion (Boroson, 2003; Greene & Ho, 2005). Although the correlation cannot be used on an object-to-object basis, correcting [O III] for outflow components Fe II emission provides a means to estimate stellar velocity dispersion for scaling relations such as the

$M_{\rm BH} - \sigma_*$ relation for larger, higher-redshift statistical samples for which stellar absorption features cannot easily be measured (Wang & Lu, 2001; Boroson, 2003; Woo et al., 2006; Komossa & Xu, 2007; Bennert et al., 2018; Sexton et al., 2019).

Correlations between the kinematics of the [O III] profile and properties of the AGN also exist. For instance, by studying the combined (core+outflow) [O III] profile of large samples of type 2 and type 1 SDSS AGNs, Woo et al. (2016) and Rakshit & Woo (2018) found that the launching velocity of outflows increases with AGN luminosity. Although these studies examined the combined flux-weighted kinematics of the [O III] profile, the results of Bennert et al. (2018) imply that the core component of the [O III] profile can be independently used to estimate stellar velocity dispersion once the outflow component has been removed. This invites inquiry as to whether or not the core or outflow components *independently* may exhibit other relationships with each other or host galaxy properties.

Since detection and fitting of outflow components in [O III] is a feature specifically implemented in BADASS, it presents an opportunity to examine both the core and outflow component kinematics of the [O III] line to investigate all correlations related to ionized gas outflows and the host galaxy to further understand the physical interpretation of the emission line profile. Furthermore, while the use of powerful techniques such as integral field spectroscopy are becoming mainstream for studying the spatially resolved kinematics of AGN host galaxies, these studies are limited to nearby objects. Our objective here is to study the emission line profile of [O III] in local AGNs with outflows to better understand the relationships between outflows, AGNs, and their host galaxies, and apply our knowledge in future studies to objects in the non-local universe for which spatially-resolved observations

are not possible.

Throughout the following sections, we refer to individual objects in our sample using their truncated object ID, for example, J001335. We commonly refer to different components of the double-Gaussian "outflow" model of the [O III] profile as "core" and "outflow" when referring to specific quantities of each, such as $\sigma_{\rm core}$ for the core component velocity dispersion.

4.2 Sample Selection

Since we wish to investigate the relationships between emission line outflow properties of [O III] and both the AGN and host galaxy, we select previously studied nearby type 1 AGNs with SDSS spectroscopy for which BH mass can be measured from the broad Hβ emission and fit these objects using BADASS. For this we included 81 type 1 AGNs studied by Bennert et al. (2018) (henceforth B18) originally selected from SDSS Data Release 6 (DR6), which selected BH masses ($6.6 \leq \log_{10}(M_{\rm BH}/M_{\odot}) \leq 8.7$) at redshifts ($0.02 \leq z \leq 0.10$). The study from B18 performed detailed follow-up observations with Keck/LRIS and performed a detailed decomposition of the [O III] profile to study how different line decompositions affect the $M_{\rm BH} - \sigma_*$ relation, however we fit only the SDSS spectra from B18 here for the purposes of benchmarking the capabilities of BADASS.

To extend the sample to lower-mass BHs we include NLS1 objects from Woo et al. (2015) (henceforth W15), which have a BH mass range of ($5.6 \leq \log_{10}(M_{\rm BH}/M_{\odot}) \leq 7.4$) and redshift range ($0.01 \leq z \leq 0.10$). The W15 sample was selected from SDSS DR7 by sequentially selecting objects with (500 km s^{-1} < FWHM$_{\rm Br.H\beta}$ $\leq$ 2000 km s^{-1}), (800 km s^{-1} <

$\mathrm{FWHM_{Br.H\alpha}} \leq 2200$ km s^{-1}), and a line flux ratio of [O III]/Hβ < 3, resulting in a final sample of 93 NLS1s.

Finally, we include 5 objects from Sexton et al. (2019) (henceforth S19) for which there is sufficient S/N to adequately measure σ_* in the SDSS spectra and have previously determined outflow signatures in the [O III] profile. The S19 sample consists of 22 type 1 AGNs observed with Keck-I LRIS comprised of both BLS1s and NLS1s. The S19 sample has a BH mass range of $(6.3 \leq \log_{10}(M_{\rm BH}/M_\odot) \leq 8.3)$ and is comprised of objects in a broad range of redshifts $(0.03 \leq z \leq 0.57)$ used to study evolution in the $M_{\rm BH} - \sigma_*$ relation in the non-local universe. The 5 objects we include here consists of 4 BLS1 objects and one NLS1 object, which have a BH mass range of $(6.9 \leq \log_{10}(M_{\rm BH}/M_\odot) \leq 8.2)$ and range in redshift from $(0.09 \leq z \leq 0.43)$ as reported by S19.

We removed 16 objects (8 from B18, 8 from W15) for which we could not fit a broad Hβ line, i.e., are type 2 AGNs or have significant host galaxy absorption that makes fitting the broad line highly uncertain. We also removed one object (J112229) listed twice in Table 1 of W15 after confirming there were no nearby neighbors.

The final sample of 162 objects span a BH mass range of $(5.6 \leq \log_{10}(M_{\rm BH}/M_\odot) \leq 8.7)$ and a average redshift of $z = 0.06$. Of these 162 objects, 76 contain measurable outflows in the [O III] line profile as determined using the BADASS outflow criteria given in Section 3.2.2.2. We also included an additional 6 objects which have some visually identifiable asymmetry in the [O III] line profile, which may be attributable to outflows, bringing the total number of objects with outflows to 82. We plot the distribution of BH mass for all 162 objects in Figure 4.1.

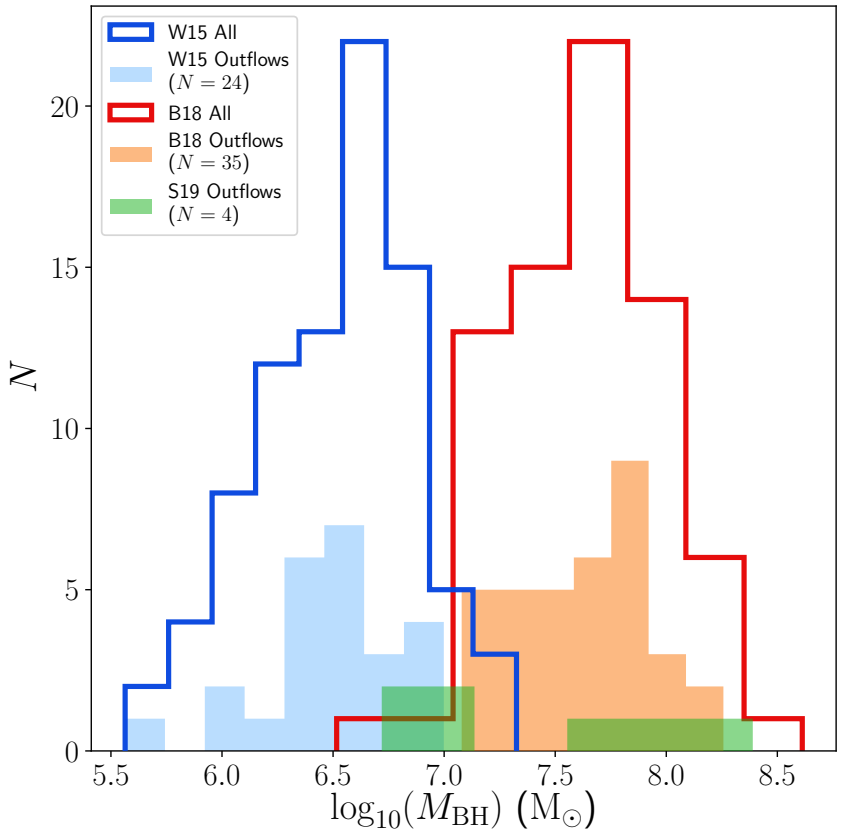

Figure 4.1: Histogram of BH mass for the individual samples from B18, W15, and S19 used for our sample of 162 type 1 AGN. The shaded regions indicate the 63 objects for which we have detected significant non-gravitational outflow signatures in the [O III] profile.

4.3 Methods

4.3.1 Spectral Fitting with BADASS

All 162 objects are re-fit with BADASS in two different ways. The first fit is forced to include outflow components in [O III] even if they do not satisfy the outflow criteria used by BADASS. The second fit is forced to not include outflow components in [O III]. Because we wish to investigate how the non-gravitational component of the [O III] profile correlates with other galaxy properties, both single- and double-Gaussian profiles must be fit to determine which decomposition produces better agreement with σ_*. In both fits we include all other model components, i.e., broad line Hβ, narrow and broad Fe II, power-law continuum, and the LOSVD, in the wavelength range ($4400 \leq \lambda \leq 5800$) following the methods from S19. This fitting region is ideal, not only because it contains the emission lines we want to study, but is also large enough to adequately constrain the amplitude of Fe II emission such that it can be distinguished from the stellar absorption features near Mg Ib used to estimate the LOSVD.

We allow BADASS to fit for a minimum of 2500 iterations with 100 walkers until the LOSVD parameters (stellar velocity and velocity dispersion), and emission line parameters (amplitude,width, and velocity offset) for the broad Hβ, [O III] core, and [O III] outflow components have achieved convergence at a minimum of 10 times the autocorrelation time and within a 10% autocorrelation tolerance, with a post-convergence burn-in of 2500 iterations. We set a maximum iteration ceiling of $50,000$ iterations, however, objects with high S/N and clearly visible outflow profiles in [O III] typically converge by ∼12,000 iterations, which is actually ∼5-10 times the autocorrelation time for the parameters we consider for

convergence.

Using both the BADASS criteria given in Section 3.2.2.2 and by visually inspecting the fits of both the outflow and no-outflow models, we determine that 82 of the 162 objects have outflow components with significant width and offset differences from their core components.

Finally, since we wish to examine the effects of the non-gravitational outflow component of the [O III] profile and compare them to the stronger gravitational component σ_*, we remove 19 objects for which we do not see an improvement in agreement between the $\sigma_{\rm core}$ and σ_*, which is necessary to remove objects for which BADASS potentially overfit with a double-Gaussian profile and thus no strong non-gravitational outflow component is present.

The final sample includes 63 objects with strong non-gravitational kinematics in the [O III]λ5007 emission line, of which 55 outflow components are blueshifted and 8 outflow components are redshifted relative to their core components. The 63 objects with strong outflows are shown in the shaded regions of 4.1 and listed in Table 4.1 with their relevant measurements.

To visualize the diversity of the 63 strong [O III] outflows in our sample, we align their full profiles by shifting them to the rest frame velocity of the core component and normalize them by the amplitude of the full profile, as shown in Figure 4.2, with the luminosity-weighted average shown by the red profile.

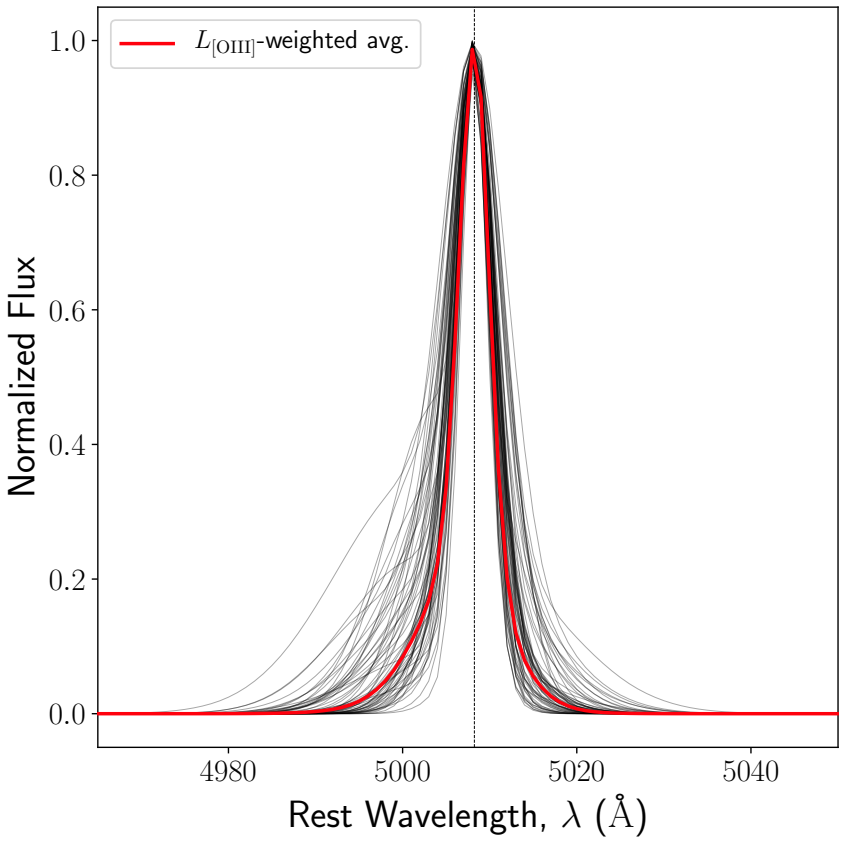

Figure 4.2: Superimposed [O III] profiles of all 63 outflow objects in our sample shown in black. Individual [O III] profiles are aligned at the rest frame velocity of the core component and normalized by the maximum amplitude of the full [O III] profile. The luminosity-weighted average is show by the red profile.

4.3.2 Correcting σ_* for Disk Inclination

The relatively large 3″ diameter SDSS fiber can cover a significant fraction of the host galaxy, introducing contamination from non-bulge components. This is of particular concern for σ_* measurements on the $M_{\rm BH} - \sigma_*$ relation since BH mass does not correlate with the stellar velocity dispersion of disks (see Kormendy & Ho (2013) for a review of all BH mass correlations).

As such, a significant number of objects in our sample contain disks, which at high inclinations, can artificially increase the measured stellar velocity dispersion, and overestimate values by as much as 25% (Hartmann et al., 2014). Using N-body simulations, Bellovary et al. (2014) derived a prescription to correct measured σ_* to face-on ($i = 0$) values using common observables, which depend significantly on the inclination i and rotational velocity $v_{\rm rot}$ of the disk.

To correct the measured velocity dispersions in our sample, we first obtain disk inclinations and disk scale lengths from (Simard et al., 2011), who performed bulge+disk decompositions of over 1.1 million SDSS galaxies, from which we obtain measurements for 57 objects from our sample of 63. We then estimate the disk rotational velocities from scale lengths using the SDSS RV Relation from Hall et al. (2012). The prescription from Bellovary et al. (2014) depends on the ratio $(v/\sigma)_{\rm spec}$), for which we assume a value of 0.6 for a fast-rotating late-type galaxy (Falcón-Barroso et al., 2017) following the same procedure from S19. We note that varying values of $(v/\sigma)_{\rm spec}$) do not significantly change the correction factor as much as values for i and $v_{\rm rot}$. We propagate all uncertainties in quadrature and assume an additional 10% uncertainty in correction prescription. The average change

in σ_* due to this correction for all of our objects is only 12 km s^{-1}, but can be as high as 39 km s^{-1} for the highest of inclinations. We determine that despite this correction, the overall scatter for σ_* in our sample does not change, and that this correction will have a negligible effect on our results.

4.4 Results

The relevant measurements obtained from spectral fitting with BADASS for the 63 objects in our sample are presented in Table 4.1. Calculated AGN luminosities at 5100 Å are obtained via the empirical relation between the luminosity of the broad Hβ emission line and $\lambda L_{5100\text{Å}}$ from Greene & Ho (2005), and $M_{\rm BH}$ is calculated using the relation from S19 based on the mass recalibration from reverberation mapping measurements from Woo et al. (2015). Black hole masses for the 63 outflow objects span nearly three orders of magnitude from ($5.6 \leq \log_{10}(M_{\rm BH}/M_{\odot}) \leq 8.4$). To quantify the maximal velocity of the outflows, we adopt the relation from Harrison et al. (2014) given by

$$v_{\rm max} = \Delta v_0 + \frac{W_{80}}{2} \tag{4.1}$$

where v_0 is the velocity offset of the outflow component measured with respect to the velocity offset of the core component, and $W_{80} = 1.09$ FWHM, which represents the width containing 80% of the Gaussian flux of the outflow component. Values of $v_{\rm max}$ listed in Table 4.1 are negative if the outflow is blueshifted with respect to the core component, and positive if redshifted with respect to the core component. Velocities for the core and outflow components, $v_{\rm core}$ and $v_{\rm outflow}$, are reported as velocities with respect to the systemic (stellar)

velocity. All reported dispersion are corrected for the SDSS redshift-dependent instrumental dispersion during the fitting process by BADASS. The vast majority of our objects ($N = 55$) have blueshifted outflow components with respect to their core component.

We use these measurements to further investigate correlations of outflows with their host galaxy and AGN to understand their relationship, if any. For reference, we plot a heatmap of the Spearman's rank correlation coefficient r_s for all relevant and possibly interesting quantities measured with BADASS in Figure 4.3. We discuss the most notable correlations in detail in the following subsections. In the following figures we adopt a consistent colorscale shown in Figure 4.4, which represents the absolute value of $v_{\rm max}$.

4.4.1 Correlations with Velocity

We first investigate correlations with the velocities of the [O III] core and outflow components. Following Woo et al. (2016), we plot Velocity-Velocity Dispersion (VVD) diagrams of the core and outflow components in Figure 4.4. The Spearman correlation coefficient for the [O III] core VVD diagram is $r_s = -0.19$, indicating no significant correlation, while the [O III] outflow VVD diagram shows stronger correlation of $r_s = -0.36$. The [O III] outflow VVD diagram also exhibits the same "fan" shape characterized by Woo et al. (2016), which according to 3D biconical outflow models (Bae & Woo, 2016), is caused by an increasing extinction due to the presence of an obscuring dust plane. In theory, if there exists a dust plane that bisects a biconical outflow for which one of the cones points toward the observer along the LOS (the blueshifted cone), the dust plane will obscure the cone on the far

Table 4.1: BADASS measurements of relevant quantities for outflow, host galaxy, and AGN properties. Column 1: SDSS object designation. Column 2: reference; (1) B18, (2) W15, (3) S19. Column 3: systemic redshift determined using stellar kinematics. Column 4: stellar velocity dispersion. Column 5: [O III] core component systemic velocity. Column 6: [O III] core component velocity dispersion. Column 7: [O III] core component luminosity. Column 8: [O III] outflow component systemic velocity. Column 9: [O III] outflow component velocity dispersion. Column 10: [O III] outflow component luminosity. Column 11: maximal outflow velocity measured using W_{80}. Column 12: FWHM of the broad Hβ emission line. Column 13: AGN luminosity at 5100 Å measured using the relation from Greene & Ho (2005). Column 14: BH mass estimated using relation from S19. Kinematic quantities measured in units of km s^{-1}. Luminosity meansured in units of erg s^{-1}. Black hole mass measured in units of $M_\odot$.

Object	Ref.	z	σ_*	$v_{\rm core}$	$\sigma_{\rm core}$	$L_{\rm core}$	$v_{\rm outflow}$	$\sigma_{\rm outflow}$	$L_{\rm outflow}$	$v_{\rm max}$	FWHM$_{\rm H\beta}$	$\lambda L_{5100\text{Å}}$	$\log(M_{\rm BH})$
J000338.94+160220.6	3	0.11668	91^{+13}_{-13}	-129^{+11}_{-11}	107^{+4}_{-4}	$41.01^{+0.02}_{-0.02}$	-331^{+24}_{-26}	397^{+21}_{-21}	$40.90^{+0.03}_{-0.03}$	-712^{+35}_{-36}	3513^{+116}_{-114}	$43.38^{+0.01}_{-0.01}$	$7.63^{+0.19}_{-0.13}$
J001335.38-095120.9	1	0.06196	55^{+18}_{-18}	-38^{+14}_{-13}	127^{+11}_{-11}	$40.25^{+0.05}_{-0.05}$	-284^{+45}_{-59}	392^{+40}_{-36}	$40.28^{+0.05}_{-0.06}$	-749^{+64}_{-75}	3587^{+53}_{-50}	$43.34^{+0.01}_{-0.01}$	$7.62^{+0.19}_{-0.13}$
J010939.01+005950.4	1	0.09376	105^{+15}_{-14}	-198^{+11}_{-11}	119^{+3}_{-3}	$41.26^{+0.01}_{-0.01}$	-398^{+16}_{-16}	393^{+13}_{-12}	$41.17^{+0.01}_{-0.01}$	-705^{+20}_{-20}	3279^{+102}_{-96}	$43.23^{+0.02}_{-0.02}$	$7.47^{+0.19}_{-0.12}$
J012159.81-010224.4	1	0.05484	116^{+12}_{-12}	-130^{+12}_{-12}	117^{+3}_{-3}	$41.38^{+0.02}_{-0.02}$	-303^{+12}_{-13}	272^{+3}_{-3}	$41.50^{+0.01}_{-0.02}$	-521^{+7}_{-7}	4210^{+51}_{-47}	$43.53^{+0.00}_{-0.00}$	$7.86^{+0.20}_{-0.13}$
J021257.59+140610.0	1	0.06228	120^{+10}_{-9}	-88^{+5}_{-5}	138^{+3}_{-3}	$40.83^{+0.01}_{-0.02}$	-290^{+25}_{-27}	413^{+35}_{-30}	$40.51^{+0.03}_{-0.03}$	-732^{+46}_{-46}	4221^{+90}_{-89}	$43.14^{+0.01}_{-0.01}$	$7.65^{+0.18}_{-0.13}$
J024912.86-081525.7	2	0.02983	20^{+11}_{-11}	-72^{+5}_{-5}	62^{+4}_{-4}	$39.60^{+0.02}_{-0.02}$	-212^{+22}_{-24}	303^{+23}_{-20}	$39.42^{+0.03}_{-0.03}$	-529^{+34}_{-35}	891^{+38}_{-38}	$41.76^{+0.02}_{-0.03}$	$5.56^{+0.22}_{-0.13}$
J030124.26+011022.8	1	0.07216	94^{+11}_{-11}	-172^{+10}_{-10}	120^{+6}_{-6}	$40.50^{+0.02}_{-0.02}$	-560^{+37}_{-41}	487^{+32}_{-30}	$40.51^{+0.03}_{-0.03}$	-1013^{+53}_{-56}	3263^{+65}_{-66}	$43.22^{+0.02}_{-0.02}$	$7.47^{+0.19}_{-0.13}$
J030144.19+011530.8	1	0.07558	98^{+10}_{-10}	-208^{+8}_{-8}	131^{+5}_{-5}	$40.89^{+0.02}_{-0.02}$	-517^{+16}_{-18}	345^{+8}_{-8}	$41.00^{+0.02}_{-0.02}$	-752^{+19}_{-21}	3622^{+47}_{-45}	$43.42^{+0.01}_{-0.01}$	$7.68^{+0.21}_{-0.14}$
J030417.78+002827.2	2	0.04488	55^{+8}_{-8}	-81^{+5}_{-5}	63^{+4}_{-4}	$40.27^{+0.03}_{-0.03}$	-172^{+10}_{-11}	166^{+6}_{-6}	$40.26^{+0.03}_{-0.03}$	-304^{+12}_{-13}	1505^{+27}_{-27}	$42.80^{+0.01}_{-0.01}$	$6.58^{+0.22}_{-0.14}$
J073106.86+392644.5	2	0.04894	32^{+10}_{-10}	-134^{+6}_{-6}	107^{+3}_{-3}	$40.17^{+0.01}_{-0.01}$	-363^{+10}_{-10}	318^{+5}_{-5}	$40.28^{+0.01}_{-0.01}$	-637^{+11}_{-11}	1492^{+35}_{-34}	$42.38^{+0.01}_{-0.01}$	$6.36^{+0.22}_{-0.14}$
J073505.65+423545.7	3	0.08644	45^{+12}_{-13}	-55^{+7}_{-7}	76^{+6}_{-6}	$40.59^{+0.05}_{-0.05}$	-156^{+11}_{-12}	174^{+7}_{-6}	$40.70^{+0.04}_{-0.04}$	-324^{+13}_{-14}	1712^{+61}_{-60}	$42.85^{+0.02}_{-0.02}$	$6.72^{+0.19}_{-0.13}$
J073703.28+424414.6	1	0.08861	102^{+10}_{-10}	-46^{+8}_{-9}	135^{+3}_{-3}	$41.27^{+0.01}_{-0.02}$	-249^{+23}_{-27}	318^{+24}_{-22}	$40.83^{+0.04}_{-0.04}$	-610^{+36}_{-38}	4004^{+63}_{-65}	$43.33^{+0.01}_{-0.01}$	$7.71^{+0.21}_{-0.14}$
J073714.28+292634.1	2	0.08029	83^{+9}_{-10}	-160^{+10}_{-10}	108^{+9}_{-12}	$40.41^{+0.06}_{-0.07}$	-353^{+69}_{-103}	231^{+41}_{-42}	$40.07^{+0.17}_{-0.15}$	-488^{+88}_{-117}	2395^{+218}_{-189}	$42.62^{+0.05}_{-0.04}$	$6.89^{+0.21}_{-0.15}$
J080243.40+310403.3	1	0.04130	99^{+8}_{-8}	-26^{+6}_{-6}	104^{+3}_{-3}	$40.69^{+0.01}_{-0.02}$	-199^{+36}_{-44}	301^{+48}_{-41}	$40.07^{+0.06}_{-0.06}$	-559^{+64}_{-69}	5511^{+81}_{-80}	$43.22^{+0.01}_{-0.01}$	$7.93^{+0.22}_{-0.14}$
J081718.55+520147.7	2	0.03911	42^{+12}_{-13}	-156^{+7}_{-7}	59^{+3}_{-4}	$40.20^{+0.02}_{-0.02}$	-101^{+25}_{-20}	205^{+28}_{-24}	$39.63^{+0.09}_{-0.07}$	318^{+39}_{-36}	1941^{+58}_{-55}	$42.39^{+0.01}_{-0.01}$	$6.59^{+0.19}_{-0.14}$
J082912.68+500652.3	2	0.04373	75^{+8}_{-7}	-56^{+6}_{-6}	77^{+1}_{-1}	$40.79^{+0.00}_{-0.00}$	-225^{+10}_{-10}	358^{+10}_{-9}	$40.38^{+0.01}_{-0.01}$	-627^{+14}_{-14}	1017^{+23}_{-22}	$42.54^{+0.01}_{-0.01}$	$6.10^{+0.22}_{-0.14}$
J085504.16+525248.3	2	0.08994	76^{+9}_{-9}	-171^{+15}_{-13}	206^{+18}_{-22}	$40.60^{+0.07}_{-0.09}$	-309^{+32}_{-42}	522^{+80}_{-68}	$40.60^{+0.08}_{-0.07}$	-808^{+94}_{-98}	2092^{+104}_{-93}	$42.96^{+0.02}_{-0.02}$	$6.95^{+0.22}_{-0.14}$
J090902.35+133019.4	1	0.05005	88^{+10}_{-10}	-69^{+10}_{-10}	92^{+15}_{-13}	$39.72^{+0.10}_{-0.07}$	4^{+24}_{-19}	249^{+27}_{-19}	$39.89^{+0.05}_{-0.07}$	392^{+34}_{-31}	3524^{+147}_{-134}	$42.49^{+0.02}_{-0.02}$	$7.15^{+0.20}_{-0.13}$
J092343.00+225432.7	1	0.03357	137^{+7}_{-6}	-157^{+8}_{-8}	146^{+3}_{-3}	$41.16^{+0.01}_{-0.01}$	-233^{+8}_{-8}	417^{+7}_{-6}	$41.37^{+0.01}_{-0.01}$	-612^{+9}_{-9}	3598^{+26}_{-26}	$43.69^{+0.00}_{-0.00}$	$7.81^{+0.21}_{-0.14}$
J093259.60+040506.0	1	0.05990	103^{+4}_{-5}	-133^{+5}_{-5}	89^{+4}_{-4}	$40.43^{+0.03}_{-0.03}$	-282^{+20}_{-25}	235^{+22}_{-20}	$40.20^{+0.05}_{-0.05}$	-450^{+33}_{-36}	4829^{+214}_{-194}	$42.74^{+0.02}_{-0.02}$	$7.56^{+0.22}_{-0.14}$
J094057.19+032401.2	2	0.06122	63^{+12}_{-12}	-134^{+9}_{-9}	90^{+9}_{-9}	$40.39^{+0.04}_{-0.04}$	-291^{+32}_{-38}	335^{+32}_{-28}	$40.34^{+0.05}_{-0.05}$	-587^{+48}_{-52}	1577^{+101}_{-99}	$42.69^{+0.02}_{-0.02}$	$6.56^{+0.22}_{-0.14}$
J094529.36+093610.4	2	0.01394	80^{+6}_{-6}	-167^{+4}_{-4}	114^{+2}_{-2}	$40.15^{+0.01}_{-0.01}$	-247^{+6}_{-6}	300^{+7}_{-7}	$39.95^{+0.02}_{-0.02}$	-465^{+10}_{-10}	2084^{+51}_{-50}	$41.95^{+0.01}_{-0.02}$	$6.41^{+0.22}_{-0.15}$
J094838.43+403043.5	1	0.04771	92^{+11}_{-11}	-176^{+7}_{-7}	103^{+2}_{-3}	$40.78^{+0.01}_{-0.01}$	-304^{+40}_{-49}	457^{+63}_{-56}	$40.12^{+0.05}_{-0.05}$	-714^{+82}_{-86}	3374^{+66}_{-64}	$43.07^{+0.01}_{-0.01}$	$7.43^{+0.18}_{-0.14}$
J104925.39+245123.7	1	0.05543	105^{+11}_{-11}	-81^{+8}_{-8}	98^{+2}_{-2}	$41.15^{+0.01}_{-0.01}$	-166^{+13}_{-13}	281^{+15}_{-13}	$40.72^{+0.03}_{-0.03}$	-445^{+19}_{-20}	5072^{+47}_{-45}	$43.48^{+0.00}_{-0.00}$	$8.00^{+0.20}_{-0.14}$
J110016.03+461615.2	2	0.03257	63^{+5}_{-5}	-156^{+4}_{-4}	79^{+3}_{-3}	$40.30^{+0.02}_{-0.02}$	-256^{+7}_{-8}	213^{+6}_{-5}	$40.23^{+0.02}_{-0.02}$	-374^{+9}_{-10}	1433^{+53}_{-52}	$42.17^{+0.02}_{-0.02}$	$6.20^{+0.21}_{-0.14}$
J110101.78+110248.8	1	0.03596	104^{+9}_{-9}	-69^{+6}_{-6}	115^{+3}_{-3}	$40.93^{+0.01}_{-0.01}$	-24^{+7}_{-8}	320^{+9}_{-9}	$40.80^{+0.02}_{-0.02}$	455^{+12}_{-12}	6092^{+80}_{-82}	$43.13^{+0.01}_{-0.01}$	$7.97^{+0.20}_{-0.14}$
J110456.03+433409.1	1	0.04952	70^{+7}_{-7}	-40^{+5}_{-5}	71^{+4}_{-4}	$40.57^{+0.02}_{-0.02}$	44^{+12}_{-10}	218^{+13}_{-12}	$40.34^{+0.04}_{-0.04}$	363^{+19}_{-19}	4031^{+253}_{-237}	$42.46^{+0.04}_{-0.03}$	$7.25^{+0.23}_{-0.14}$
J112526.51+022039.0	2	0.04897	76^{+11}_{-11}	-57^{+7}_{-7}	75^{+5}_{-5}	$40.31^{+0.03}_{-0.04}$	-99^{+18}_{-22}	229^{+29}_{-24}	$39.97^{+0.07}_{-0.07}$	-336^{+35}_{-38}	1618^{+121}_{-116}	$42.31^{+0.03}_{-0.03}$	$6.38^{+0.23}_{-0.15}$
J114545.18+554759.6	1	0.05419	96^{+12}_{-12}	-159^{+8}_{-9}	79^{+11}_{-11}	$40.18^{+0.08}_{-0.07}$	-122^{+13}_{-12}	248^{+28}_{-22}	$40.30^{+0.05}_{-0.05}$	356^{+30}_{-30}	3765^{+168}_{-160}	$42.67^{+0.03}_{-0.03}$	$7.31^{+0.19}_{-0.14}$

Table 4.1: *Continued*

Object	Ref.	z	σ_*	$v_{\rm core}$	$\sigma_{\rm core}$	$L_{\rm core}$	$v_{\rm outflow}$	$\sigma_{\rm outflow}$	$L_{\rm outflow}$	$v_{\rm max}$	FWHM$_{\rm H\beta}$	$\lambda L_{5100\text{Å}}$	$\log(M_{\rm BH})$
J115333.22+095408.4	2	0.06965	99^{+9}_{-9}	-134^{+7}_{-7}	123^{+2}_{-3}	$41.19^{+0.01}_{-0.01}$	-260^{+16}_{-18}	345^{+19}_{-18}	$40.74^{+0.03}_{-0.03}$	-569^{+27}_{-29}	1937^{+69}_{-66}	$42.90^{+0.02}_{-0.02}$	$6.86^{+0.19}_{-0.13}$
J120556.01+495956.4	1	0.06376	120^{+8}_{-7}	-170^{+6}_{-6}	148^{+2}_{-2}	$41.67^{+0.01}_{-0.01}$	-208^{+9}_{-9}	390^{+18}_{-17}	$41.05^{+0.03}_{-0.03}$	-539^{+22}_{-22}	7451^{+177}_{-166}	$43.28^{+0.01}_{-0.01}$	$8.24^{+0.19}_{-0.13}$
J120626.29+424426.1	1	0.05234	119^{+8}_{-8}	-100^{+7}_{-7}	110^{+4}_{-4}	$40.47^{+0.01}_{-0.01}$	-290^{+42}_{-45}	544^{+65}_{-57}	$40.14^{+0.03}_{-0.04}$	-889^{+84}_{-86}	3819^{+62}_{-58}	$43.12^{+0.01}_{-0.01}$	$7.57^{+0.17}_{-0.14}$
J121044.27+382010.3	1	0.02319	97^{+7}_{-6}	-75^{+6}_{-6}	103^{+4}_{-4}	$40.70^{+0.02}_{-0.02}$	-63^{+8}_{-8}	266^{+13}_{-12}	$40.52^{+0.03}_{-0.03}$	354^{+17}_{-17}	6302^{+108}_{-98}	$43.03^{+0.01}_{-0.01}$	$7.96^{+0.18}_{-0.14}$
J123152.04+450442.9	1	0.06276	140^{+11}_{-11}	-195^{+12}_{-11}	208^{+8}_{-9}	$40.71^{+0.03}_{-0.04}$	-749^{+118}_{-117}	442^{+72}_{-76}	$40.29^{+0.11}_{-0.09}$	-1121^{+153}_{-152}	2708^{+90}_{-83}	$42.89^{+0.02}_{-0.02}$	$7.14^{+0.18}_{-0.14}$
J123228.08+141558.7	3	0.42747	90^{+39}_{-38}	-183^{+28}_{-27}	154^{+7}_{-7}	$41.97^{+0.03}_{-0.03}$	-225^{+32}_{-31}	484^{+34}_{-30}	$41.95^{+0.03}_{-0.03}$	-663^{+42}_{-42}	5760^{+301}_{-281}	$44.01^{+0.02}_{-0.02}$	$8.39^{+0.18}_{-0.13}$
J123455.90+153356.2	3	0.04625	98^{+7}_{-7}	-47^{+6}_{-6}	90^{+2}_{-2}	$40.83^{+0.01}_{-0.01}$	-240^{+14}_{-15}	235^{+9}_{-9}	$40.51^{+0.03}_{-0.02}$	-494^{+17}_{-18}	2514^{+55}_{-53}	$42.88^{+0.02}_{-0.02}$	$7.07^{+0.19}_{-0.14}$
J123651.17+453904.1	2	0.03079	98^{+6}_{-6}	-130^{+5}_{-6}	65^{+3}_{-3}	$40.12^{+0.02}_{-0.01}$	-186^{+6}_{-6}	339^{+5}_{-5}	$40.55^{+0.01}_{-0.01}$	-491^{+7}_{-7}	1964^{+47}_{-46}	$42.50^{+0.01}_{-0.01}$	$6.66^{+0.17}_{-0.14}$
J123932.59+342221.3	2	0.08516	78^{+8}_{-8}	-184^{+7}_{-7}	70^{+7}_{-6}	$40.27^{+0.03}_{-0.03}$	-450^{+16}_{-19}	321^{+12}_{-12}	$40.68^{+0.02}_{-0.02}$	-678^{+22}_{-24}	2198^{+120}_{-114}	$42.85^{+0.04}_{-0.04}$	$6.94^{+0.18}_{-0.14}$
J124035.82-002919.4	2	0.08154	94^{+19}_{-18}	-133^{+15}_{-15}	76^{+2}_{-2}	$41.28^{+0.01}_{-0.01}$	-171^{+16}_{-16}	251^{+8}_{-8}	$41.03^{+0.02}_{-0.02}$	-360^{+11}_{-11}	1553^{+69}_{-66}	$42.81^{+0.02}_{-0.02}$	$6.62^{+0.20}_{-0.13}$
J124129.42+372201.9	1	0.06363	119^{+12}_{-12}	-41^{+7}_{-7}	116^{+3}_{-3}	$41.13^{+0.01}_{-0.01}$	-169^{+23}_{-25}	390^{+30}_{-28}	$40.66^{+0.03}_{-0.03}$	-629^{+42}_{-43}	4412^{+94}_{-90}	$43.22^{+0.01}_{-0.01}$	$7.74^{+0.19}_{-0.13}$
J132310.39+270140.4	1	0.05618	70^{+10}_{-10}	-13^{+6}_{-6}	91^{+6}_{-6}	$40.40^{+0.04}_{-0.04}$	-54^{+8}_{-8}	251^{+11}_{-10}	$40.54^{+0.03}_{-0.03}$	-362^{+15}_{-15}	4176^{+217}_{-198}	$42.59^{+0.02}_{-0.02}$	$7.34^{+0.21}_{-0.13}$
J135345.93+395101.6	1	0.06330	134^{+6}_{-6}	-117^{+6}_{-6}	126^{+5}_{-6}	$40.57^{+0.02}_{-0.03}$	-240^{+27}_{-33}	466^{+73}_{-64}	$40.30^{+0.04}_{-0.04}$	-721^{+86}_{-88}	6036^{+334}_{-318}	$42.78^{+0.03}_{-0.03}$	$7.78^{+0.20}_{-0.13}$
J140514.86-025901.2	1	0.05460	107^{+12}_{-12}	-67^{+8}_{-8}	116^{+9}_{-9}	$40.31^{+0.04}_{-0.05}$	-175^{+26}_{-34}	320^{+28}_{-25}	$40.20^{+0.06}_{-0.06}$	-519^{+41}_{-47}	3689^{+100}_{-98}	$42.95^{+0.01}_{-0.01}$	$7.44^{+0.18}_{-0.13}$
J141630.82+013707.9	1	0.05436	115^{+9}_{-9}	-137^{+7}_{-7}	145^{+8}_{-8}	$40.45^{+0.04}_{-0.04}$	-231^{+15}_{-17}	411^{+24}_{-21}	$40.55^{+0.03}_{-0.03}$	-620^{+31}_{-32}	3667^{+173}_{-156}	$42.66^{+0.03}_{-0.03}$	$7.28^{+0.19}_{-0.14}$
J141908.30+075449.6	1	0.05634	168^{+10}_{-10}	-6^{+7}_{-7}	195^{+3}_{-4}	$41.18^{+0.01}_{-0.01}$	-329^{+27}_{-34}	449^{+16}_{-16}	$40.80^{+0.03}_{-0.03}$	-898^{+33}_{-39}	6065^{+299}_{-294}	$42.92^{+0.02}_{-0.02}$	$7.86^{+0.19}_{-0.14}$
J143452.45+483942.8	1	0.03669	110^{+9}_{-9}	-54^{+7}_{-7}	108^{+2}_{-2}	$40.99^{+0.01}_{-0.01}$	53^{+20}_{-18}	336^{+26}_{-23}	$40.40^{+0.04}_{-0.04}$	538^{+35}_{-34}	4855^{+44}_{-47}	$43.40^{+0.00}_{-0.00}$	$7.93^{+0.16}_{-0.14}$
J152209.56+451124.0	2	0.06593	95^{+11}_{-11}	-58^{+10}_{-11}	167^{+18}_{-22}	$40.42^{+0.09}_{-0.11}$	-92^{+29}_{-56}	418^{+99}_{-71}	$40.27^{+0.14}_{-0.11}$	-570^{+96}_{-107}	2083^{+102}_{-90}	$42.66^{+0.03}_{-0.03}$	$6.79^{+0.19}_{-0.13}$
J152324.42+551855.3	2	0.03987	86^{+11}_{-10}	-217^{+6}_{-6}	86^{+5}_{-5}	$40.12^{+0.03}_{-0.03}$	-435^{+43}_{-63}	234^{+23}_{-31}	$39.66^{+0.08}_{-0.10}$	-519^{+59}_{-75}	2459^{+158}_{-143}	$42.15^{+0.03}_{-0.03}$	$6.66^{+0.21}_{-0.13}$
J152940.58+302909.3	2	0.03641	93^{+5}_{-5}	-98^{+6}_{-6}	97^{+4}_{-5}	$40.48^{+0.03}_{-0.03}$	-231^{+23}_{-31}	228^{+22}_{-20}	$40.15^{+0.07}_{-0.06}$	-426^{+35}_{-40}	2412^{+40}_{-40}	$42.98^{+0.01}_{-0.01}$	$7.08^{+0.18}_{-0.13}$
J153552.40+575409.3	1	0.03077	128^{+13}_{-12}	-93^{+10}_{-10}	130^{+2}_{-2}	$41.44^{+0.01}_{-0.01}$	-171^{+12}_{-13}	273^{+10}_{-9}	$41.01^{+0.04}_{-0.04}$	-429^{+14}_{-14}	4447^{+38}_{-39}	$43.57^{+0.00}_{-0.00}$	$7.93^{+0.18}_{-0.13}$
J154351.49+363136.7	1	0.06794	78^{+9}_{-9}	-163^{+6}_{-7}	108^{+3}_{-3}	$41.27^{+0.02}_{-0.02}$	-323^{+10}_{-10}	267^{+6}_{-6}	$41.18^{+0.02}_{-0.02}$	-502^{+12}_{-12}	2898^{+44}_{-44}	$43.39^{+0.01}_{-0.01}$	$7.46^{+0.19}_{-0.13}$
J154507.53+170951.1	1	0.04837	119^{+10}_{-9}	8^{+6}_{-6}	103^{+1}_{-1}	$41.12^{+0.01}_{-0.01}$	-119^{+9}_{-9}	311^{+8}_{-8}	$40.72^{+0.01}_{-0.01}$	-527^{+12}_{-12}	5501^{+112}_{-115}	$42.99^{+0.01}_{-0.01}$	$7.80^{+0.18}_{-0.13}$
J160746.00+345048.9	2	0.05478	86^{+8}_{-8}	-200^{+7}_{-8}	108^{+4}_{-4}	$40.61^{+0.02}_{-0.02}$	-411^{+11}_{-11}	424^{+9}_{-8}	$40.84^{+0.01}_{-0.01}$	-755^{+14}_{-14}	1651^{+47}_{-44}	$42.75^{+0.01}_{-0.01}$	$6.63^{+0.18}_{-0.13}$
J161156.30+521116.8	1	0.04149	108^{+7}_{-7}	-44^{+6}_{-6}	131^{+4}_{-4}	$40.50^{+0.02}_{-0.02}$	-368^{+29}_{-31}	426^{+21}_{-21}	$40.33^{+0.03}_{-0.03}$	-870^{+39}_{-41}	3727^{+141}_{-135}	$42.72^{+0.02}_{-0.02}$	$7.33^{+0.19}_{-0.13}$
J163159.59+243740.2	2	0.04384	72^{+6}_{-6}	-58^{+6}_{-6}	94^{+2}_{-2}	$40.65^{+0.01}_{-0.01}$	-207^{+21}_{-24}	278^{+16}_{-16}	$39.97^{+0.04}_{-0.04}$	-506^{+28}_{-31}	1065^{+48}_{-44}	$42.37^{+0.02}_{-0.02}$	$6.07^{+0.18}_{-0.14}$
J163501.46+305412.1	2	0.05460	95^{+15}_{-14}	-108^{+9}_{-9}	122^{+6}_{-6}	$40.79^{+0.03}_{-0.02}$	-223^{+11}_{-12}	393^{+13}_{-11}	$40.97^{+0.01}_{-0.02}$	-620^{+17}_{-17}	2333^{+120}_{-110}	$42.73^{+0.02}_{-0.02}$	$6.94^{+0.18}_{-0.14}$
J170859.15+215308.1	1	0.07277	123^{+12}_{-12}	-85^{+9}_{-9}	164^{+4}_{-4}	$40.94^{+0.01}_{-0.01}$	2^{+15}_{-15}	551^{+24}_{-22}	$40.86^{+0.02}_{-0.02}$	795^{+31}_{-31}	6325^{+122}_{-115}	$43.37^{+0.01}_{-0.01}$	$8.13^{+0.18}_{-0.13}$
J172759.14+542147.0	2	0.09989	40^{+19}_{-16}	-89^{+12}_{-13}	73^{+3}_{-3}	$40.80^{+0.02}_{-0.02}$	-185^{+29}_{-34}	241^{+36}_{-31}	$40.26^{+0.07}_{-0.06}$	-406^{+47}_{-51}	1295^{+78}_{-78}	$42.66^{+0.02}_{-0.02}$	$6.38^{+0.20}_{-0.13}$
J205822.14-065004.3	2	0.07413	35^{+13}_{-13}	-59^{+8}_{-8}	96^{+2}_{-2}	$41.05^{+0.01}_{-0.01}$	-225^{+12}_{-13}	287^{+8}_{-8}	$40.78^{+0.02}_{-0.02}$	-533^{+14}_{-14}	1302^{+32}_{-32}	$42.87^{+0.01}_{-0.01}$	$6.48^{+0.19}_{-0.13}$
J210226.54+000702.3	2	0.05222	73^{+9}_{-8}	-92^{+8}_{-9}	77^{+7}_{-8}	$39.93^{+0.05}_{-0.05}$	-275^{+39}_{-49}	199^{+31}_{-28}	$39.73^{+0.09}_{-0.09}$	-438^{+53}_{-60}	1984^{+129}_{-116}	$42.19^{+0.03}_{-0.03}$	$6.50^{+0.20}_{-0.14}$
J222246.61-081943.9	1	0.08312	111^{+8}_{-8}	-222^{+7}_{-7}	172^{+4}_{-4}	$41.16^{+0.01}_{-0.01}$	-599^{+13}_{-13}	570^{+8}_{-8}	$41.35^{+0.01}_{-0.01}$	-1109^{+15}_{-16}	3933^{+110}_{-105}	$43.27^{+0.01}_{-0.01}$	$7.67^{+0.18}_{-0.13}$
J223338.42+131243.5	1	0.09438	123^{+16}_{-15}	-203^{+10}_{-9}	150^{+4}_{-4}	$41.40^{+0.02}_{-0.02}$	-258^{+12}_{-13}	483^{+20}_{-20}	$41.29^{+0.02}_{-0.02}$	-675^{+28}_{-28}	4326^{+55}_{-51}	$43.66^{+0.00}_{-0.00}$	$7.96^{+0.19}_{-0.13}$
J235128.75+155259.1	1	0.09675	136^{+12}_{-11}	-23^{+8}_{-9}	98^{+4}_{-4}	$41.21^{+0.01}_{-0.01}$	-135^{+8}_{-8}	249^{+2}_{-2}	$41.55^{+0.00}_{-0.00}$	-431^{+4}_{-4}	7236^{+180}_{-175}	$43.43^{+0.01}_{-0.01}$	$8.28^{+0.19}_{-0.13}$

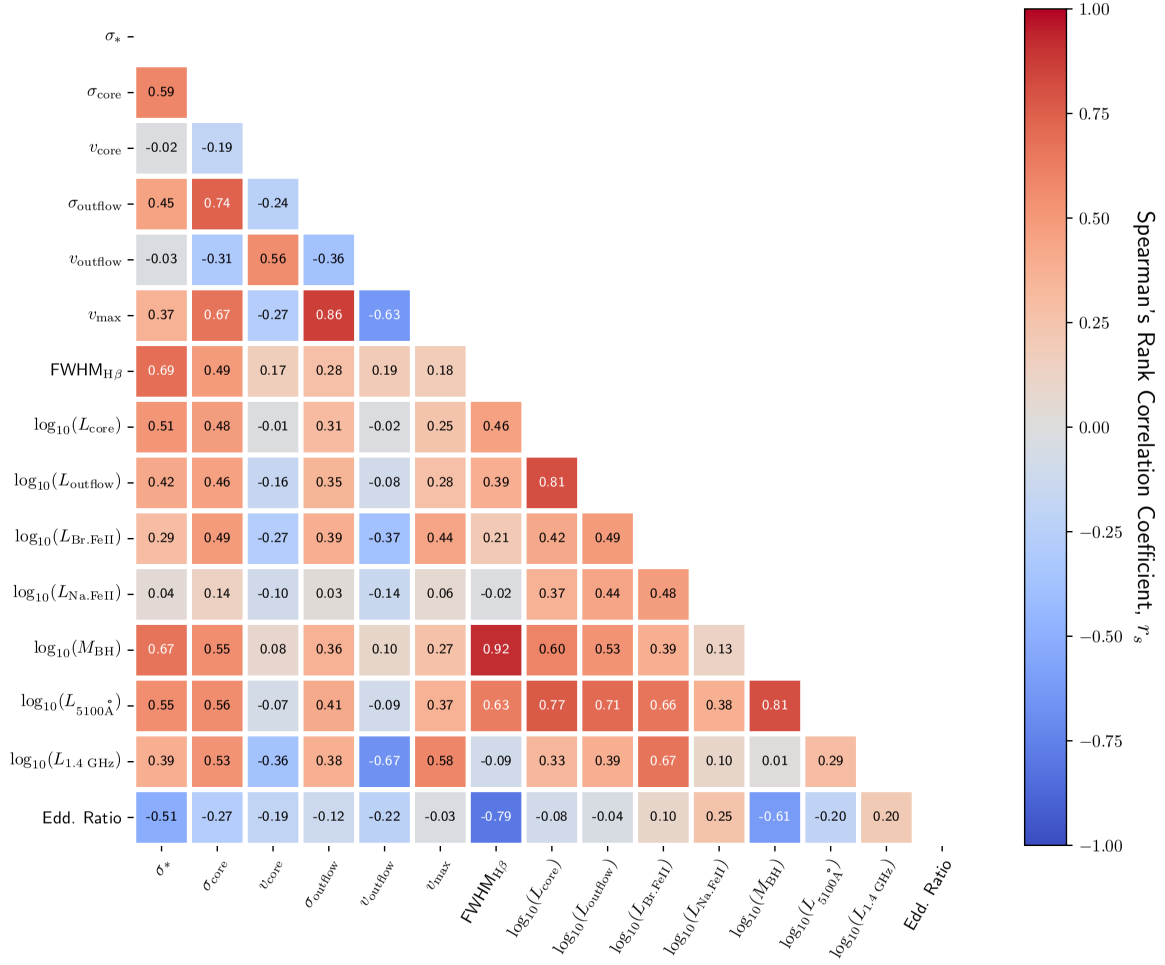

Figure 4.3: Correlation matrix of relevant quantities measured with BADASS. The colorscale represents the absolute Spearman's rank correlation coefficient r_s. The average uncertainty for all calculated values of r_s is 0.04.

side (the redshifted cone) causing an observed blueshifted flux excess. The fan-shaped VVD diagram for outflows does not appear to extend to the core component. We also confirm the result from Rakshit & Woo (2018) that blueshifted outflows are significantly more common than redshifted outflows for type 1 AGN.

There does appear to be strong correlation ($r_s = 0.56$) between $v_{\rm core}$ and $v_{\rm outflow}$ measured with respect to the systemic (stellar) velocity, as shown in Figure 4.5, which shows $v_{\rm core}$ scales linearly with $v_{\rm outflow}$. Our data suggest that for blueshifted outflows (right of the dashed line in Figure 4.5) there is an average offset of 120 km s^{-1} between the core and outflow components, and there appears to be an increasing offset from $v_{\rm core}$ with $v_{\rm max}$. A larger sample with $v_{\rm max} > 900$ km s^{-1} and objects with redshifted outflows is needed to conclusively determine whether this trend holds, or if there is a value of $v_{\rm max}$ for which this trend no longer holds true.

4.4.2 Correlations with Dispersion

In Figure 4.6, we plot the single-Gaussian "no-outflow" model [O III] dispersion $\sigma_{\rm single}$ alongside the double-Gaussian "outflow" model core dispersion $\sigma_{\rm core}$, both as a function of σ_*. We confirm the results from Bennert et al. (2018) that $\sigma_{\rm core}$ correlates more strongly with σ_* once the secondary outflow component is accounted for. Values of $\sigma_{\rm core}$ are scattered about the perfect correlation with σ_*, with a root-mean-square error (RMSE) of 27 ± 2 km s^{-1}. The mean of this distribution of $\sigma_{\rm core}$ values is 18 ± 2 km s^{-1}, caused primarily by objects with $v_{\rm max} > 700$ km s^{-1}.

In Figure 4.7 we plot the difference ($\sigma_{\rm core} - \sigma_*$) as a function of $\sigma_{\rm outflow}$ and find

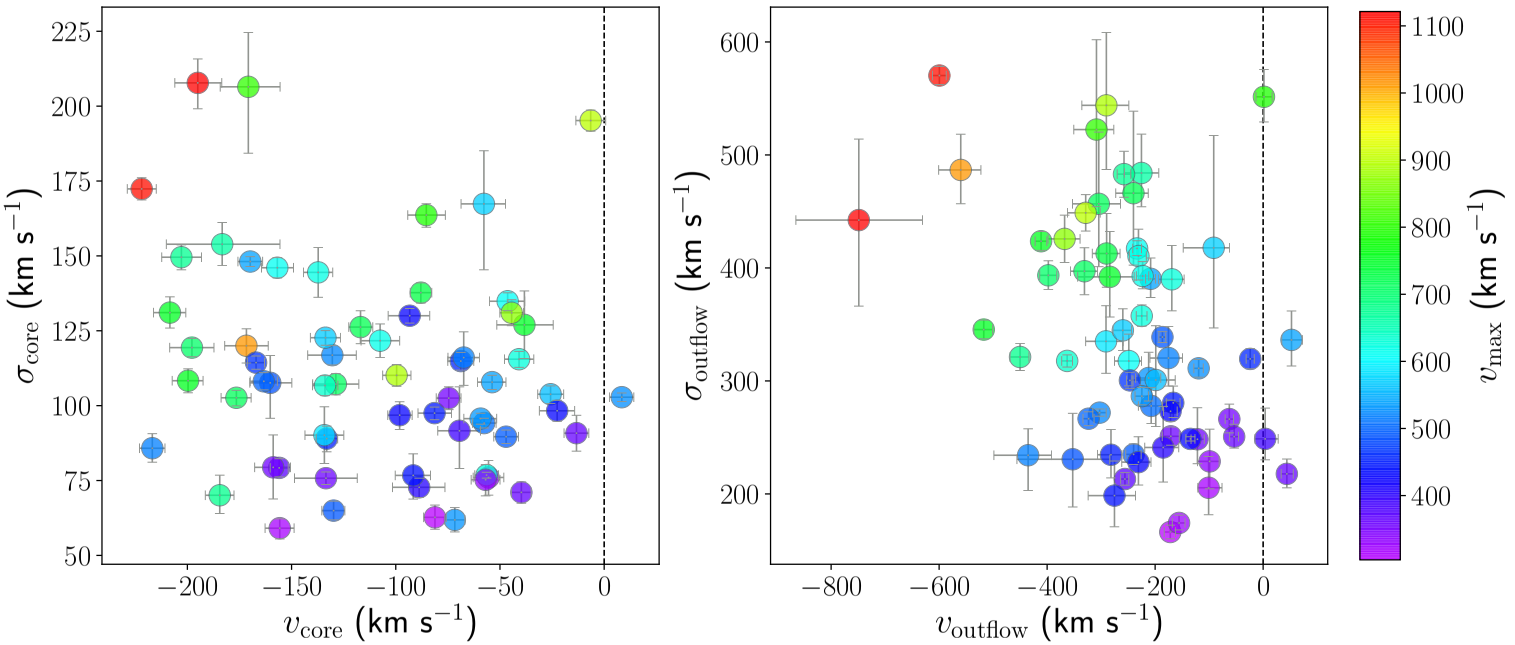

Figure 4.4: VVD diagrams for the [O III] core and outflow components. The black dashed line indicates zero velocity offset with respect to the systemic (stellar) velocity. (*Left*): There is no correlation between $\sigma_{\rm core}$ and $v_{\rm core}$, however the majority of velocities are blueshifted with respect to the systemic velocity. (*Right*): There is a significant correlation between $\sigma_{\rm outflow}$ and $v_{\rm outflow}$, characterized by the distinct "fan" shape described by Woo et al. (2016), caused by increasing extinction with increasing outflow velocity.

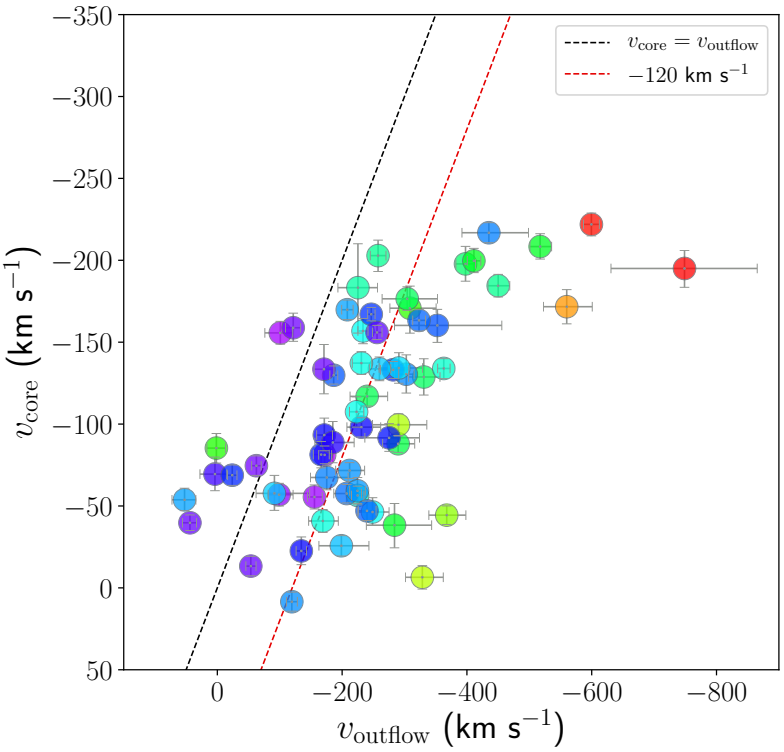

Figure 4.5: The strong correlation between $v_{\rm core}$ and $v_{\rm outflow}$ measured with respect to the systemic (stellar) velocity. The black dashed line indicates the perfect correlation $v_{\rm core} = v_{\rm outflow}$, and the red dashed line indicates an average -120 km s^{-1} offset from the perfect correlation for blueshifted outflows. Objects with larger $v_{\rm max}$ appear to deviate from this correlation, however a larger sample of objects with $v_{\rm max} > 900$ km s^{-1} is needed to conclusively determine if the correlation holes true, and likewise for redshifted outflows.

that there is some dependence on how well $\sigma_{\rm core}$ can recover the gravitational component σ_* as a function of $\sigma_{\rm outflow}$ and $v_{\rm max}$, however a larger sample will also be needed to confirm this trend.

There also exists a strong correlation between the [O III] core component dispersion $\sigma_{\rm core}$ and the outflow component dispersion $\sigma_{\rm outflow}$ as first reported by Zhang & Feng (2017), which we plot in Figure 4.8 for our sample. This correlation has so far been largely overlooked, mostly due to the parameterization other studies have used to quantify outflows. For instance, Woo et al. (2016) performed double-Gaussian decomposition of the [O III], but did not study individual dispersions and instead adopted a flux-weighted integrated dispersion for the full line (core+outflow) profile. The Spearman rank correlation coefficient for this relation is $r_s = 0.74$, implying a very strong correlation, and stronger than the $\sigma_{\rm core} - \sigma_*$ correlation ($r_s = 0.59$). We perform linear regression using *emcee* following the same methods used in S19, and determine a best-fit slope of $m = 0.26 \pm 0.03$, intercept of $b = 25.00^{+9.05}_{-8.89}$ km s^{-1}, and intrinsic scatter of $f = 19.11^{+2.16}_{-2.08}$, which we plot in Figure 4.8.

It is important to emphasize that the $\sigma_{\rm core} - \sigma_{\rm outflow}$ correlation is not a result of our definition of an "outflow" or our selection criteria for outflows given in Section 3.2.2.2. Although we define an outflow to have $\sigma_{\rm outflow} > \sigma_{\rm core}$, which excludes objects above the dashed line ($\sigma_{\rm core} = \sigma_{\rm outflow}$) in Figure 4.8 by design, this does not explain the tightness in the correlation below the dashed line. The outflow criterion for dispersion given in Section 3.2.2.2 also does not select objects based on the ratio of $\sigma_{\rm outflow}$ and $\sigma_{\rm core}$, but by the ratio of the difference of $\sigma_{\rm outflow}$ and $\sigma_{\rm core}$ and their relative uncertainties. Recall that 90% of the objects with outflows were first identified visually from their strong asymmetric profile,

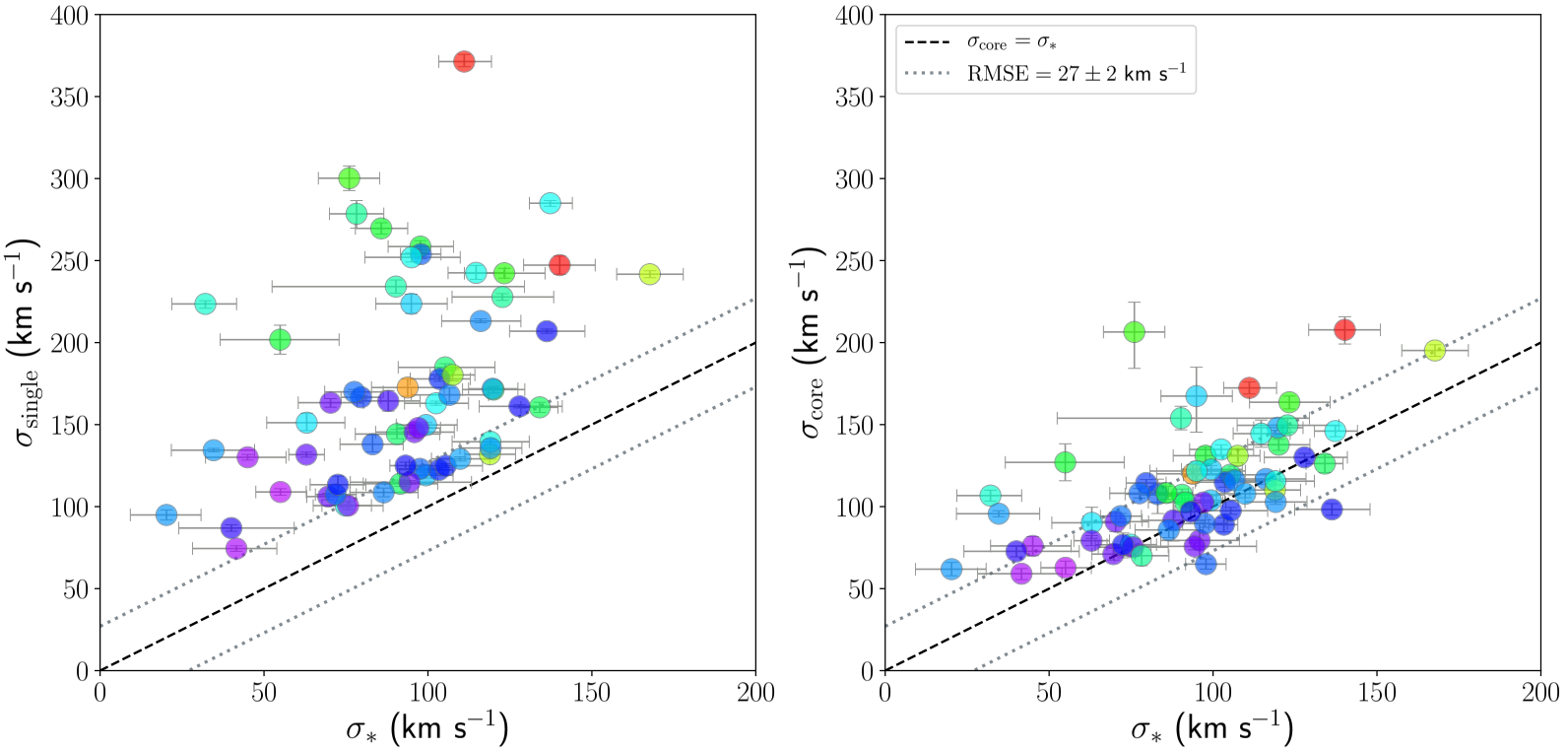

Figure 4.6: (*Left*): The single gaussian no-outflow model [O III] dispersion $\sigma_{\rm single}$ as a function of stellar velocity dispersion σ_*. There is a clear offset in objects which exhibit strong outflows with large $v_{\rm max}$. (*Right*): The double-Gaussian outflow model [O III] dispersion as a function of σ_*. The gray dotted lines in both plots give the scatter of the $\sigma_{\rm core} - \sigma_*$ relation for comparison. The colorscale is the same as in Figure 4.4. The black dashed line represents perfect correlation, i.e., $\sigma_{\rm core} = \sigma_*$.

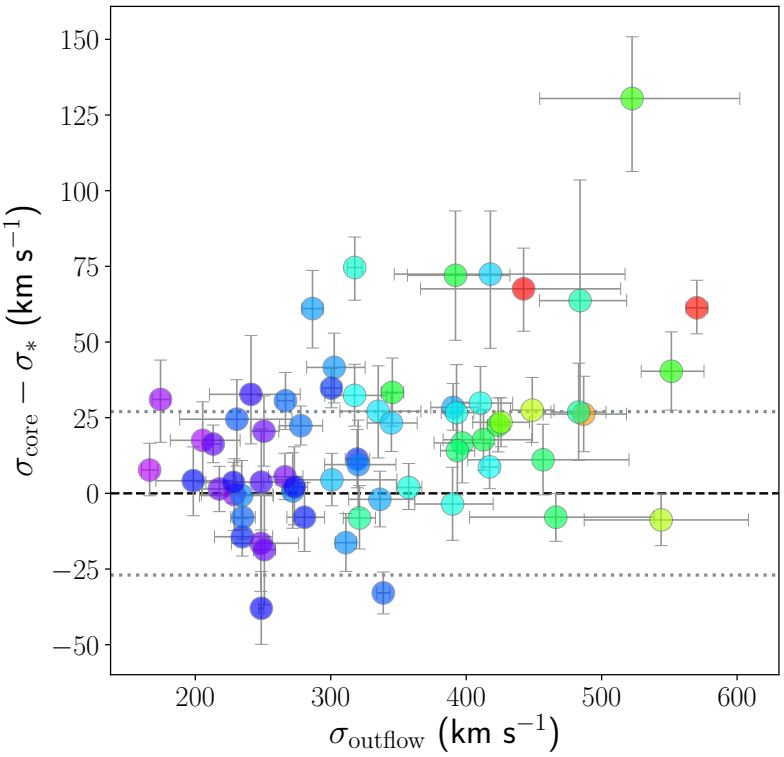

Figure 4.7: The difference between the decomposed $\sigma_{\rm core}$ and σ_* as a function of $\sigma_{\rm outflow}$. There is a clear dependence on how well $\sigma_{\rm core}$ traces the gravitational component σ_*, which appears to scale with $\sigma_{\rm outflow}$.

implying that we are not overfitting [O III] profiles which do not require double-Gaussian decomposition. We therefore are confident that the $\sigma_{\rm core} - \sigma_{\rm outflow}$ correlation is real and not an artifact of the fitting process.

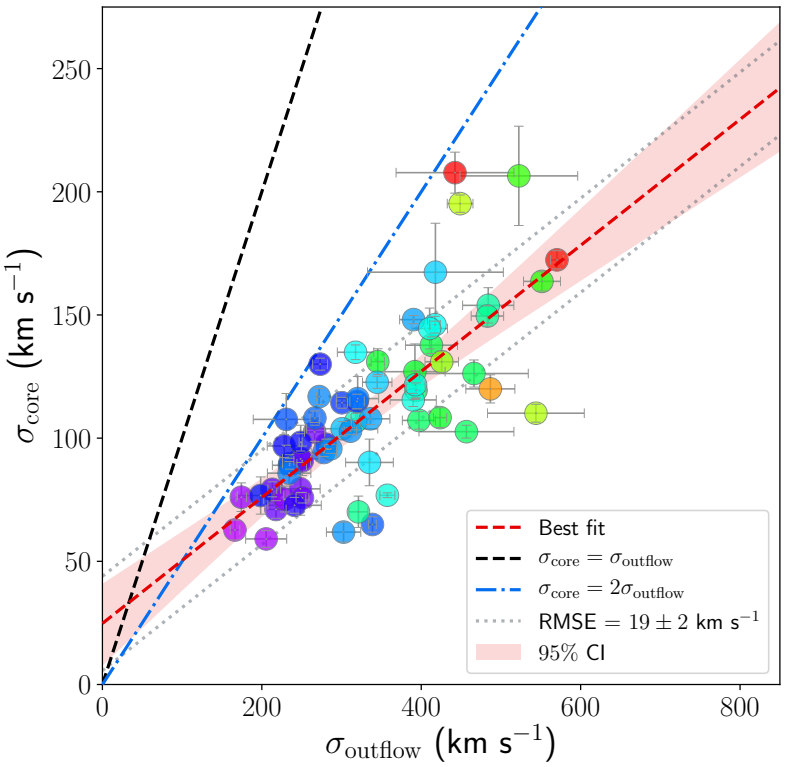

Figure 4.8: The correlation between $\sigma_{\rm core}$ and $\sigma_{\rm outflow}$. The best-fit regression line is given by the red dashed line, and the shaded red region corresponds to 95% confidence interval. The gray dotted lines correspond to the scatter in the relation. The identity correlation ($\sigma_{\rm core} = \sigma_{\rm outflow}$) is shown by the black dashed line, and the $\sigma_{\rm core} = 2\sigma_{\rm outflow}$ relation is shown by the blue dashed-dotted line for comparison.

4.4.3 Correlations with Luminosity

There is strong correlation between the AGN luminosity at 5100 Å ($L_{5100\ \text{Å}}$) and $L_{\rm core}$ ($r_s = 0.77$), and a slightly weaker correlation for $L_{\rm outflow}$ ($r_s = 0.71$), although the weaker correlation with $L_{\rm outflow}$ is likely due to larger uncertainties. Because we are esti-

mating $L_{5100\text{Å}}$ using the luminosity of the broad Hβ emission line (Greene & Ho, 2005), correlations with $L_{5100\text{Å}}$ presented here are comparable to correlations with M_{BH}, which is estimated using both the luminosity and width of the broad Hβ emission line. However, the correlation between $L_{5100\ \text{Å}}$ and outflow kinematics are comparatively weaker.

To investigate correlations with the radio luminosity at 1.4 GHz, we obtain $L_{1.4\ \text{GHz}}$ measurements from the VLA First Survey Catalog (White et al., 1997), which covers 10,575 square degrees of sky for a total of 946,432 radio sources, from which 18 of our 63 outflow objects have measurements. Referring to Figure 4.3, the correlations between $L_{1.4\ \text{GHz}}$ and σ_{core} and σ_{outflow} are comparable to their correlations with $L_{5100\ \text{Å}}$. However, when compared to systemic velocities, there is much stronger correlation between $L_{1.4\ \text{GHz}}$ and v_{outflow} ($r_s = -0.67$) than for v_{core} ($r_s = -0.36$). In Figure 4.9, we plot $L_{1.4\ \text{GHz}}$ as a function of v_{core} and v_{outflow}.

The only other notable correlations found between luminosities are those with the luminosity of the broad Fe II. Both $L_{5100\text{Å}}$ and $L_{1.4\ \text{GHz}}$ correlate strongly with $L_{\text{Br.FeII}}$, and with nearly identical degrees of correlation of $r_s \sim 0.67$.

4.4.4 The $M_{\text{BH}} - \sigma_*$ Relation

The ultimate goal of our analysis is to determine the effect - if any - of outflow kinematics on the $M_{\text{BH}} - \sigma_*$ relation. In Figure 4.10 we plot the $M_{\text{BH}} - \sigma$ relation using both σ_* and σ_{core}, and plot the local relation derived from S19 (black dashed line) and the 0.43 dex scatter (orange dotted line) for comparison.

There is considerable scatter in the $M_{\text{BH}} - \sigma_*$ relation (left of Figure 4.10) for our

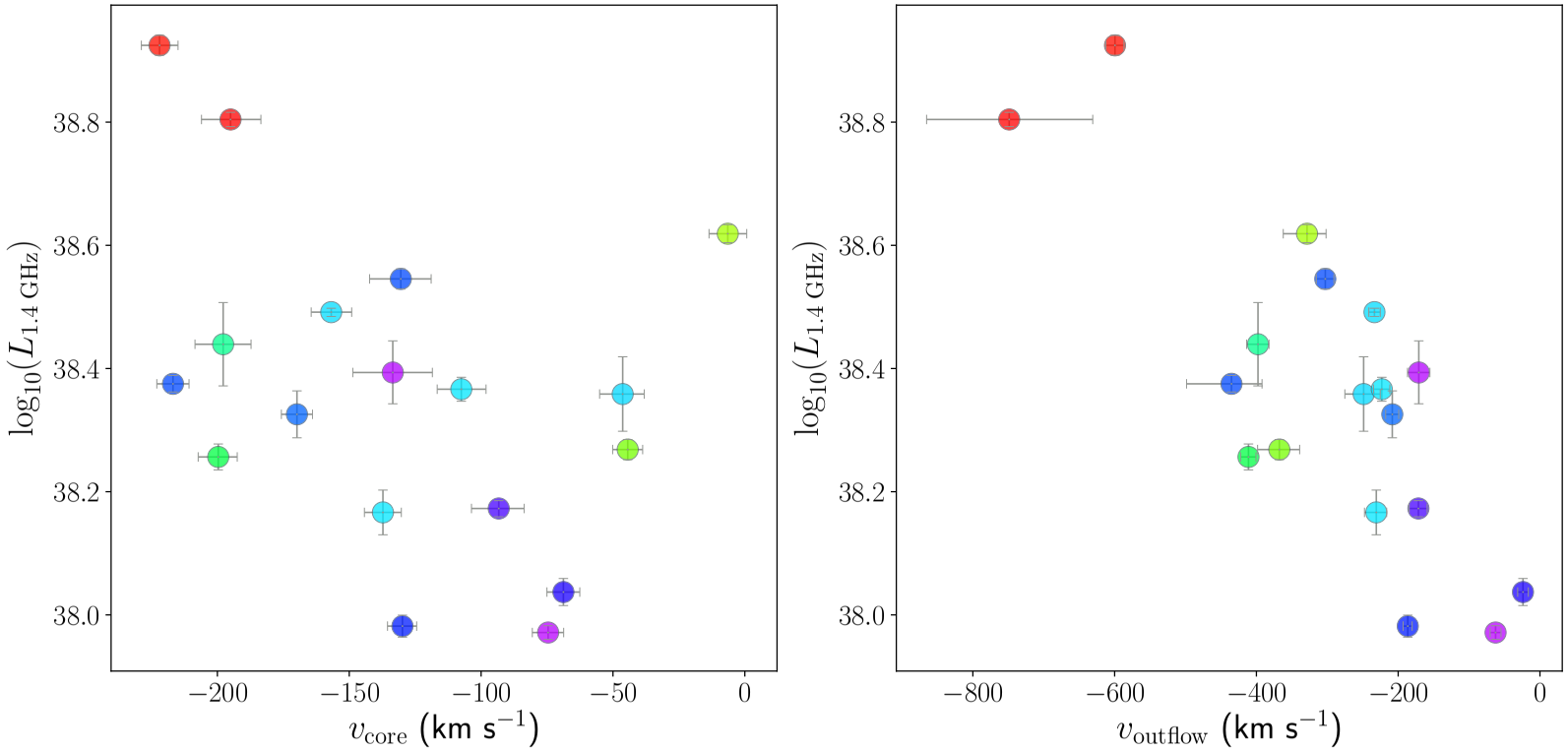

Figure 4.9: Correlations of $L_{1.4\,\mathrm{GHz}}$ versus v_{core} (left) and v_{outflow} (right) for 18 objects with available measurements. The correlation correlation with $\sigma_{\mathrm{outflow}}$ ($r_s = -0.67$) is nearly twice that of the correlation with v_{core}.

objects, however the majority of our sample falls within or close to the expected scatter of the relation, with the exception of some outliers above the relation by as much as ~ 1 dex. The total scatter about the relation for our objects is 0.6 dex. There are considerable uncertainties we cannot account for given the nature of SDSS data that may affect our measurements of σ_*. Despite our efforts to correct for the effects of inclination, it is possible that the bulge+disk decomposition performed by Simard et al. (2011) resulted in a poor match to the image PSF, since the decompositions do not take into account the point-spread function (PSF) of the AGN, which would in turn affect measured disk quantities such as ellipticity (b/a) and inclination. As mentioned in Section 4.3.2, the $3''$ diameter SDSS fiber can cover a significant fraction of the host galaxy to include contamination from non-bulge components, which can bias measurements of σ_*, but also decrease the fraction of light from the AGN. If the fraction of light from the AGN decreased due to significant host galaxy absorption, we would underestimate the amplitude and therefore overestimate the FWHM of the broad Hβ emission line, leading to an overestimation of $M_{\rm BH}$. Dependencies on AGN continuum dilution also play a role in how well σ_* can be recovered from absorption features, as we showed in Figure 3.11. It remains that measurements σ_* are one of the most uncertain measurements in BH scaling relations, due to both data limitations and poorly understood systematics.

Since we are interested in using $\sigma_{\rm core}$ as a surrogate for σ_* on the $M_{\rm BH}-\sigma_*$ relation, we plot $M_{\rm BH}-\sigma_{\rm core}$ on the right in Figure 4.10. We find that the scatter of the $M_{\rm BH}-\sigma_*$ relation is 0.54 dex, slightly less than that of the $M_{\rm BH}-\sigma_{\rm core}$ relation with a scatter of 0.57 dex. However, the mean of $M_{\rm BH}-\sigma_*$ relation is 0.57 dex above the local relation, driven

by clear outliers between 1-2 dex above the local relation. The mean of the $M_{\rm BH} - \sigma_{\rm core}$ is 0.17 and more-evenly distributed about the local relation.

It is clear from Figure 4.10 that the scatter in $M_{\rm BH} - \sigma_{\rm core}$ is due primarily to stratification in $\sigma_{\rm core}$, with $\sigma_{\rm core} < 600$ km s^{-1} primarily above the relation, and $\sigma_{\rm core} > 900$ km s^{-1} below the relation. It is possible that this separation in dispersion across the local relation could be attributed to the core broadening as a function of $v_{\rm max}$ we see in Figure 4.7. It is also worthy to note that this stratification in σ_* is not as obvious in the $M_{\rm BH} - \sigma_*$ relation, although there is similar trend for $\sigma_* < 600$ km s^{-1}.

4.5 Discussion

In the following sections we discuss the different correlations and their possible interpretation. We emphasize that although we can only speculate on the physical interpretation of these correlations, these observations represent observational constraints that should be considered when developing models that describe AGN-driven outflows.

4.5.1 Correlations with Velocity

The differences in the VVD diagrams shown in Figure 4.4 indicate that the core and outflow components of the NLR are kinematically distinct. According 3D biconical outflow modelling from Bae & Woo (2016), the fan-shaped distribution of the $\sigma_{\rm outflow} - v_{\rm outflow}$ relation is due to a number of factors, the most important of which are bicone inclination, ejection velocity, and dust extinction along the line of sight. For a symmetric biconical outflow in the absence of any dust extinction, we would expect to measure zero velocity

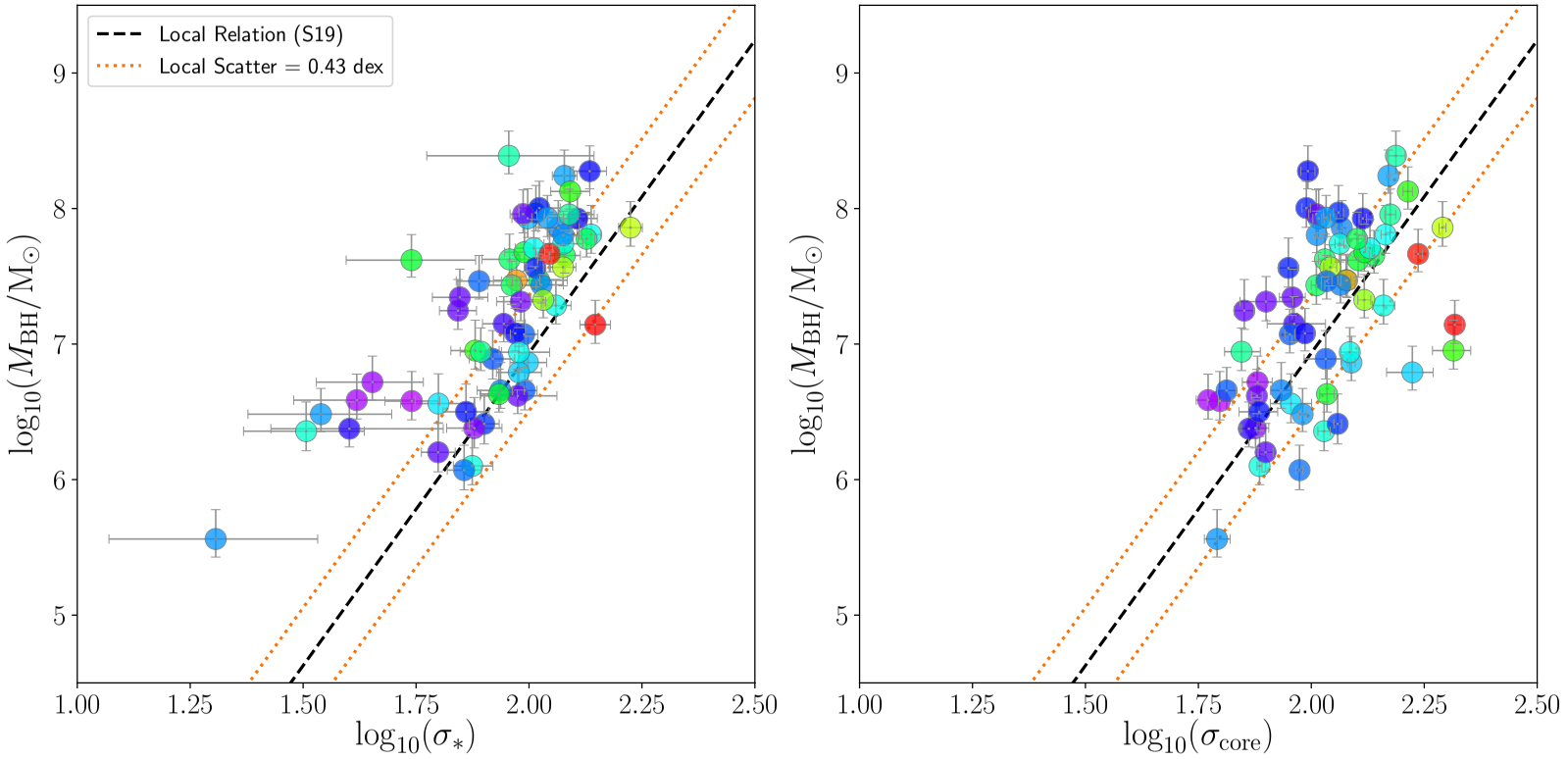

Figure 4.10: The $M_{\rm BH} - \sigma$ relation as a function of σ_* (left) and $\sigma_{\rm core}$ (right). We plot the local relation calculated from S19 (black dashed line) as well as the local scatter (orange dotted lines) for comparison. The majority of objects on the $M_{\rm BH} - \sigma_*$ relation agree with the local relation with some scatter ($f = 0.54$ dex), but the mean of the distribution is 0.57 dex above the local relation, caused by significant outliers likely due to poorly understood systematics and data quality. The $M_{\rm BH} - \sigma_{\rm core}$ relation also agrees with the local relation, with a comparable amount of scatter ($f = 0.58$ dex), mostly caused by stratification in $\sigma_{\rm core}$, and a mean of only 0.17 dex above the local relation.

offset along line of sight due to the cancelling of velocities in opposite directions. With the addition of extinction effects, the obscuration of one side of the bicone would lead to a shift in observed velocity offset. The large number of blueshifted outflows in our sample can be explained as varying obscuration of the receding (redshifted) cone. One interpretation of the strong correlation in the outflow VVD diagram is evidence of collimation, that is, we expect to see an increase in $\sigma_{\rm outflow}$ with an increase in $v_{\rm outlfow}$ along the line of sight if the flow subtends relatively small solid angle (such as a cone) and has a preferred inclination. For example, we expect to see larger velocities as well as a larger velocity dispersion for a flow that is directed along the LOS, as opposed to a flow directed at some angle with respect to the LOS, which would produce a smaller observed velocity and thus smaller dispersion. This interpretation is consistent with the model grids for 3D biconical outflow models from Bae & Woo (2016).

We do not observe the same strong correlation for the $\sigma_{\rm core} - v_{\rm core}$ VVD relation. There is an overall blueshift of $v_{\rm core}$ which correlates with $v_{\rm outflow}$, as shown in Figure 4.5, however there is a larger spread in $v_{\rm core}$ for a given value of $\sigma_{\rm core}$. Given our above argument for the outflow component, the lack of correlation for the core component would imply that the source of the core gas emission is less collimated and more spherically symmetric. This would agree with the interpretation that the core component represents the original NLR gas that is still strongly coupled to the gravitational potential. The core VVD diagram clearly does not exhibit the same kinematic properties of outflows, and should be treated as separate kinematic component when trying to model outflows in AGN.

The linear increase between $v_{\rm core}$ and $v_{\rm outflow}$ and constant 120 km s^{-1} offset in

velocity shown in Figure 4.5 could indicate that the two components are locked in velocity, at least up to a certain value of $v_{\rm max}$. We can only speculate the physical interpretation of this trend, but it could mean that the core NLR gas can be coupled to the outflowing gas below a certain velocity threshold, causing it to become entrained and expand with the outflow. At the highest velocities, the core gas may decouple from the outflowing gas, causing this trend to plateau as shown in Figure 4.5. We would require a larger sample of objects with outflows with $v_{\rm max} > 900$ km s^{-1} to determine if this occurs.

4.5.2 Correlations with Dispersion

In an idealized gravitationally bound system, such as in an undisturbed NLR, we should expect the gas and stellar components to have similar velocity distributions. If a secondary component in the same region as the source of NLR emission is present, and exhibits some collimation (increase in velocity and velocity dispersion), we would expect a distribution similar to that shown on the left of Figure 4.6. We do recover the core NLR gas within some scatter about the perfect correlation with σ_* after correction, as shown on the right in Figure 4.6. Objects with $v_{\rm max} < 600$ km s^{-1} are more evenly distributed about the perfect correlation with σ_* after correcting for $\sigma_{\rm outflow}$. The majority of objects with $v_{\rm max} > 600$ km s^{-1} tend to fall above with the relation even after correcting for $\sigma_{\rm outflow}$, which may indicate that the presence of outflows may introduce additional non-gravitational broadening which may only be detected for the strongest cases. Some scatter is expected, as we cannot fully account for all non-gravitational interactions nor fully account for systematics involving the measurements of σ_* given the nature of SDSS data, such as inclination, aperture effects, or merger history. This correlation is enough to suggest that the core component of the

[O III] profile traces the original NLR gas that is dominated by the gravitational potential of the stellar component.

It is not unreasonable to suggest that if a secondary outflowing component arises from within the NLR, it must start out with the same velocity distribution as the core components. If that velocity distribution then undergoes some interaction, we expect the original distribution to broaden. We can interpret the $\sigma_{\rm core} - \sigma_{\rm outflow}$ correlation shown in Figure 4.8 to be the broadening of the original NLR core gas due to the outflowing gas. What is still puzzling is the linear rate at which the outflow dispersion grows with the core dispersion and its small scatter. We can interpret this as the outflow component having a strong dependence on the original NLR gas from which it is believe to have originated, and the strong linear dependence describes the manner by which the flow propagates through the ambient medium. Another possible interpretation is that the strength of the outflow component (parameterized by $v_{\rm max}$) causes a broadening of the core component, such that $\sigma_{\rm core}$ approaches its respective value of σ_*. There is some correlation shown in Figure 4.7 that suggests that the core component broadens as a function of $\sigma_{\rm outflow}$ (and therefore $v_{\rm max}$), however a larger sample of objects with $v_{\rm max} > 900$ is needed to determine if this trend is real or simply increased scatter.

The $\sigma_{\rm core} - \sigma_*$ and $\sigma_{\rm core} - \sigma_{\rm outflow}$ imply that there is some connection between σ_* and $\sigma_{\rm outflow}$. Ideally, if there is a constant linear relationship between $\sigma_{\rm core}$ and $\sigma_{\rm outflow}$, and if $\sigma_{\rm core}$ traces σ_*, then $\sigma_{\rm outflow}$ should also scale with σ_* but positively offset by some constant. We can fit the interdependence of the three dispersions as a plane of the form

$$a \log_{10}(\sigma_*) + b \log_{10}(\sigma_{\rm core}) + c \log_{10}(\sigma_{\rm outflow}) + d = 0 \tag{4.2}$$

We perform orthogonal regression using *emcee* following the methods of S19 and obtain best fit coefficients of $a = -2.39^{+0.54}_{-0.51}$, $b = 10.26^{+1.00}_{-1.19}$, and $c = -7.91^{+1.12}_{-0.96}$, $d = 3.63^{+1.46}_{-1.60}$, and a scatter about the best fit plane of $f = 0.10$ dex. We plot the projections of the three dispersions, and the projection along the parallel axis of the plane in Figure 4.11. Despite the decreased scatter, there is still a large uncertainty in a, i.e., the slope of the $\sigma_{\rm outflow} - \sigma_*$ relation, which is caused by large scatter. Further study with a larger sample is needed to better constrain this slope before the functional form of 4.2 can be used to calculate σ_* using both $\sigma_{\rm core}$ and $\sigma_{\rm outflow}$.

The physical interpretation of the plane relationship between the three dispersions does not necessarily imply that $\sigma_{\rm outflow}$ can somehow influence σ_* or vice versa, neither does it answer the proverbial "chicken or egg" problem, that is, we do not know if outflows are the causal explanation for the broadening of $\sigma_{\rm core}$ or if $\sigma_{\rm outflow}$ correlates with $\sigma_{\rm core}$ because it originated from an already-broad gas velocity distribution. A larger sample, along with integral field spectroscopy, to determine if these relationships hold true.

4.5.3 Correlations with Luminosity

It has been known for some time that the incidence of [O III] outflows correlates with radio emission in both type 1 and type 2 AGN (Wilson & Willis, 1980; Whittle, 1985; Whittle et al., 1988; Nelson & Whittle, 1996). More recent studies suggest that the strongest correlation with luminosity is between the [O III] width and the radio luminosity at 1.4 GHz ($L_{1.4\,\rm GHz}$), especially in objects with high-velocity outflows and at much higher redshifts. (Mullaney et al., 2013; Zakamska & Greene, 2014; Zakamska et al., 2016; Hwang et al., 2018;

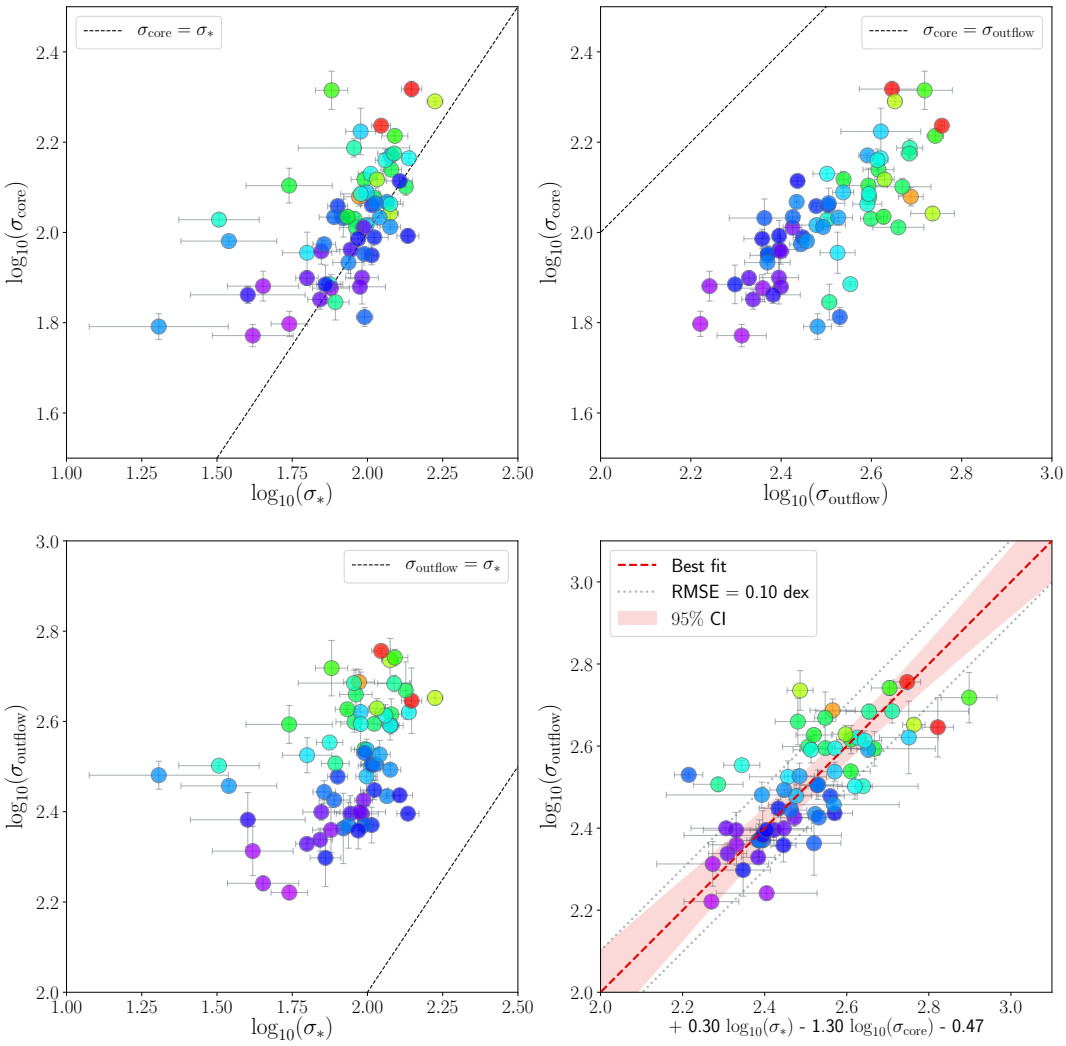

Figure 4.11: The three projections of the $\sigma_{\rm outflow} - \sigma_{\rm core} - \sigma_*$ relation, and the best fit relation projected parallel to the best fit plane. The identity correlations are given by the black dashed line in each plot. The scatter about the best fit plane relation is $f = 0.10$, which is considerably smaller than the scatter in the $\sigma_{\rm core} - \sigma_*$ ($f = 0.17$ dex) and $\sigma_{\rm outflow} - \sigma_*$ ($f = 0.19$ dex) relations, and comparable to the $\sigma_{\rm core} - \sigma_{\rm outflow}$ relation ($f = 0.09$ dex).

Perrotta et al., 2019).

As mentioned in Section 4.4.3, the strong correlation between the core and outflow components, $L_{\rm core}$ and $L_{\rm outflow}$, and the optical AGN luminosity $L_{5100\text{Å}}$ is not surprising if the core and outflow components originate in close proximity to the ionizing source. There is still some correlation with core and outflow dispersion, but even lesser so for the core and outflow velocities. We see similar lack of correlation when we compare $\sigma_{\rm core}$ and $v_{\rm core}$ to $L_{1.4\,\rm GHz}$. By far, the strongest correlation we find between any measured luminosities and kinematics is with $L_{1.4\,\rm GHz}$ and $v_{\rm outflow}$.

Previous studies by Woo et al. (2016) and Rakshit & Woo (2018) used a total (core+outflow) integrated [O III] velocity dispersion parameterization and normalized it by the stellar velocity dispersion to quantify non-gravitational kinematics to compare to radio luminosity, finding no strong correlations with radio activity. In this study, the outflow component is designated as the only non-gravitational component, for which we do find strong correlation with radio luminosity, although with a much smaller sample size. Our findings agree with Mullaney et al. (2013), who similarly found strong correlation between objects with high $L_{1.4\,\rm GHz}$ and objects with the broadest [O III] profiles.

4.5.4 The $M_{\rm BH} - \sigma_*$ Relation

Figure 4.10 shows that when corrected for the outflow component, $\sigma_{\rm core}$ can be used as a surrogate for σ_* on the $M_{\rm BH}-\sigma_*$ relation with comparable scatter, and agree with the results found by Bennert et al. (2018). However, if we are to use $\sigma_{\rm core}$ for studies on the non-local $M_{\rm BH}-\sigma_*$,

we do not have the luxury of comparing it σ_* to ensure we have evidence of non-gravitational kinematics as we have done in our sample. Performing a double-Gaussian decomposition of the [O III] profile when there is no evidence of an additional non-gravitational component, while always producing a better fit, can cause one to measure a smaller $\sigma_{\rm core}$ than what σ_* suggests, which can give the impression that one is measuring BHs that are overmassive relative to the local $M_{\rm BH} - \sigma_*$ relation.

We advise that if $\sigma_{\rm core}$ is used as a surrogate for σ_*, that one always fit a double-Gaussian component and check that the object falls within the acceptable scatter of the $\sigma_{\rm core} - \sigma_{\rm outflow}$ relation. Furthermore, for $\sigma_{\rm outflow} < 200$ km s^{-1}, the scatter of the $\sigma_{\rm core} - \sigma_{\rm outflow}$ relation begins to intersect with that of the $\sigma_{\rm outflow} - \sigma_*$ relation, and it becomes increasingly unclear if there are additional non-gravitational kinematics present in the [O III] profile with respect to σ_*. Therefore, we recommend that for $\sigma_{\rm outflow} < 200$ km s^{-1} one does *not* use a double-Gaussian decomposition for the risk of severely overfitting the [O III] profile and significantly underestimating σ_*. Likewise, if a single-Gaussian fit to the [O III] profile exceeds ~ 200 km s^{-1}, it is recommended to perform a double-Gaussian decomposition and assess the quality of the fit. In this regard, the outflow confidence calculated by BADASS by performing an F-statistic model comparison makes it clear when a double-Gaussian fit is warranted by the data.

4.6 Summary

As an application of BADASS, we fit a sample of 63 SDSS type 1 AGN with strong evidence of outflows in the [O III]λ5007 emission line with BADASS and performed

a correlation analysis of kinematics to determine the relationships between outflows, the AGN, and the host galaxy, expanding upon previous similar studies. We summarize our most important results below:

- By performing a double-Gaussian decomposition of the [O III]λ5007 emission line profile into separate core and outflow components, we find that the core dispersion of the [O III] profile ($\sigma_{\rm core}$) is a suitable surrogate for stellar velocity dispersion (σ_*) in a statistical context but should not be used on an object-to-object basis. There is some evidence that the measured difference $\sigma_{\rm core} - \sigma_*$ scales with increasing outflow component dispersion ($\sigma_{\rm outflow}$), which may imply that there is some broadening of the NLR gas due to the presence of outflows, causing the scatter we see in the $\sigma_{\rm core} - \sigma_*$ relation.

- Velocity-Velocity Dispersion (VVD) digrams of the outflow component resemble the "fan-shaped" VVD profiles exhibited by 3D biconical outflow models from Bae & Woo (2016), indicating possible orientation-dependent or collimated flow. The core component does not exhibit the same VVD shape as the outflow component, indicating that it is a kinematically distinct component of the [O III] gas, more strongly coupled to the gravitational potential.

- There is a systematic broadening of the $\sigma_{\rm core}$ component which scales with $\sigma_{\rm outflow}$, resulting a tight correlation between $\sigma_{\rm core}$ and $\sigma_{\rm outflow}$. This tight correlation implies a very specific relationship between outflow kinematics and the kinematics of the narrow line region, which could be used to constrain theoretical models of AGN outflows.

- We present a new planar relationship between σ_*, $\sigma_{\rm core}$ and $\sigma_{\rm outflow}$ with a scatter about the best-fit plane of 0.10 dex. However, a larger sample is still needed to constrain the relationship between $\sigma_{\rm outflow}$ and σ_* before it can be used to obtain values for σ_*.

- We recover the strong correlation between $L_{1.4\,\rm GHz}$ and properties of outflows found in previous studies. We do not observe strong correlations between outflow kinematics and the optical AGN luminosity $L_{5100\text{Å}}$.

- We find that $\sigma_{\rm core}$ is a suitable surrogate for σ_* on the $M_{\rm BH} - \sigma_*$ relation with comparable scatter in a statistical context in agreement with Bennert et al. (2018). Additionally, we present recommendations and caveats for using $\sigma_{\rm core}$ for studies of the $M_{\rm BH} - \sigma_*$ relation in the non-local universe for which σ_* cannot be measured.

The correlations we have presented here showcase a number of observational constraints that theoretical models of AGN outflows should satisfy. Further investigation into these correlations and their causes will be necessary with larger samples, and we have shown here that BADASS is capable of such detailed analyses.

Chapter 5

Conclusion

To summarize the main results of the previous chapters, we have shown that by using a standardized sample selection criteria, namely the width of the broad Hβ emission feature, we can overcome some of the luminosity-threshold bias seen in high-z studies of the $M_{\rm BH} - \sigma_*$ relation. While our sample is likely still sampling the upper envelope of BH masses at higher-z, we show that NLS1s show some promise in probing lower BH masses in the non-local universe. By comparing NLS1 galaxies in our sample on the Fundamental Plane, we were also able to show that NLS1s do indeed have lower BH masses, and that their narrower broad Hβ widths are likely not a result of broadline region geometry, as some previous studies have implied (Decarli et al., 2008).

To address the challenges associated with probing the $M_{\rm BH} - \sigma_*$ relation in the non-local universe, we introduced BADASS, a new and powerful fitting algorithm for SDSS spectra, which is specifically designed for the careful decomposition of AGN features, including simultaneous fitting of the LOSVD and outflows in narrow forbidden emission line

features. We perform tests on the recovery of σ_*, which show that AGN continuum dilution is mainly responsible for biased measurements of σ_* in Type 1 AGNs, and not necessarily due to the presence of Fe II emission. The BADASS algorithm performs the most-detailed decomposition of optical AGN spectra to date, and is designed for the challenges of future all-sky surveys coming online within the decade.

Finally, we performed spectral decomposition using BADASS on a sample of 63 Type 1 AGNs with evidence of strong outflows, and investigate correlations of the decomposed [O III] core and outflow components independently with properties of AGNs and host galaxies. We confirmed results of previous studies that show that the core [O III] dispersion $\sigma_{\rm core}$ can be used as a surrogate for σ_* in a statistical context once corrected for the presence of strong outflows. Additionally, we show that there may be some broadening of $\sigma_{\rm core}$ that scale with outflow velocity. Known correlations with velocity were recovered, such as the VVD diagrams from Woo et al. (2016), however only for the outflow component of [O III], indicating that the outflow component is a kinematically distinct component of [O III]. We also showed that the outflow velocity is strongly coupled to the radio luminosity at 1.4 GHz, while there is no such correlation for the core velocity of [O III]. We confirmed the results of Bennert et al. (2018) that when correctly accounted for, $\sigma_{\rm core}$ can serve as a suitable substitute for σ_* on the $M_{\rm BH} - \sigma_*$ relation, but only in a statistical context. Finally, we find a strong planar relationship between σ_*, $\sigma_{\rm core}$, and $\sigma_{\rm outflow}$, whose scatter along the fitted plane is ~ 0.1 dex. While these results still require a larger sample size to confirm the significance of the planar relationship, we can speculate that outflows play some role in stellar and gas kinematics. These results provide strong constraints on how we can properly

utilize $\sigma_{\rm core}$ as a surrogate for σ_* on the $M_{\rm BH} - \sigma_*$ relation for higher redshift studies, and the correlations with outflows show enough promise to warrant future studies with a much larger sample in the hopes of further constraining the evolution of the $M_{\rm BH} - \sigma_*$ relation.

Bibliography

Afanasev, V. L., Lipovetskii, V. A., Markarian, B. E., & Stepanian, D. A. 1980, Astrofizika, 16, 193

Astropy Collaboration, Robitaille, T. P., Tollerud, E. J., et al. 2013, A&A, 558, A33, doi: 10.1051/0004-6361/201322068

Bae, H.-J., & Woo, J.-H. 2016, ApJ, 828, 97, doi: 10.3847/0004-637X/828/2/97

Bae, H.-J., Woo, J.-H., Karouzos, M., et al. 2017, ApJ, 837, 91, doi: 10.3847/1538-4357/aa5f5c

Barth, A. J., Pancoast, A., Bennert, V. N., et al. 2013, ApJ, 769, 128, doi: 10.1088/0004-637X/769/2/128

Beifiori, A., Maraston, C., Thomas, D., & Johansson, J. 2011, A&A, 531, A109, doi: 10.1051/0004-6361/201016323

Bellovary, J. M., Holley-Bockelmann, K., Gültekin, K., et al. 2014, MNRAS, 445, 2667, doi: 10.1093/mnras/stu1958

Bennert, V. N., Auger, M. W., Treu, T., Woo, J.-H., & Malkan, M. A. 2011a, ApJ, 726, 59, doi: 10.1088/0004-637X/726/2/59

—. 2011b, ApJ, 742, 107, doi: 10.1088/0004-637X/742/2/107

Bennert, V. N., Treu, T., Auger, M. W., et al. 2015, ApJ, 809, 20, doi: 10.1088/0004-637X/809/1/20

Bennert, V. N., Loveland, D., Donohue, E., et al. 2018, MNRAS, 481, 138, doi: 10.1093/mnras/sty2236

Bentz, M. C., Peterson, B. M., Netzer, H., Pogge, R. W., & Vestergaard, M. 2009, ApJ, 697, 160, doi: 10.1088/0004-637X/697/1/160

Bentz, M. C., Denney, K. D., Grier, C. J., et al. 2013, ApJ, 767, 149, doi: 10.1088/0004-637X/767/2/149

Bertin, E., & Arnouts, S. 1996, A&AS, 117, 393, doi: 10.1051/aas:1996164

Berton, M., Björklund, I., Lähteenmäki, A., et al. 2020, Contributions of the Astronomical Observatory Skalnate Pleso, 50, 270, doi: 10.31577/caosp.2020.50.1.270

Boroson, T. A. 2003, ApJ, 585, 647, doi: 10.1086/346111

Boroson, T. A., & Meyers, K. A. 1992, ApJ, 397, 442, doi: 10.1086/171800

Brotherton, M. S. 1996, The Astrophysical Journal Supplement Series, 102, 1, doi: 10.1086/192249

Calderone, G., Nicastro, L., Ghisellini, G., et al. 2017, MNRAS, 472, 4051, doi: 10.1093/mnras/stx2239

Cales, S. L., Brotherton, M. S., Shang, Z., et al. 2013, ApJ, 762, 90, doi: 10.1088/0004-637X/762/2/90

Canalizo, G., & Stockton, A. 2001, ApJ, 555, 719, doi: 10.1086/321520

Canalizo, G., Wold, M., Hiner, K. D., et al. 2012, ApJ, 760, 38, doi: 10.1088/0004-637X/760/1/38

Cappellari, M. 2017, MNRAS, 466, 798, doi: 10.1093/mnras/stw3020

Cappellari, M., & Emsellem, E. 2004, Publications of the Astronomical Society of the Pacific, 116, 138, doi: 10.1086/381875

Cicone, C., Maiolino, R., & Marconi, A. 2016, A&A, 588, A41, doi: 10.1051/0004-6361/201424514

Cisternas, M., Jahnke, K., Inskip, K. J., et al. 2011, ApJ, 726, 57, doi: 10.1088/0004-637X/726/2/57

Collin, S., Kawaguchi, T., Peterson, B. M., & Vestergaard, M. 2006, A&A, 456, 75, doi: 10.1051/0004-6361:20064878

Costa, T., Pakmor, R., & Springel, V. 2020, arXiv e-prints, arXiv:2006.05997. https://arxiv.org/abs/2006.05997

Croton, D. J. 2006a, MNRAS, 369, 1808, doi: 10.1111/j.1365-2966.2006.10429.x

—. 2006b, MNRAS, 369, 1808, doi: 10.1111/j.1365-2966.2006.10429.x

Croton, D. J., Springel, V., White, S. D. M., et al. 2006, MNRAS, 365, 11, doi: 10.1111/j.1365-2966.2005.09675.x

Davies, R. L., Förster Schreiber, N. M., Übler, H., et al. 2019, ApJ, 873, 122, doi: 10.3847/1538-4357/ab06f1

Davies, R. L., Schreiber, N. M. F., Lutz, D., et al. 2020, ApJ, 894, 28, doi: 10.3847/1538-4357/ab86ad

De Robertis, M. M., & Osterbrock, D. E. 1984, ApJ, 286, 171, doi: 10.1086/162585

Decarli, R., Dotti, M., Fontana, M., & Haardt, F. 2008, MNRAS, 386, L15, doi: 10.1111/j.1745-3933.2008.00451.x

Decarli, R., Dotti, M., Haardt, F., & Zibetti, S. 2011, in Narrow-Line Seyfert 1 Galaxies and their Place in the Universe, 41

DeGraf, C., Di Matteo, T., Treu, T., et al. 2015, MNRAS, 454, 913, doi: 10.1093/mnras/stv2002

Dimitrijević, M. S., Popović, L. Č., Kovačević, J., Dačić, M., & Ilić, D. 2007, MNRAS, 374, 1181, doi: 10.1111/j.1365-2966.2006.11238.x

DiPompeo, M. A., Hickox, R. C., Carroll, C. M., et al. 2018, ApJ, 856, 76, doi: 10.3847/1538-4357/aab365

Djorgovski, S., & Davis, M. 1987, ApJ, 313, 59, doi: 10.1086/164948

Du, P., Lu, K.-X., Zhang, Z.-X., et al. 2016, ApJ, 825, 126, doi: 10.3847/0004-637X/825/2/126

Dubois, Y., Gavazzi, R., Peirani, S., & Silk, J. 2013, MNRAS, 433, 3297, doi: 10.1093/mnras/stt997

Event Horizon Telescope Collaboration, Akiyama, K., Alberdi, A., et al. 2019, ApJL, 875, L1, doi: 10.3847/2041-8213/ab0ec7

Faber, S. M., & Jackson, R. E. 1976, ApJ, 204, 668, doi: 10.1086/154215

Fabian, A. C. 2012, Annual Review of Astronomy and Astrophysics, 50, 455, doi: 10.1146/annurev-astro-081811-125521

Falcón-Barroso, J., Lyubenova, M., van de Ven, G., et al. 2017, A&A, 597, A48, doi: 10.1051/0004-6361/201628625

Ferrarese, L., & Merritt, D. 2000, ApJ, 539, L9, doi: 10.1086/312838

Ferrarese, L., Pogge, R. W., Peterson, B. M., et al. 2001, ApJ, 555, L79, doi: 10.1086/322528

Fisher, D. B., & Drory, N. 2008, in Formation and Evolution of Galaxy Disks, Vol. 396, 309

Foreman-Mackey, D., Hogg, D. W., Lang, D., & Goodman, J. 2013, Publications of the Astronomical Society of the Pacific, 125, 306, doi: 10.1086/670067

Freitas, I. C., Riffel, R. A., Storchi-Bergmann, T., et al. 2018, MNRAS, 476, 2760, doi: 10.1093/mnras/sty303

Gadotti, D. A. 2009, MNRAS, 393, 1531, doi: 10.1111/j.1365-2966.2008.14257.x

Gebhardt, K., Bender, R., Bower, G., et al. 2000a, ApJ, 539, L13, doi: 10.1086/312840

Gebhardt, K., Kormendy, J., Ho, L. C., et al. 2000b, ApJ, 543, L5, doi: 10.1086/318174

Goodrich, R. W. 1989, ApJ, 342, 224, doi: 10.1086/167586

Graham, A. W., Onken, C. A., Athanassoula, E., & Combes, F. 2011, MNRAS, 412, 2211, doi: 10.1111/j.1365-2966.2010.18045.x

Grandi, S. A. 1977, Lick Observatory Bulletin, 754, 1

Greene, J. E. 2012, Nature Communications, 3, 1304, doi: 10.1038/ncomms2314

Greene, J. E., & Ho, L. C. 2005, ApJ, 627, 721, doi: 10.1086/430590

—. 2006a, ApJ, 641, L21, doi: 10.1086/500507

—. 2006b, ApJ, 641, 117, doi: 10.1086/500353

Grupe, D., Beuermann, K., Mannheim, K., & Thomas, H. C. 1999, A&A, 350, 805. https://arxiv.org/abs/astro-ph/9908347

Grupe, D., & Mathur, S. 2004, ApJ, 606, L41, doi: 10.1086/420975

Guo, H., Shen, Y., & Wang, S. 2018, PyQSOFit: Python code to fit the spectrum of quasars, Astrophysics Source Code Library. http://ascl.net/1809.008

Hall, M., Courteau, S., Dutton, A. A., McDonald, M., & Zhu, Y. 2012, MNRAS, 425, 2741, doi: 10.1111/j.1365-2966.2012.21290.x

Hamann, F., Herbst, H., Paris, I., & Capellupo, D. 2019, MNRAS, 483, 1808, doi: 10.1093/mnras/sty2900

Harrison, C. M., Alexander, D. M., Mullaney, J. R., & Swinbank, A. M. 2014, MNRAS, 441, 3306, doi: 10.1093/mnras/stu515

Hartmann, M., Debattista, V. P., Cole, D. R., et al. 2014, MNRAS, 441, 1243, doi: 10.1093/mnras/stu627

Haynes, M. P., & Giovanelli, R. 1984, AJ, 89, 758, doi: 10.1086/113573

Heckman, T. M., Miley, G. K., & Green, R. F. 1984, ApJ, 281, 525, doi: 10.1086/162125

Heckman, T. M., Miley, G. K., van Breugel, W. J. M., & Butcher, H. R. 1980, in Bulletin of the American Astronomical Society, Vol. 12, 809

Hiner, K. D., Canalizo, G., Wold, M., Brotherton, M. S., & Cales, S. L. 2012, ApJ, 756, 162, doi: 10.1088/0004-637X/756/2/162

Hwang, H.-C., Zakamska, N. L., Alexand roff, R. M., et al. 2018, MNRAS, 477, 830, doi: 10.1093/mnras/sty742

Hyde, J. B., & Bernardi, M. 2009, MNRAS, 396, 1171, doi: 10.1111/j.1365-2966.2009.14783.x

Ivezić, Ž., Kahn, S. M., Tyson, J. A., et al. 2019, ApJ, 873, 111, doi: 10.3847/1538-4357/ab042c

Jackson, N., & Browne, I. W. A. 1991, MNRAS, 250, 414, doi: 10.1093/mnras/250.2.414

Jahnke, K., & Macciò, A. V. 2011, ApJ, 734, 92, doi: 10.1088/0004-637X/734/2/92

Jahnke, K., Bongiorno, A., Brusa, M., et al. 2009, ApJ, 706, L215, doi: 10.1088/0004-637X/706/2/L215

Kang, D., & Woo, J.-H. 2018, ApJ, 864, 124, doi: 10.3847/1538-4357/aad561

Kaspi, S., Maoz, D., Netzer, H., et al. 2005, ApJ, 629, 61, doi: 10.1086/431275

Kaspi, S., Smith, P. S., Netzer, H., et al. 2000, ApJ, 533, 631, doi: 10.1086/308704

Kim, D. C., Yoon, I., Privon, G. C., et al. 2017, ApJ, 840, 71, doi: 10.3847/1538-4357/aa6030

King, A., & Pounds, K. 2015, Annual Review of Astronomy and Astrophysics, 53, 115, doi: 10.1146/annurev-astro-082214-122316

Kluyver, T., Ragan-Kelley, B., Pérez, F., et al. 2016, in Positioning and Power in Academic Publishing: Players, Agents and Agendas, ed. F. Loizides & B. Schmidt, IOS Press, 87 – 90

Kollatschny, W., & Zetzl, M. 2011, Nature, 470, 366, doi: 10.1038/nature09761

Komossa, S. 2008b, in Revista Mexicana de Astronomia y Astrofisica Conference Series, Vol. 32, Revista Mexicana de Astronomia y Astrofisica Conference Series, 86–92

Komossa, S., & Xu, D. 2007, ApJ, 667, L33, doi: 10.1086/522002

Komossa, S., Xu, D., Zhou, H., Storchi-Bergmann, T., & Binette, L. 2008a, ApJ, 680, 926, doi: 10.1086/587932

Komossa, S., Xu, D. W., & Wagner, A. Y. 2018, MNRAS, 477, 5115, doi: 10.1093/mnras/sty901

Kormendy, J., & Bender, R. 2013, ApJ, 769, L5, doi: 10.1088/2041-8205/769/1/L5

Kormendy, J., Bender, R., & Cornell, M. E. 2011, Nature, 469, 374, doi: 10.1038/nature09694

Kormendy, J., & Ho, L. C. 2013, Annual Review of Astronomy and Astrophysics, 51, 511, doi: 10.1146/annurev-astro-082708-101811

Kovačević, J., Popović, L. Č., & Dimitrijević, M. S. 2010, ApJS, 189, 15, doi: 10.1088/0067-0049/189/1/15

Kraft, D. 1988, A Software Package for Sequential Quadratic Programming, Deutsche Forschungs- und Versuchsanstalt für Luft- und Raumfahrt Köln: Forschungsbericht (Wiss. Berichtswesen d. DFVLR). https://books.google.com/books?id=4rKaGwAACAAJ

Lauer, T. R., Tremaine, S., Richstone, D., & Faber, S. M. 2007, ApJ, 670, 249, doi: 10.1086/522083

Lazarova, M. S., Canalizo, G., Lacy, M., & Sajina, A. 2012, ApJ, 755, 29, doi: 10.1088/0004-637X/755/1/29

Leighly, K. M. 1999, ApJS, 125, 317, doi: 10.1086/313287

Malkan, M. A. 1983, ApJ, 268, 582, doi: 10.1086/160981

Manzano-King, C. M., Canalizo, G., & Sales, L. V. 2019, ApJ, 884, 54, doi: 10.3847/1538-4357/ab4197

Maraston, C., Strömbäck, G., Thomas, D., Wake, D. A., & Nichol, R. C. 2009, Monthly Notices of the Royal Astronomical Society, 394, L107, doi: 10.1111/j.1745-3933.2009.00621.x

Massey, P., & Gronwall, C. 1990, ApJ, 358, 344, doi: 10.1086/168991

Massey, P., Strobel, K., Barnes, J. V., & Anderson, E. 1988, ApJ, 328, 315, doi: 10.1086/166294

Mathur, S., Kuraszkiewicz, J., & Czerny, B. 2001, NewA, 6, 321, doi: 10.1016/S1384-1076(01)00058-6

Matthews, T. A., & Sandage, A. R. 1963, ApJ, 138, 30, doi: 10.1086/147615

McConnell, N. J., & Ma, C.-P. 2013, ApJ, 764, 184, doi: 10.1088/0004-637X/764/2/184

McIntosh, D. H., Rieke, M. J., Rix, H. W., Foltz, C. B., & Weymann, R. J. 1999, ApJ, 514, 40, doi: 10.1086/306936

McLure, R. J., & Dunlop, J. S. 2004, MNRAS, 352, 1390, doi: 10.1111/j.1365-2966.2004.08034.x

Medling, A. M., U, V., Max, C. E., et al. 2015, ApJ, 803, 61, doi: 10.1088/0004-637X/803/2/61

Melioli, C., & de Gouveia Dal Pino, E. M. 2015, ApJ, 812, 90, doi: 10.1088/0004-637X/812/2/90

Mocz, P., Green, A., Malacari, M., & Glazebrook, K. 2012, in American Astronomical Society Meeting Abstracts #219, Vol. 219, 346.06

Moran, E. C., Halpern, J. P., & Helfand, D. J. 1996, ApJS, 106, 341, doi: 10.1086/192341

Mullaney, J. R., Alexander, D. M., Fine, S., et al. 2013, MNRAS, 433, 622, doi: 10.1093/mnras/stt751

Müller-Sánchez, F., Prieto, M. A., Hicks, E. K. S., et al. 2011, ApJ, 739, 69, doi: 10.1088/0004-637X/739/2/69

Nelson, C. H., & Whittle, M. 1996, ApJ, 465, 96, doi: 10.1086/177405

Oke, J. B., Cohen, J. G., Carr, M., et al. 1995, Publications of the Astronomical Society of the Pacific, 107, 375, doi: 10.1086/133562

Onken, C. A., Ferrarese, L., Merritt, D., et al. 2004, ApJ, 615, 645, doi: 10.1086/424655

Osterbrock, D. E. 1989, Astrophysics of gaseous nebulae and active galactic nuclei

Osterbrock, D. E., & Pogge, R. W. 1985, ApJ, 297, 166, doi: 10.1086/163513

Park, D., Woo, J.-H., Bennert, V. N., et al. 2015, ApJ, 799, 164, doi: 10.1088/0004-637X/799/2/164

Park, D., Woo, J.-H., Treu, T., et al. 2012, ApJ, 747, 30, doi: 10.1088/0004-637X/747/1/30

Peng, C. Y., Ho, L. C., Impey, C. D., & Rix, H.-W. 2011, GALFIT: Detailed Structural Decomposition of Galaxy Images, Astrophysics Source Code Library. http://ascl.net/1104.010

Peng, C. Y., Impey, C. D., Rix, H.-W., et al. 2006, ApJ, 649, 616, doi: 10.1086/506266

Perrotta, S., Hamann, F., Zakamska, N. L., et al. 2019, MNRAS, 488, 4126, doi: 10.1093/mnras/stz1993

Peterson, B. M. 2004, in The Interplay Among Black Holes, Stars and ISM in Galactic Nuclei, Vol. 222, 15–20

Pizagno, J., Prada, F., Weinberg, D. H., et al. 2007, AJ, 134, 945, doi: 10.1086/519522

Polletta, M., Tajer, M., Maraschi, L., et al. 2007, ApJ, 663, 81, doi: 10.1086/518113

Rakshit, S., Stalin, C. S., Chand, H., & Zhang, X.-G. 2017, ApJS, 229, 39, doi: 10.3847/1538-4365/aa6971

Rakshit, S., & Woo, J.-H. 2018, ApJ, 865, 5, doi: 10.3847/1538-4357/aad9f8

Rockosi, C., Stover, R., Kibrick, R., et al. 2010, in Ground-based and Airborne Instrumentation for Astronomy III, Vol. 7735, 77350R

Runco, J. N., Cosens, M., Bennert, V. N., et al. 2016, ApJ, 821, 33, doi: 10.3847/0004-637X/821/1/33

Salpeter, E. E. 1964, ApJ, 140, 796, doi: 10.1086/147973

Sarzi, M., Falcón-Barroso, J., Davies, R. L., et al. 2006, Monthly Notices of the Royal Astronomical Society, 366, 1151, doi: 10.1111/j.1365-2966.2005.09839.x

Schmidt, M. 1963, Nature, 197, 1040, doi: 10.1038/1971040a0

Schramm, M., & Silverman, J. D. 2013, ApJ, 767, 13, doi: 10.1088/0004-637X/767/1/13

Sérsic, J. L. 1963, Boletin de la Asociacion Argentina de Astronomia La Plata Argentina, 6, 41

Sexton, R. O., Canalizo, G., Hiner, K. D., et al. 2019, The Astrophysical Journal, 878, 101, doi: 10.3847/1538-4357/ab21d5

Shen, Y., Greene, J. E., Strauss, M. A., Richards, G. T., & Schneider, D. P. 2008, ApJ, 680, 169, doi: 10.1086/587475

Shen, Y., & Kelly, B. C. 2010, ApJ, 713, 41, doi: 10.1088/0004-637X/713/1/41

Shen, Y., Greene, J. E., Ho, L. C., et al. 2015, ApJ, 805, 96, doi: 10.1088/0004-637X/805/2/96

Shields, G. A., Gebhardt, K., Salviander, S., et al. 2003, ApJ, 583, 124, doi: 10.1086/345348

Shuder, J. M., & Osterbrock, D. E. 1981, ApJ, 250, 55, doi: 10.1086/159347

Silva, L., Granato, G. L., Bressan, A., & Danese, L. 1998, ApJ, 509, 103, doi: 10.1086/306476

Simard, L., Trevor Mendel, J., Patton, D. R., Ellison, S. L., & McConnachie, A. W. 2011, VizieR Online Data Catalog, J/ApJS/196/11

Stickley, N. R., & Canalizo, G. 2014, ApJ, 786, 12, doi: 10.1088/0004-637X/786/1/12

STScI development Team. 2013, pysynphot: Synthetic photometry software package, Astrophysics Source Code Library. http://ascl.net/1303.023

Tremaine, S., Gebhardt, K., Bender, R., et al. 2002, ApJ, 574, 740, doi: 10.1086/341002

Treu, T., Woo, J.-H., Malkan, M. A., & Blandford, R. D. 2007, ApJ, 667, 117, doi: 10.1086/520633

Valdes, F. 1984, in Bulletin of the American Astronomical Society, Vol. 16, 497

Valdes, F., Gupta, R., Rose, J. A., Singh, H. P., & Bell, D. J. 2004, The Astrophysical Journal Supplement Series, 152, 251, doi: 10.1086/386343

Valencia-S., M., Zuther, J., Eckart, A., et al. 2012, in Proceedings of Nuclei of Seyfert galaxies and QSOs - Central engine & conditions of star formation (Seyfert 2012). 6-8 November, 17

van Dokkum, P. G., Bloom, J., & Tewes, M. 2012, L.A.Cosmic: Laplacian Cosmic Ray Identification, Astrophysics Source Code Library. http://ascl.net/1207.005

van Dokkum, P. G., & Franx, M. 2001, ApJ, 553, 90, doi: 10.1086/320645

Vazdekis, A., Sánchez-Blázquez, P., Falcón-Barroso, J., et al. 2010, MNRAS, 404, 1639, doi: 10.1111/j.1365-2966.2010.16407.x

Veilleux, S. 1991, ApJS, 75, 383, doi: 10.1086/191535

Véron-Cetty, M. P., Joly, M., & Véron, P. 2004, A&A, 417, 515, doi: 10.1051/0004-6361:20035714

Véron-Cetty, M. P., Véron, P., & Gonçalves, A. C. 2001, A&A, 372, 730, doi: 10.1051/0004-6361:20010489

Virtanen, P., Gommers, R., Oliphant, T. E., et al. 2020, Nature Methods, 17, 261, doi: https://doi.org/10.1038/s41592-019-0686-2

Volonteri, M. 2010, Astronomy and Astrophysics Review, 18, 279, doi: 10.1007/s00159-010-0029-x

Wandel, A., Peterson, B. M., & Malkan, M. A. 1999, ApJ, 526, 579, doi: 10.1086/308017

Wang, J., Xu, D. W., & Wei, J. Y. 2018, ApJ, 852, 26, doi: 10.3847/1538-4357/aa9d1b

Wang, T., & Lu, Y. 2001, A&A, 377, 52, doi: 10.1051/0004-6361:20011071

White, R. L., Becker, R. H., Helfand, D. J., & Gregg, M. D. 1997, ApJ, 475, 479, doi: 10.1086/303564

Whittle, M. 1985, MNRAS, 213, 1, doi: 10.1093/mnras/213.1.1

Whittle, M., Pedlar, A., Meurs, E. J. A., et al. 1988, ApJ, 326, 125, doi: 10.1086/166074

Wilson, A. S., & Willis, A. G. 1980, ApJ, 240, 429, doi: 10.1086/158248

Woo, J.-H., Bae, H.-J., Son, D., & Karouzos, M. 2016, ApJ, 817, 108, doi: 10.3847/0004-637X/817/2/108

Woo, J.-H., Schulze, A., Park, D., et al. 2013, ApJ, 772, 49, doi: 10.1088/0004-637X/772/1/49

Woo, J.-H., Treu, T., Malkan, M. A., & Blandford, R. D. 2006, ApJ, 645, 900, doi: 10.1086/504586

—. 2008, ApJ, 681, 925, doi: 10.1086/588804

Woo, J.-H., Treu, T., Malkan, M. A., Ferry, M. A., & Misch, T. 2007, ApJ, 661, 60, doi: 10.1086/516564

Woo, J.-H., Yoon, Y., Park, S., Park, D., & Kim, S. C. 2015, ApJ, 801, 38, doi: 10.1088/0004-637X/801/1/38

Woo, J.-H., Treu, T., Barth, A. J., et al. 2010, ApJ, 716, 269, doi: 10.1088/0004-637X/716/1/269

Wylezalek, D., Flores, A. M., Zakamska, N. L., Greene, J. E., & Riffel, R. A. 2020, MNRAS, 492, 4680, doi: 10.1093/mnras/staa062

Xiao, T., Barth, A. J., Greene, J. E., et al. 2011, ApJ, 739, 28, doi: 10.1088/0004-637X/739/1/28

Xu, D., Komossa, S., Zhou, H., et al. 2012, AJ, 143, 83, doi: 10.1088/0004-6256/143/4/83

York, D. G., Adelman, J., Anderson, John E., J., et al. 2000, AJ, 120, 1579, doi: 10.1086/301513

Zahid, H. J., Geller, M. J., Fabricant, D. G., & Hwang, H. S. 2016, ApJ, 832, 203, doi: 10.3847/0004-637X/832/2/203

Zakamska, N. L., & Greene, J. E. 2014, MNRAS, 442, 784, doi: 10.1093/mnras/stu842

Zakamska, N. L., Hamann, F., Pâris, I., et al. 2016, MNRAS, 459, 3144, doi: 10.1093/mnras/stw718

Zhang, S., Wang, T.-G., Wang, H., et al. 2010, ApJ, 714, 367, doi: 10.1088/0004-637X/714/1/367

Zhang, X.-G., & Feng, L.-L. 2017, MNRAS, 468, 620, doi: 10.1093/mnras/stx519